UNIVERSITY OF OKLAHOMA

GRADUATE COLLEGE

ADVANCED SIGNAL PROCESSING

FOR MULTI-MISSION AIRBORNE RADAR

A DISSERTATION

SUBMITTED TO THE GRADUATE FACULTY

in partial fulfillment of the requirements for the

Degree of

DOCTOR OF PHILOSOPHY

By

Ramesh Nepal
Norman, Oklahoma
2018

ADVANCED SIGNAL PROCESSING
FOR MULTI-MISSION AIRBORNE RADAR

A DISSERTATION APPROVED FOR THE
SCHOOL OF ELECTRICAL AND COMPUTER ENGINEERING

BY

Dr. Yan "Rockee" Zhang, Chair

Dr. S. Varahan

Dr. J.R. Cruz

Dr. Choon Yik Tang

Dr. Lei Ding

Dr. Mark E. Weber

To my mum, Radha, buwa, Ratna, and my wife, Shivani

Acknowledgments

I would like to express my deep gratitude to my advisor and committee chair Dr Yan "Rockee" Zhang. His support, encouragement, and guidance has been enormous throughout my graduate studies. The collaborations he arranged have been monumental in advancing my research. My gratitude to my committee members for their guidance and flexibility throughout this process. My thanks to Dr Zhengzheng Li for his collaboration and advice.

Furthermore, I'd like to acknowledge Garmin Inc, Kansas, for their collaboration and support. I'm thankful to the whole radar team at Garmin, especially Dr William Blake for his invaluable insights, suggestions, and feedbacks. The hardware support as well as the data provided by them have been instrumental in my research.

I also extend my appreciation to the faculty and staff at School of Electrical and Computer Engineering as well as Advanced Radar Research Center (ARRC) at University of Oklahoma. Additionally, many thanks to my friends and colleagues, especially, Jingxiao Cai, Xinning Yu, Ridhwan Mirza, Zhe Li, and Yunish Shrestha for helping me during various stages and for being good friends. All of you have made my stay at Norman delightful and memorable.

Finally, I'd like to acknowledge the support and sacrifices from my family. Their love has propelled me forward and motivates me every day.

Table of Contents

List of Tables

List of Figures

Abstract

With the technological advancement of the 21st century, functions of different radars are being merged. A multi-functional system brings the technology of remote sensing to a wide array of applications while at the same time reduces costs of implementation and operation. Ground-based multi-mission radars have been studied in the past. The airborne counterpart deserves a through study with additional and stringent requirements of cost, size, weight, and power.

In this dissertation, multi-mission functions in an airborne radar is performed using modular, software-based architecture. The software-based solution is chosen instead of proposing new hardware, primarily because evaluation, validation, and certification of new hardware is onerous and time consuming. The system implementations are validated using simulations as well as field measurements. The simulations are carried out using Mathworks$^{\circledR}$ Phased Array System Toolbox. The field measurements are performed using an enhanced commercial airborne radar system called **P**olarimetric **A**irborne **Rad**ar **O**perating at **X**-band Version 1 (PARADOX1), which is an X-band, vertically polarized, solid state, pulsed radar.

The shortcomings of PARADOX1 originate from small aperture size and low power. Various signal processing algorithms are developed and applied to PARADOX1 data to enhance the data quality. Super-resolution algorithms

in range, angle, and Doppler domains, for example, have proven to effectively enhance the spatial resolution. An end-to-end study of single-polarized weather measurements is performed using PARADOX1 measurements. The results are compared with well established ground-based radars. The similarities, differences as well as limitations (of such comparisons) are discussed. Sense and Avoid (SAA) tracking is considered as a core functionality and presented in the context of safe integration of Unmanned Aerial Vehicles (UAV) in national airspace. A "nearly" constant acceleration motion model is used in conjunction with Kalman Filter and Joint Probabilistic Data Association (JPDA) to perform tracking operations. The basic SAA tracking function is validated through simulations as well as field measurements.

The field-validations show that a modular, software-based enhancement to an existing radar system is a viable solution in realizing multi-mission functionalities in an airborne radar. The SAA tracking is validated in ground-based tests using an x86 based PC with a generic Linux operating system. The weather measurements from PARADOX1 and the subsequent data quality enhancements show that PARADOX1 data products are comparable to those of existing ground based radars.

Chapter 1

Introduction

1.1 Introduction

RADAR is an acronym for Radio Detection and Ranging. A general radar transmits an electromagnetic pulse and then measures the backscattered signal. Such a radar is called a monostatic[1] pulsed[2] radar. The hardware of a radar can be recognized as a combination of transmitter subsystem, antenna subsystem, and receiver subsystem. The transmitter subsystem is responsible for modulating the carrier frequency with a radar waveform (e.g. Linear/Non-linear frequency modulated, various phase coded waveforms, etc.). The transmitter subsystem is also responsible for band-pass filtering as well as amplifying the signal before delivering it to the antenna. Since a single antenna is used for transmit and receive, either a circulator or a switch is positioned between the antenna and transmitter/receiver subsystems. Both (circulator and switch) are three port microwave devices that are responsible for routing the signal to the proper port. This ensures the signal from transmitter can only go to the antenna and signal back from antenna can only go to the receiver. During the signal routing, the receiver subsystem is isolated from the transmitter

---

[1] co-located transmitter and receiver

[2] transmitting a pulse instead of a continuous signal
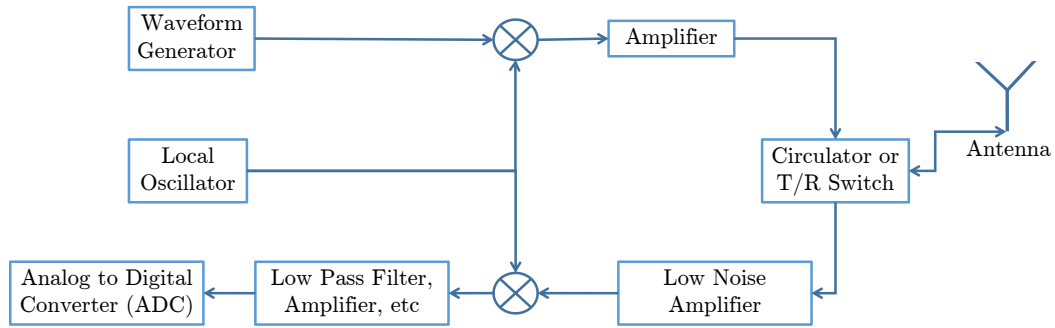
Figure 1.1: A basic monostatic radar block diagram

subsystem thereby preventing any interference or overloading of various receive components. A limiter is often the first component in the receiver subsystem to further prevent any inadvertent leakage of the transmitted signal. The antenna subsystem functions to radiate the signal out to the atmosphere and collect the backscattered signal. It can be as simple as a mechanical disk or as elaborate as a phased array antenna with each elements' own transmitter and receiver subsystems. The receiver subsystem, on the other hand, amplifies the signal, down-converts the signal to baseband (through one or more intermediate frequency steps), and delivers the signal to an analog-to-digital converter (ADC). Finally, the ADC digitizes the signal which can then be processed in real time or stored for further processing. Figure 1.1 shows a very simple radar block diagram. In modern times, the digitized signal is used for detection, display, and various signal processing algorithms. In spite of differences in hardware, this study treats radar hardware as a general sensor and concerns itself with the various signal processing algorithms after digitization via the ADC.

Although there are different types of radar, this dissertation focuses on a monostatic pulsed radar with a coherent receiver. A coherent receiver is the one that can retrieve phase information of the returned signal in addition to

its amplitude. The amplitude of the returned signal is associated to the Radar Cross Section (RCS) of the remote target while the phase of the returned signal depends on the target's range, relative velocity, and the signal propagation medium. Since most modern radars can transmit/receive multiple pulses, using a coherent receiver, a progressive change in phase can be calculated. This change in phase can then be used to estimate the radial velocity of the remote target. The number of pulses transmitted every second is called the Pulse Repetition Frequency (PRF). The interval in which a set of coherent pulses are transmitted and received is called the Coherent Processing Interval (CPI). Each CPI can, therefore, consist of a wide variety of waveform and PRF combinations. The amplitude of the target, again, analogous to the RCS, depends more on the electrical properties of the target and the aspect angle to/from the radar rather than just its physical size. For example, the RCS of a metallic vehicle is greater than that of a tree with similar size. Furthermore, the RCS of a metallic plate is much less when its normal is not along the direction of radar. The range to the remote target is calculated by measuring the delay between the transmitted and the received pulse. The continuous returned signal is sampled in time or "binned" to get a range profile data. Note that the continuous signal here is in contrast to the discrete signal. In a scanning radar, the antenna is pointed towards different azimuth and elevation angles to get a 2D or a 3D representation of the environment. The range, angle, amplitude, and phase data can then be processed in real time to estimate radar products or stored for post-processing algorithms.

In modern times, radar is used ubiquitously in defense, weather, scientific, law enforcement communities as well as in commercial sectors. The first patent associated with radar comes from Christian Hülsemeyer in Düsseldorf,

Germany for detecting metallic objects using electrical waves and subsequent demonstration at the Hohenzollern Bridge in Cologne, Germany in 18th May 1904 [1]. US Naval Research Laboratory (NRL) demonstrated detection of a ship by a radar in 1922 and then accidentally detected aircraft(s) in 1930 which set off more substantial investigations in the field of remote sensing using radar [2]. Further development of radar (including pulsed doppler radar) continued during and after World War II primarily driven by military and defense needs such as surveillance, navigation, and weapon guidance for ground, sea, and air vehicles [2], [3].

On the meteorology side, the exact origin of a weather radar still remains a mystery mainly due to wartime secrecy [3]. The interest in radar meteorology stems from the apparent weather related interference during the detection of aircrafts. The first detection of precipitation might have happened in the later half of 1940 in General Electric Corporation Research Laboratory in Wembley, England primarily due to the works by Dr. J. W. Ryde [3]. In the US, armed services, particularly Air Force and its Cambridge Research Laboratories were actively involved in studies related to meteorological capabilities of a radar. The National Severe Storms Laboratory (NSSL) was formed in 1964 which furthered meteorological research using Weather Surveillance Radar-1957 (WSR-57) [4], [5]. Currently in the US, National Weather Service (NWS) operates a network of 159 high resolution S-band Doppler weather radars called WSR-88D (Weather Surveillance Radar 1988 Doppler). Collectively, these radars are referred to as Next Generation Radar or NEXRAD [6]–[8]. The data from all the NEXRAD radars are publicly available at [9].

In recent years, automotive radars are increasingly being used and researched as a means of sensing road hazards and provide more autonomous capability

to road vehicles. A radar sensor is capable of detecting vehicles, pedestrians, as well as road barriers in all weather conditions, both in daytime as well as nighttime. The availability of low cost processing systems as well as high precision component manufacturing procedures have paved the way for a variety of such automotive radars. Those radars generally transmit Frequency Modulated Continuous Wave (FMCW) waveforms and use Multiple Input, Multiple Output (MIMO) antenna technique for transmit and receive. One substantial difference between a pulsed system and a CW (continuous wave) system is that the former can operate with a single antenna and a single up/down conversion chain while the latter requires at least two antennas and, in general, matching number of up/down conversion chains. The frequency modulation of the waveform enables the range measurement while transmitting and simultaneously receiving the continuous wave. Multiple chirps[3] can be transmitted to measure phase information and subsequently estimate the radial velocity. The MIMO operation allows the use of a variety of angle finding algorithms to locate the angular position of remote scatterers.

Modern radar applications can be primarily grouped into detection, imaging and tracking. In addition to defense and meteorology related applications discussed above, radars are widely used in

1. Air traffic control/management

2. Altitude measurement during flights

3. Weather hazards measurement/monitoring/avoidance in aviation

4. Detection and collision avoidance by ships and now by automobiles

---

[3]a signal with varying frequency

5. Velocity measurement (either by law enforcement or in sports like tennis, baseball, etc.)

6. Micro-Doppler (small Doppler due to rotating objects) measurements and studies

7. Imaging the earth's topography, and environmental characteristics (e.g. forests, ice, water, land use etc)

8. Radar ecology (e.g. measuring migratory birds' behaviors)

Currently, a different radar would be designed and implemented for each of the different applications numerated above. The variations in applications require a reciprocal variations in frequency bands, components, antennas as well as data collection methods, and signal processing algorithms. For example, in radar meteorology, reflectivity is often calculated using Rayleigh approximation which is strictly valid only for frequencies less than 3 GHz [3]. In military and aviation applications, the antenna pattern and scan rate needs to be different than in meteorological applications. In SAR (Synthetic Aperture Radar) and MTI (Moving Target Indication) applications, the data collection method as well as signal processing algorithms are extremely different. Due to all of these considerations, distinct radar systems for distinct applications have been historically warranted.

In recent years, there have been some development of multi-mission radars [10]–[12]. These radars serve the military, and defense communities and are generally expensive. They employ Active Electronically Scanned Array (AESA) antenna architecture which adds to the cost and complexity. The critical issue of Cost, Size, Weight, and Power (C-SWaP) seem to be largely ignored in those radars. Furthermore, there does not seem to be a civilian or a commercial

counterpart to such multi-mission radars.

However, technological advancements in hardware, computer systems, and digital signal processing algorithms allow us to carry out multiple operations using the same radar system. This leads to a lower number of required radar systems which in turn results in reduced cost of operation as well as maintenance [13]. Therefore, a multi-function radar that can meet all the required operational necessities is a cost effective solution. Furthermore, a multi-mission radar is the next chapter in radar technological advancement as the component level advancement approaches the required maturity. In addition to performance improvements, the ongoing advancements in various radar components have resulted in increased component bandwidth thereby enabling frequency diverse applications while using same hardware. The proliferation of phased array antennas has paved a way for not only very rapid electronic scanning but also changing the antenna pattern on the fly. The MIMO technique together with angle finding algorithms enable using smaller number of antenna array elements while maintaining the required beamwidth and performance. The continued advancements in computer architecture, processing speed as well as data I/O and storage have resulted in implementations of digital radar systems that can support a variety of data collection methods as well as various real time and post processing algorithms.

1.2   Ground based Multi-Mission Radar

Ground based multi function/mission radars have been an area of active research. An overall implementation is therefore not too far in the horizon. Such radar system will be able to replace NEXRAD [5]–[8], Terminal Doppler Weather Radar (TDWR) [14], and Airport Surveillance Radar (ASR-9 and

ASR-11) [15]. These radars will be of interest to various government agencies and civilian sectors alike. The fast electronic scanning capability provided by a phased array antenna has provided a means to multi-function while maintaining adequate update intervals. The National Weather Radar Testbed (NWRT [16], [17]) located in Norman, OK has been a focus for such studies [18], [19]. The Multi-Function Phased Array Radar (MPAR) is a project that is being undertaken by National Severe Storms Laboratory (NSSL) with its various industry and academic partners to achieve the goal of multi-function ground based radar. The requirements and road-maps of MPAR have been previously studied [19]–[21].

Another ground based radar that has the potential to become a multi-function radar is the Cylindrical Phased Array Radar (CPAR) [22], [23]. There have been studies about antenna design and calibration for such multi-mission radars [24]–[27]. While CPAR studies is currently more focused on weather measurements, validation, and subsequent studies, the phased array architecture provides a promising prospect for multi functionality. Therefore, in the ground based case, there are plans and ongoing studies on multi-functionality. However, an overall system characterization, implementation, and demonstration has not been done yet.

1.3   Airborne Multi-Mission Radar

As "single-mission" airborne radars complement "single-mission" ground based radars for various civilian, military, and scientific necessities, such is the case for a multi-mission radar. The challenges in development and implementation of an airborne counterpart of a multi-mission radar, on the other hand, are more extreme. The classical bottle-neck of C-SWaP advances non-linearly

as more functionalities are added to an airborne radar. The data storage and processing present challenges in terms of bandwidth, throughput as well as radar products' estimation and retrieval. This paradox is also present in ground-based multi-mission radars, although with the benefit of higher margin in size, weight, and power requirements. A majority of ground based radars are migrating towards Phased Array Antenna architecture due to the high speed electronic scanning capability. However, the Phased Array architecture has a little to do with low cost. In the most advanced Phased Array system, each element requires its own up/down conversion chain as well as data I/O ports and storage solutions. The appetite for larger and simultaneous processing power is perennial, especially, in radars which are, in affect, digitizing and manipulating high frequency signals and interpreting the results. The signal processing challenge comes in two-fold, one in terms of hardware as the incoming analog signals need to be digitized error free and efficiently; and another in software as those digitized signals need to be processed in real time or stored for later processing. So far as parallelizing the data acquisition/processing is concerned, not all the desired parallelizations can be achieved as the data collection and processing sometimes must follow sequential algorithms. There have been studies about using General Purpose Graphical Processing Unit (GPGPU) to perform parallel computations [28]–[30].

Currently, airborne weather radars are being used extensively in aviation and defense applications. There continues to be a pertinent appetite for research quality data originating from airborne platforms. There have been previous efforts to build and operate a research grade airborne weather radar. While no longer in commission, the ELDORA/ASTRAIA (Electra Doppler Radar/Analyese Stereoscopic par Impulsions Aeroporte) airborne Doppler

weather radar [31], [32], operated by NCAR/UCAR (National Center for Atmospheric Research, University Corporation for Atmospheric Research), is an example of an airborne radar for scientific missions. Another example is the Airborne Rain Mapping Radar (ARMAR) developed by NASA and Jet Propulsion Laboratory for operation on NASA DC-8 aircraft [33], [34]. A variety of studies and measurements were performed with ELDORA in focus [35], [36] as well as with ARMAR in focus [37]–[39]. The utility of such scientific mission radars cannot be overstated, however, these radars present a substantial financial burden for operation and maintenance. While, such radars are essential in remote sensing studies, the cost of operation results in very sparse coverage both in time and space. A multi-mission radar can be a viable replacement for single mission airborne radars for scientific studies.

The bulk of current generation of airborne radars are being used to detect and assess weather hazards and thereby provide situational awareness to pilots. One of the requirements of a multi-mission capable airborne radar is to provide commercial grade output (for pilots) while at the same time be able to store/process research grade data when necessary. Traditionally, multi-mission applications in airborne radar is implemented through expensive phased array architectures. The military and defense communities are, again, the pioneers in this sector as they are well equipped to absorb the ensuing expenditures. So far as civilian and commercial sectors are concerned, achieving multi-function capabilities have been difficult, especially, on a low-cost airborne radar system. These low-cost systems usually do not have the quality of electronics, antenna with desired beamwidth, and computing power to support advanced capabilities. However, as technology matures and the costs subside, the implementation of such low C-SWaP systems appear to be more feasible.

For meteorology, the challenge/mission is usually the precise measurement of scattering power and phase response from moving platforms. These measurements are sometimes referred to as "raw" or I/Q returns. One of the goals in meteorology is to properly estimate "radar products" which can then be used not only to estimate current weather parameters (like rainfall rate) but also to make future weather predictions (weather forecast). For a single polarized system, radar products to be estimated are Reflectivity, Doppler Velocity, and Spectrum Width; whereas for dual polarized systems, additional radar products like Differential Reflectivity, Correlation Coefficient, and Specific Differential Phase need to be estimated [3], [40], [41]. The "raw" measurements along with the radar products drive bulk of the weather related research which is necessary for our understanding of climate and weather phenomena as well as for preparedness against potential weather hazards.

1.3.1   Sense and Avoid

One of the core missions of a multi-mission radar is the sense and avoid capability. Modern airspace is shared by a variety of civilian, commercial, and military aviation in addition to birds and meteorological elements like rain/storm clouds. All of those objects simultaneously present in an airspace are potential threats to aviation. Uncooperative and unresponsive aircrafts are also a concern, especially in military aviation. With the current generation of airborne radars, there is more implementation of sensing part while avoiding part is performed manually. Unmanned airborne systems are already in the airspace in the form of military drones. It is just a matter of time when fully autonomous airborne systems traverse the skies during which the potential for safety becomes more imperative. The sense and avoid paradigm encompasses

sensing and tracking all the aforementioned airborne threats followed by a mitigation procedure. For an unmanned system, the first step is to ascertain the airspace properly and change course whenever necessary. This naturally includes radar as a sensor along with a tracking subsystem. A tracking subsystem can be viewed as a part of processing chain that conducts target associations, track initialization, prediction, update, maintenance and finally avoidance.

The concept of tracking emerged in the period of warfare when it was necessary to understand the adversary's flight path and motives. However, as humans have evolved, it is essential to view tracking not just as a defense apparatus but rather as a necessary tool that can aid in sharing of a common airspace. Since autonomous navigation is now a distinct possibility, the notion of tracking needs to evolve to encompass a broader meaning. Tracking of weather, for instance, should be included in this broader meaning. Bad weather is often the biggest threat to civilian and commercial aviation. Indeed, weather events cause in-flight injuries as well as hundreds of delays and cancellations of flights every year. As the airspace gets dense, the ability to track commercial/civilian flights and predict their next position becomes necessary. Although, virtually all of the air traffic today can be considered as cooperating targets, it is still desirable to track those aircrafts in the event of any malfunction in the transponder or the communication systems. There have been studies about the appropriateness of current system of air traffic control called the Traffic Alert and Collision Avoidance System (TCAS) [42]. While [42] focuses on Dynamic Programming, the predicament of potential failure or overload of TCAS still remains. An onboard, tracking capable, multi-mission airborne radar system is therefore, without a doubt, useful. Hence, tracking is considered as an essential subsystem for a multi-mission radar and such a radar needs to have the ability

to track a variety of targets, albeit with the mission of operational safety.

Then, there is the field of autonomous navigation of an unmanned aerial vehicle, which, although still in its infancy, has an ever growing list of applications that can benefit from a sense and avoid radar. On the defense sector, there has been feasibility studies that not only identifies the various requirements but also presents a potential road-map in realizing such an unmanned aerial vehicle with SAA capability [43], [44]. On the civilian sector, remote sensing and mapping takes precedence [45]. These group of applications, especially from the civilian surveillance prefer and in many cases have a hard requirement of low C-SWaP. Therefore, an airborne radar on unmanned aerial vehicles (UAVs) needs to address extreme constrains on C-SWaP. On the other hand, unmanned aircrafts still need similar (maybe more autonomous) capabilities for situation awareness compared to their manned counterparts [46]. Therefore, it is necessary to explore a variety of potential solutions that can alleviate the challenge of autonomous navigation while at the same time satisfying the requirement of low C-SWaP.

There are indeed other novel avenues for various signal processing algorithms in airborne multi-mission radars. Micro Doppler studies is one of them. Micro Doppler in radar returns are generated due to slight variation of Doppler velocity, especially, from a rotating target. When coupled with machine learning techniques, micro-Doppler signatures can be classified and/or recognized to discern different types of targets. One example is the recognition and classification of Wind Turbines in radar return data [47].

Apart from those outlined above, there can be more potential uses of airborne multi-mission radars. Airborne multi-mission radar is already poised to become a necessity when we examine all the diverse applications that it

can support. When the concept of radar was conceived about a century ago, a lot of its modern applications were unknown. Similarly, development and implementations of airborne multi-mission radar and the subsequent signal processing algorithms will undoubtedly introduce various novel applications than currently available/possible. The evolution of mankind and its technology has never failed to astonish and an airborne multi-mission radar will be no different. This study is one of the first steps in recognizing the possibility and hopes to pave a path to further studies, developments, and implementations.

1.4   Research Objective

In this study, the feasibility of a practical multi-mission airborne radar is examined in detail. With the challenges recognized above, there are two possible paths for the solution. One is to develop a higher frequency, lower-cost, and agile hardware, such as metamaterial scanner [48], similar to the hardware in automobile radars [49], etc. The drawback of implementing these new hardware changes is the necessity of thorough testing and validation as well as meeting the requirements of aircraft recertification. In addition, potential complications may arise during the development, implementation, and deployment of radar hardware as well as during configuration modifications.

The other path is to use existing and certified hardware such as low-cost weather radars. The functionalities can be enhanced through advanced signal processing algorithms. This study focuses on this second path where the signal processing algorithms are developed and applied. Because the enhancements are done in software, there is little or no need to modify existing hardware, thereby reducing the development time, costs as well as certification risks. Multiple independent modules of signal processors can be added to

enhance the capability of existing radar systems. There are still challenges to this approach. Low C-SWaP systems generally comprise of smaller aperture size, lower scanning speed, and in general slower computation time with less memory as well as components with lower throughput. These challenges will be addressed using modular hardware that can operate independently in parallel or in sequence depending on the mission requirements. One of the core objectives of this study is to verify that the signal processing algorithms can enhance the performance of a "single-mission" radar system to meet the Sense and Avoid (SAA) radar sensing requirements [50] or at least support the basic functionality of SAA operations as a part of multi-mission operations. Note that, although there has been FAA-RTCA (Federal Aviation Administration-Radio Technical Commission for Aeronautics) working groups actively investigating the SAA (also sometimes referred to as Detect and Avoid, DAA) radar sensing requirements [51], [52] the final performance requirements have not been finalized and released yet. Currently, SAA radars are being studied and developed by multiple industry entities. Some examples are the Due-Regard Radar from General Atomics [53], Northrop Grumman's SAA radar, and initial flight tests [54]. However, these on-going works do not appear to address the multi-functional application for low-cost radar operations, as well as the scenario of close-by multi-target tracking with angular resolution constraints. One innovative aspect of this work is the first time integration and application of advanced algorithms for SAA functions on a low-cost airborne weather radar platform.

In this study, a specific commercial weather radar platform is used and its functionalities are enhanced. The software based solution introduced in this study intends to use low-cost hardware and advanced algorithms/processing

back-end to meet the remote sensing goals for multi-mission applications. This work implements and validates a basic SAA function using an existing weather radar system, rather than proposing a completely new and dedicated SAA radar system. In addition to the demonstration of fulfilling basic operational needs using software processing and various signal processing algorithms, this study will also validate multi-mission capability of this enhanced radar system. The focus of this study is to determine the optimal operation mode and to perform algorithm development and data quality validations, both in cases of weather as well as sense and avoid (SAA) applications. The main challenges for the solution are the resolution limitation due to small aperture size, limitations from field-of-view (FOV), and scan speed due to mechanical scanning.

1.5   Outline of the Dissertation

Following Introduction, this study is organized as follows.

- Chapter 2 introduces a multi-mission airborne radar. It also builds some radar fundamentals in terms of weather and point target detection as well as radar signal spectrum. A formulation of tracking from a sense and avoid point of view is then presented.

- Chapter 3 introduces the signal processing algorithm suite as well as an end-to-end radar simulator.

- Chapter 4 details Iterative Adaptive Approach, and Matched Filter Based Iterative Adaptive Approach as real aperture super-resolution algorithms.

- Chapter 5 presents an example of tracking from sense and avoid perspective by using the aforementioned multi-mission radar and resolution enhancement algorithms.

- Chapter 6 analyzes weather surveillance using the same sensor platform and similar algorithms after which the results are validated against well known ground based research radar results.

- Chapter 7 presents a summary and conclusions arrived, in this study.

- Chapter 8 outlines future work.

Chapter 2

Airborne Multi-Mission Radar

Most of the radar systems built in the past were done to address a specific challenge; be it military radars, civil aviation radars, meteorological/weather or general research radars. Since each combination of a problem in an environment requires a slightly different system characteristics, such practice has been historically justified. Additionally, there were few overlaps between the interests of different communities (military, civilian, science/research) and therefore each radar was built to satisfy a particular necessity for a specific community. In recent times, the goals of different communities are increasingly overlapped. Tracking, for instance, was historically a defense apparatus but lately an increasing number of commercial applications are finding it beneficial. Weather studies, on the other hand, are of interest to not only researchers but also to aviation industry. Imaging radars are being used to study deforestation, ice sheet conditions, etc. in addition to mapping the earth's surface. Since the common goals of different radar communities are increasing, a multi-mission capable system can not only reduce cost, but also drive the industry forward as historically separate communities work towards a common set of goals.

Airborne radars have been a part of aviation community to access weather hazards. As discussed in Chapter 1, such radars are used solely for situational

awareness to the pilots. Since making hardware changes to an existing platform would be onerous as products need to be tested, validated, and re-certified, this study focuses on software modifications as a viable approach in realizing multi-mission airborne radar using a commercial airborne radar platform. One concept of such radar is PARADOX which is discussed below.

2.1 Polarimetric Airborne Radar Operating at X-band, PARADOX

Together with Garmin International Inc. the Intelligent Aerospace Radar Team (IART) at University of Oklahoma has been developing a new airborne weather radar system called **P**olarimetric **A**irborne **Rad**ar **O**perating at **X**-band (PARADOX). PARADOX has had multiple versions since 2007. In 2010 the first version (referred to as "version zero") was flight tested with an industry partner using IART designed hardware and some initial dual-polarimetric data for rainfall were collected. In 2012, PARADOX1 was developed, based on Garmin Inc's commercial GSX70 airborne weather transceivers and processors. Data collections were performed by designing and implementing various Coherent Processing Intervals (CPI's). The collected data were analyzed using a multitude of advanced signal processing methods [55]–[59]. PARADOX2 radar will, again, be based on a new generation of hardware from Garmin Inc. It will be upgraded to dual-polarization operation from the current configuration of vertically-polarized antenna.

Figure 2.1a shows the mechanical structure of PARADOX1 while Figure 2.1b shows the current setup. Table 2.1 lists the key parameters of PARADOX1. The low C-SWaP (Cost, Size, Weight and Power) of PARADOX1 makes it suitable for deployment on small to medium aircrafts including UAV's (Unmanned

Radar Parameters		Values
Mechanical Dimensions	Antenna Size	10-18 inches for standard antenna product configuration
	Transceiver Diameter	8 inches
	Depth	6.3 inches
	Total Weight	9.5 lbs (for a 18 inch antenna, and electronics) plus digital backend (small form factor PC)
Operating Frequency		9.3 to 9.5 GHz
Antenna		Slotted Waveguide Array and Mechanical Scanning
FOV		$\pm 60°$ azimuth, $\pm 30°$ elevation
Transmitter		Solid-state 40 watt peak power, support for a wide range of waveforms and PRFs
Sensitivity		0 dBZ @ 30 km
Receiver		Real-time pulse compression receiver with optimized LFM and phase coded waveforms
Antenna Beamwidth		Scalable: 18 inch panel: 5.6° az/el
Scan Speed		Variable (depends on the number of Transmitted Pulses)
Basic Data Products		Real-time: Reflectivity, Doppler velocity, spectrum width. Offline: SAR (Synthetic Aperture Radar) imaging, airborne hazard and biological target trajectory estimation
Mounting and Installation		Nose cone mounting or pod mounting

Table 2.1: PARADOX1 Specifications

(a) Mechanical Structure of GSX-70

(b) Current Configuration (with 12 inch antenna)
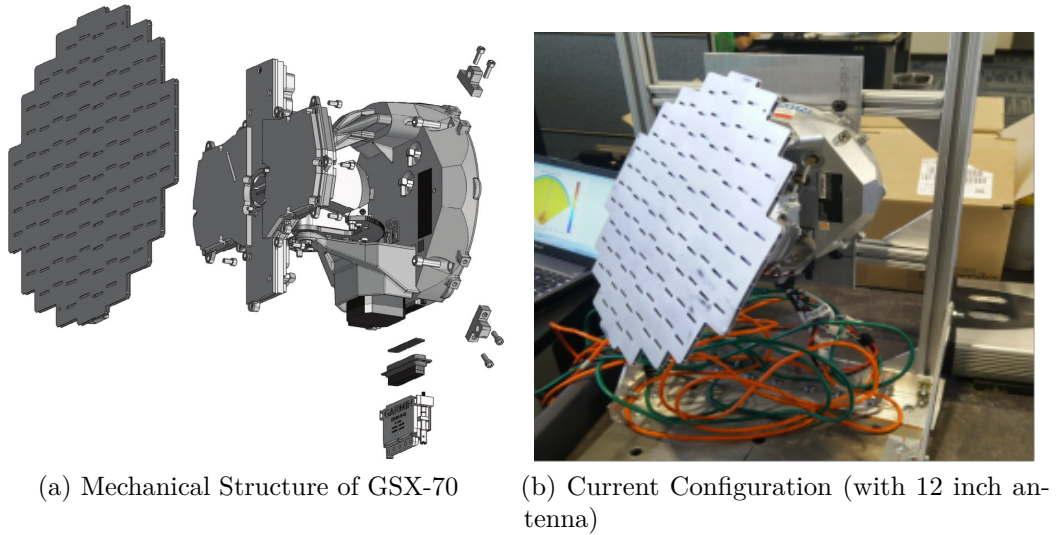
Figure 2.1: Garmin GSX70

Aerial Vehicles). The entire system, including the mechanical scanner and signal processors, is integrated into the 9.5 lbs, 8 inches diameter and 6.3 inches deep package. PARADOX1 is highly configurable by design and therefore a number of parameters listed on Table 2.1 have multiple available options. The aperture is a planar waveguide array that can have diameter from 6 to 18 inches for the current design, and can be extended to 50 inches with customized designs. In addition, PARADOX1, being a solid-state radar, also supports a variety of pulse compression waveforms. In the latest version of the hardware, a diverse number of phase coded waveforms, modulations, and bandwidths can be employed. The sensitivity of the radar can be tweaked using various duty cycles.

Figure 2.2 depicts the multi-mission concept of PARADOX1. The embedded mission processor can be configured to execute various missions simultaneously. The SAA (Sense And Avoid) tracking part, naturally, needs to be in Track While Scan (TWS) mode. Signal processing modules can be attached to data output of PARADOX1 to achieve improvements such as super-resolution

21
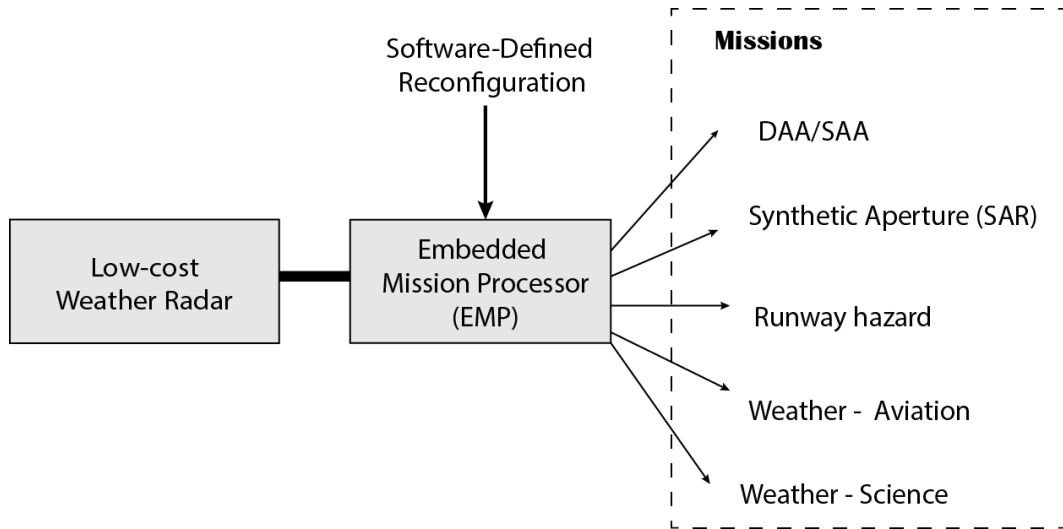
Figure 2.2: PARADOX1: A Multi-Mission Airborne Radar

(SR), range/azimuth/Doppler enhancement, sidelobe reduction etc. Chapter 4 describes the Range-Doppler-Azimuth Super-Resolution, which is an important step required to meet the multi functionality performance goals. Chapter 5 details the SAA tracking subsystem while Chapter 6 presents scientific research quality data validations. In each of the Chapters of this study, the data from PARADOX1 is used to not only verify the validity of the algorithms, but also to present PARADOX1 as an airborne multi-mission radar.

2.2 Radar Returns

A meaningful radar return data consists of a backscattered signal from a target that is stronger than the inherent thermal noise and/or any interference at the receiver. Radar returns are quantized in range, azimuth, and elevation. The ability to discern returns from remote targets in space or time (essentially resolving different targets) is referred to as resolution. An increase in resolution is accompanied by a decrease in the cell size of space or time in the measured

data. The resolution in range depends on the transmit waveform bandwidth[1]. Although there are high bandwidth radars that can achieve sub-meter resolution, for most radars range resolution varies from tens of meters to few hundred meters. Range resolution is generally constant for a set of data. The resolution in azimuth and elevation depends on the antenna pattern beamwidth[2]. Since radar/antenna beam broadens with increasing range, the azimuthal and elevation resolution decrease with an increase in range. The range, azimuth, and elevation resolution constitute a 3D "resolution volume" which is analogous to a 3D pixel. The shape of this pixel is reminiscent of a thin (3D) ellipsoid with the span in range direction being the smallest. In general, there are multiple scatters in each resolution volume. As a consequence, radar return is comprised of a superposition of the returns from those multiple scatterers.

In case of airborne radars, there are two distinct types of targets that need be considered. Firstly, the so-called hard targets that occupy very few range bins are modeled as single point targets. Some examples are other aircrafts, birds, most ground targets, and clutter if scanning downwards. The other type of target is the meteorological target, e.g. storm clouds, rain, hail, snow, etc. Those targets span multiple range, azimuth, and elevation bins and are modeled as distributed targets. Although the basic physics of both types of targets are largely similar, slightly different approaches are used for signal modeling and processing. The radar range equation that gives the fundamental signal model is discussed in the next section.

---

[1]All the components' bandwidth should be equal to or greater than that of the waveform, else the lowest bandwidth among the components determines the range resolution

[2]azimuth and elevation beamwidth may not necessarily be equal

2.3 Radar Range Equation

The radar range equation is a deterministic signal model that relates various radar system components to the environment and estimates the received power at the receiver. By providing the expected return value in a theoretical sense, radar range equation can provide an assessment of the capability of the radar system. The received power P_r from a target at range R, with radar cross section σ, using a radar of wavelength λ, with transmit power P_t, transmit antenna gain G_t, receive antenna gain G_r, assuming one way propagation loss l, and all other system losses (e.g. due to various system components like waveguides, power dividers, radome, etc.) lumped together as l_s is [2], [60]

$$P_r = \frac{P_t G_t}{4\pi R^2 l} \times \frac{\sigma}{4\pi R^2 l} \times \frac{G_r \lambda^2}{4\pi l_s} \tag{2.1}$$

Equation 2.3 is a simple form of radar range equation. The first fraction term on the right side is the directed power to the target; the second term is the backscattered power from the target; and the third term is power directed towards the receiver. Note that all the terms in equation 2.3 are of linear units and the received power is instantaneous. For a monostatic radar (radar with same antenna for transmit and receive), equation 2.3 can be simplified as

$$P_r = \frac{P_t G^2 \lambda^2 \sigma}{(4\pi)^3 R^4 l_s l_a} \tag{2.2}$$

Here, $G_t = G_r = G$ is the single antenna gain, and $l^2 = l_a$ is the two way propagation loss due to the atmosphere.

Equation 2.3 is the basic radar range equation for a point target. In the equation, σ is the unknown target RCS which is directly proportional to the return power. Radar range equation provides the expected echo power from

a remote target. In the next section, the returns from weather targets are examined followed by a discussion of the spectrum of such returns.

2.4   Weather Returns

One of the great utilities of modern radars is the ability to measure weather phenomena and access the associated threats to the infrastructure and public. Therefore, measuring weather is one of the core missions of a multi-mission radar. Especially for an unmanned airborne platform, proper weather measurements, and subsequent assessments are crucial for operational safety. In addition, weather measurements also provide critical research data for weather related studies. Weather studies are increasingly paramount as the humankind is beginning to appreciate the effect of changing climate. As aforementioned, weather returns comprise of superposition of returns from smaller scatterers in the 3D resolution volume and spans multiple such resolution volumes. It is, therefore, modeled as distributed target which results in radar range equation taking a slightly different form.

The RCS of a weather target is a contribution of RCS from different sizes and types of hydrometeors in the resolution volume. If we let η as the average RCS per unit volume and consider ΔV to be resolution volume then the ellipsoidal resolution volume can be expressed as,

$$\Delta V = \frac{c\tau\pi R^2 \theta_{az}\theta_{el}}{12} \tag{2.3}$$

where, θ_{az}, and θ_{el} are azimuth and elevation beamwidth respectively, c is the speed of light, τ is the pulsewidth and R is range to the target.

The average RCS per unit volume, η, is also called reflectivity and is

expressed as [3], [61]

$$\eta = \int_0^\infty \sigma_b(D)N(D)dD \tag{2.4}$$

where $\sigma(D)$ is the RCS for the scatter with diameter D and $N(D)$ is the number of such scatterers (with diameter D). Reflectivity, η is related to reflectivity factor Z as

$$\eta = \frac{\pi^5}{\lambda^4}|K_w|^2 Z \tag{2.5}$$

where K_w is the dielectric factor of water, $K_w = (\epsilon_w - 1)/(\epsilon_w + 2)$, and ϵ_w is the dielectric constant of water. The unit of Z is $mm^6 m^{-3}$ and is usually expressed as dBZ ($10log_{10}Z$). Equation 2.4 is called the Rayleigh approximation which is valid when diameters of hydrometeors are small compared to radar wavelengths [3], [61]. Therefore, radar range equation for weather targets takes the form

$$P_r = \frac{P_t G^2 \lambda^2}{(4\pi)^3 R^4 l_s l_a} \frac{\pi^5}{\lambda^4}|K_w|^2 Z \frac{c\tau\pi R^2 \theta_{az}\theta_{el}}{12} \tag{2.6}$$

Please note that although radar range equation for weather targets is derived using Rayleigh scattering approximation, often, this condition cannot be met, especially when the transmit frequency for a radar is high.

2.5   Spectrum of Radar Signals

As mentioned previously, modern radars are capable of concurrently measuring amplitude and phase of the returned echo from the remote target. The radar range equation in the previous section provided an expression for the amplitude of the echo (by formulating a power equation). The phase of the returned echo signal is used for frequency analysis in a range-azimuth-elevation volume or a resolution cell. Such frequency analyses provide the measure of velocity

contents (or a weighted distribution of velocities) in the volume. If there are targets in the resolution volume, the power spectrum plot for that cell consists of peaks equaling to the number of targets and each at the frequency/velocity location of the target. Note that if the velocity/Doppler resolution is not high enough, multiple peaks can get "merged" and can have the appearance of a single peak albeit wider. The width of those peaks also depends on the platform dynamics as well as the target characteristics. In case of weather measurements, the width of the peak (in the spectrum) is related to the atmospheric turbulence. The phase of the echo can be expressed as [3]

$$\psi_e = -\frac{4\pi r}{\lambda} + \psi_t + \psi_s \tag{2.7}$$

where, r is the range to the target, λ is the wavelength, ψ_t and ψ_s are the phase introduced by the transmitter and remote scatterer (target) respectively. The Doppler frequency is the time derivative of the phase which is,

$$f_d = \frac{1}{2\pi}\frac{d\psi_e}{dt} = \frac{1}{2\pi}\left(\frac{-4\pi}{\lambda}\right)v = -\frac{2v}{\lambda} \tag{2.8}$$

In equation 2.8 above, both ψ_t and ψ_s are considered to be time invariant. While ψ_t can be generally considered constant, more so for a ground based radar, ψ_s, on the other hand is more nuanced. For a non-meteorological target, ψ_s can be considered constant but for a meteorological target ψ_s is time varying due to vibration of water droplets during precipitation. Furthermore, since weather returns comprise of returns from multiple scatterers of different sizes in the resolution volume, the sum total of the phases from each target no longer remains time invariant. The vibration, of the meteorological targets, manifests itself as a broader peak in the Doppler spectrum. Please note that v

in equation 2.8 is the relative velocity and in fact is the relative radial velocity (i.e. the component of velocity in the line of sight direction).

In contrast to a ground based radar, an airborne radar is in motion during data collection and therefore a Doppler frequency shift is always present in the received signal. The spectrum is further complicated by the turbulence in the platform itself, causing random changes in ψ_t.

It is to be noted that a direct measurement of Doppler frequency from a single short pulse is not possible. The carrier frequency of a radar is fairly high; e.g. NEXRAD/WSR-88D radars' frequency is between 2.7 and 3 GHz, and for an airborne radar X-band (8 - 12 GHz) is the most popular choice. The change in phase caused in one short pulse (tens of micro-seconds) is generally within the limits of error. On the other hand, if there are multiple pulses transmitted and a coherent receiver is used, the difference of the phase between successive pulses can be calculated which can then provide the Doppler shift and finally the radial velocity of the remote target can be estimated.

As aforementioned, the velocity of a remote scatterer is estimated by doing a frequency domain analysis of the returned echo. Fourier Transform is taken on the time domain return signal to generate a power spectrum estimate. The Discrete Fourier Transform (DFT) of a time domain signal sampled M times at a uniform spacing T_s is defined as [3]

$$Z(kf_0) = \sum_{m=0}^{M-1} V(mT_s)e^{-j2\pi f_0 T_s mk} \qquad (2.9)$$

where $V(mT_s)$ is the complex voltage (amplitude and phase representation of the echo signal) of mth sample and $Z(kf_0)$ is the complex amplitude of the kth spectral coefficient at frequency $f = kf_0$. Similarly, the Inverse Discrete

Fourier Transform (IDFT) can be expressed as,

$$V(mT_s) = \frac{1}{M} \sum_{k=0}^{M-1} Z(kf_0)e^{j2\pi f_0 T_s mk} \tag{2.10}$$

Note that the sampling frequency here is the PRF and therefore sampling time, $T_s = 1/PRF$ and there are M total pulses in the CPI. Using the Nyquist criterion, the maximum unambiguous Doppler frequency that can be measured is $(2T_s)^{-1}$ or $PRF/2$. Examining equations 2.9, all the frequencies in the summation are multiples of $1/MT_s$ therefore, the Doppler resolution is $1/MT_s$ or PRF/M. Finally, the maximum unambiguous velocity that can be measured is derived using equation 2.8 as,

$$v_{ua} = \pm\frac{\lambda \cdot PRF}{4} \tag{2.11}$$

And the velocity resolution is,

$$\Delta v = \frac{\lambda \cdot PRF}{2 \cdot M} \tag{2.12}$$

The above equations, 2.11 and 2.12, give the extent of the estimated power spectrum as well as the location of the peak(s) if scatterers are present. Next the shape of the Doppler spectrum is briefly discussed.

The power spectrum of an infinite sinusoid is a delta function at the frequency of the sinusoid. If the sinusoid is multiplied by a rectangular envelope to generate a pulse in the time domain; in the frequency domain counterpart, it is equivalent to the convolution between the delta function (spectrum of sinusoid) and a sinc function (spectrum of rectangular envelope). The resulting spectrum is frequency shifted sinc function. A sequence of such pulses in a

CPI also result in a sinc function in the spectrum whose width is given by the frequency/velocity resolution. However, as discussed previously, if the phase change due to the scatterer ψ_s is varying with time, the resulting sinc function in the frequency spectrum broadens. In ground based weather radar, the width of the spectrum is related to the turbulence in the atmosphere. In case of airborne radar, the there is additional spectrum broadening due to the fluctuation of platform motion (manifested through the change in ψ_t).

2.6 Airborne Sense And Avoid

As mentioned previously, sense and avoid is a broader term that encompasses the notion of target tracking. Tracking capability will certainly be of great utility for pilots. In addition to that, it is also useful to the emerging field of autonomous navigation. As discussed previously, SAA tracking of weather as well as other aerial vehicles is a safety necessity.

Tracking, simply put, is an estimation of the current state/parameter of a moving object followed by a prediction of future state. This, of course, is complicated by the fact that moving objects never move in a perfect path and the measurements are always contaminated by the noise. Furthermore, the inherent limit in sensor resolution causes an uncertainty, in the measurement, and during the mathematical modeling of the tracking algorithm. Therefore a tracker has the function of filtering (noise), interpolating the measurements where necessary, estimating the true measurements, and predicting the future measurements. The prediction part is done by taking into account all the previous measurements as well as knowledge of parameters and the statistics of any involved noise and uncertainties. There are definitely a variety of approaches to estimation and prediction where the benefit of accuracy is

complemented by a complexity of computation.

In addition to the intricacies involved in estimation and prediction, modern tracking also involves with data association. In almost all of the practical scenarios, there are generally more than one detection. For an airborne case, it can be argued that there may be a single target in the current field of view in given time and space. However, the omnipresence of noise, clutter, and the resulting false alarms are sure to result in more than one detection. Data association part of sense and avoid associates detections to the previously established tracks or previously detected targets. There are, of course, different algorithms for data associations; one detection can be associated with one target/track (hard detection) or a more probabilistic soft detection approach can be undertaken where a single detection can be associated with more than one target/track.

For the application outlined in this study, Kalman Filter (KF) is used for estimating the state of dynamic targets and Joint Probabilistic Data Association (JPDA) is used for data association. Kalman Filter [62] provides a recursive method to optimally estimate the state of linear systems in presence of Gaussian error statistics. JPDA provides joint posterior association probabilities for multiple targets in presence of Poisson clutter [63], [64]. Together, JPDA and KF are responsible for initializing tracks, associating measurements as well as updating the tracks, states, and other relevant parameters. There are other state estimation algorithms available. Extended Kalman Filter (EKF) [65], [66] is based on the frameworks of Kalman Filter and includes estimation for non-linear systems. EKF is obtained by linearization of the (non-linear) process about the estimation point using Taylor Series expansion. First or second order EKF can be obtained using the appropriate order during linearization.
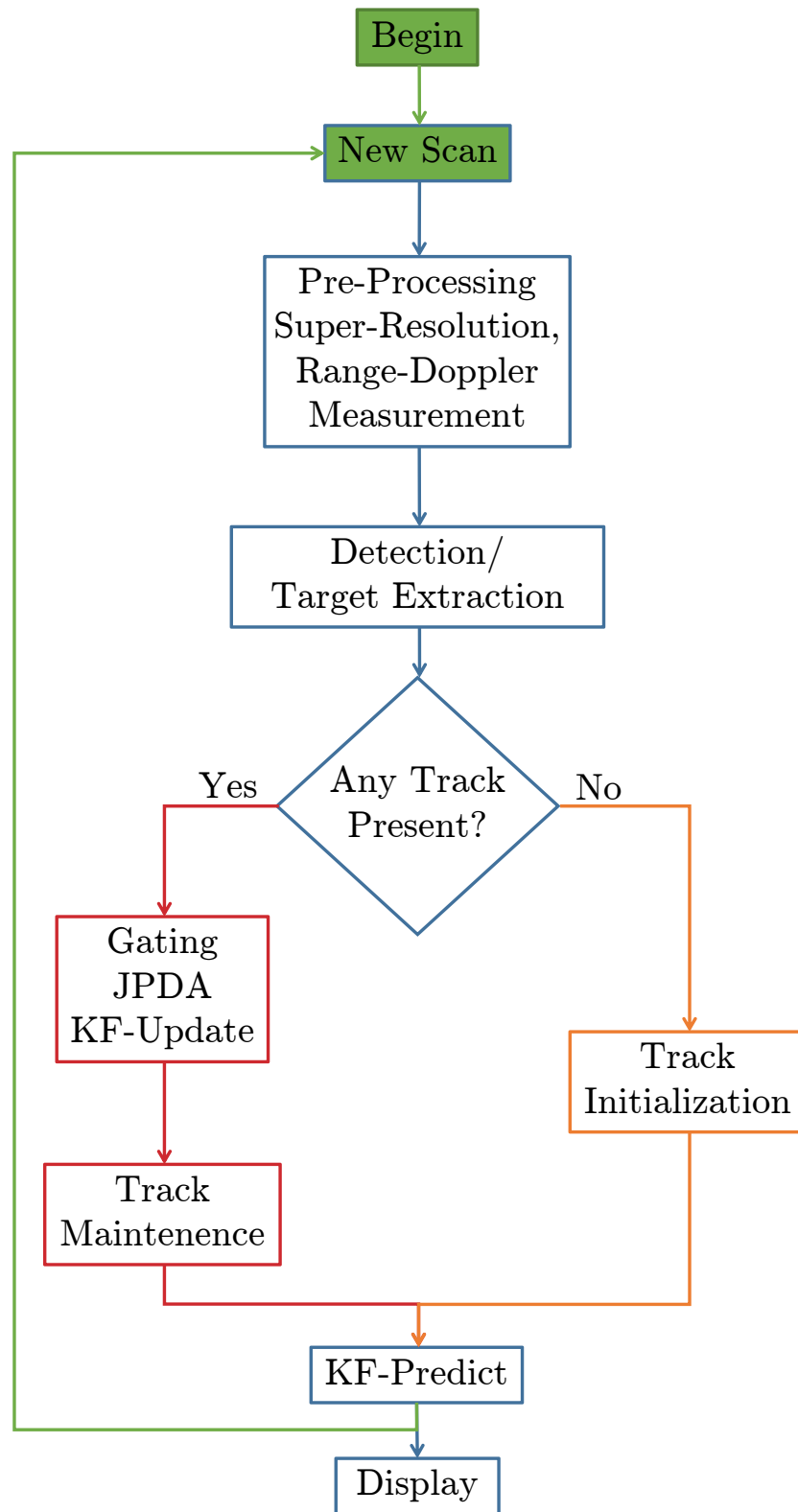
Figure 2.3: Tracking Flowchart

Particle Filter [67], [68], on the other hand, is also gaining popularity as faster computation/processing is increasingly available. Similarly, for data association multiple algorithms like Global Nearest Neighbor and Multiple Hypothesis Tracking [69]–[71] are available. At the end, KF and JPDA are used primarily because of good results with smaller/acceptable computational requirement.

Furthermore, a "g-sigma ellipsoid" gating is used to reject measurements for each track which further increases the computational speed. Figure 2.3 shows the SAA tracker algorithm flow. Note that "Track Maintenance" step adds and deletes track as necessary. A tentative track is added when a new target is not associated with any existing tracks. An existing track is deleted if no measurements are associated for a that track during multiple consecutive scans. A simulated two target scenario as well as measured single target scenario and tracking is presented later in this study. In this section, a theoretical basis of the tracking algorithm is discussed.

2.6.1   SAA Tracking with Constant Acceleration Model

There are different motion models that can be considered for tracking. While military and defense applications require more robust motion model to account for high "g" maneuvering targets (essentially to incorporate the effects of higher order derivatives of position into the motion model); the civilian applications, on the other hand, can have some of those requirements relaxed. Since this study presents tracking from sense and avoid perspective in an airborne multi-function radar, the goal of tracking is to ascertain any collision threat and change course if and when necessary. The targets can be safely assumed to move with a non-constant velocity while at the same time not performing the high "g" evasive maneuvering or have significant and/or deliberate jerks and jounces.

Therefore, a constant acceleration motion model can be used to formulate the dynamics of the system. This model, in reality, is a Wiener-process acceleration model [65], [72]. In other words, the acceleration in the model is a process with iid (independent identically distributed) increments. More precisely, the model is a white noise driven "nearly constant acceleration model" which allows for small changes in the acceleration (and those changes are assumed to be iid).

Consider, first, a one dimensional moving target. The recursive evolution of position s, velocity $\dot{s}$, and acceleration $\ddot{s}$ given the values at previous sampling time can be viewed as a noise driven process which can be represented as,

$$s_{k+1} = s_k + \dot{s}_k T + \frac{1}{2}\ddot{s}_k T^2 + \frac{1}{2}v_s T^2 \qquad (2.13)$$

$$\dot{s}_{k+1} = \dot{s}_k + \ddot{s}_k T + v_s T \qquad (2.14)$$

$$\ddot{s}_{k+1} = \ddot{s}_k + v_s \qquad (2.15)$$

where T is the update time and $k = nT$ (for integer n) is the sample time.

A moving target, in general, can move in all three dimensions. However, since the goal of an airborne sense and avoid radar is primarily avoidance, the three dimensional problem can be simplified to two dimensional one. Furthermore, for a general radar (like an airborne multi-mission radar), scanning and tracking in three dimension quickly becomes onerous as the update time can reach to tens of minutes. On the other hand, as technology matures a fast three dimensional scan is possible in which case tracking in two dimensions can be easily upgraded to three dimensions. The discrete time state-space model for a target moving in two dimensions can be extended from the one dimensional case above and is expressed as,

$$x_{k+1} = Fx_k + Gw_k \qquad (2.16)$$

where, x_k is the state vector at sample time k,

$$x_{k+1} = [s_x, s_y, \dot{s}_x, \dot{s}_y, \ddot{s}_x, \ddot{s}_y]^T_{k+1} \qquad (2.17)$$

F is the state transition matrix, represented as

$$F = \begin{bmatrix} 1 & 0 & T & 0 & \frac{1}{2}T^2 & 0 \\ 0 & 1 & 0 & T & 0 & \frac{1}{2}T^2 \\ 0 & 0 & 1 & 0 & T & 0 \\ 0 & 0 & 0 & 1 & 0 & T \\ 0 & 0 & T & 0 & 1 & 0 \\ 0 & 0 & 0 & 0 & 0 & 0 \end{bmatrix} \qquad (2.18)$$

G is the noise distribution matrix as,

$$G = \begin{bmatrix} \frac{1}{2}T^2 & 0 \\ 0 & \frac{1}{2}T^2 \\ T & 0 \\ 0 & T \\ 1 & 0 \\ 0 & 1 \end{bmatrix} \qquad (2.19)$$

and $w = [w_x, w_y]^T$ is the process noise vector (at sample time k) which is assumed to be a zero mean Gaussian noise with covariance Q. Similarly, the measurement equation can be expressed as

$$y_k = Hx_k + v_k \qquad (2.20)$$

where, y_k is the measured vector at sample time k, H is the measurement

35

transition matrix as,

$$H = \begin{bmatrix} 1 & 0 & 0 & 0 & 0 & 0 \\ 0 & 1 & 0 & 0 & 0 & 0 \end{bmatrix} \tag{2.21}$$

and v_k is the white Gaussian measurement noise (at k) with zero mean and a covariance of R.

Note that although radars measure in Polar/Spherical Coordinates, the measurement here is considered in Cartesian Coordinates. Spherical measurements to Cartesian measurements can be realized easily using trigonometric functions or a lookup table. The main drawback of using Polar/Spherical Coordinates is that the Coordinate transformation is a non-linear process which results in unnecessary complications due to H being non-linear [3].

The tracker is initialized at the first scan and when a measurement cannot be attributed to any tracks. The state covariance matrix is also initialized with a diagonal matrix at this stage. The process noise covariance matrix Q is kept at a low value. The measurement noise covariance matrix R is modeled as a function of range and azimuthal resolution. Since all detections are considered as potential targets, a tentative track is formed when any kind of unassociated (with track) detection is discovered. The M-of-N logic is used to elevate a tentative track to a confirmed track; i.e. a tentative track is confirmed when there are M valid detections out of last N scans. Whenever a track fails to adhere to the rule, the track is deleted. A valid detection is the one that situates inside a validation gate. The validation gate used is a g-sigma ellipsoid gate which can be defined as,

$$d(k) = \tilde{y}^T(k)S^{-1}\tilde{y}(k) \leq \gamma^2 \tag{2.22}$$

---

[3]Non-linear H requires to perform linear approximation by doing Taylor expansion at the measured value which adds complexity while decreasing accuracy

where, γ is the gate threshold which is obtained by choosing χ^2 distribution with two degrees of freedom at 0.99% confidence level. $\tilde{y}$ is the innovation (difference between predicted and measured value) and S is the innovation covariance obtained from Kalman Filter equations. The gate itself in this case is two dimensional ellipse obtained by cutting off the tails of a bivariate Gaussian density. The size of this validation region changes when the innovation covariance S changes during the evolution of the track.

2.6.2 Joint Probabilistic Data Association

When there is a single detection inside the validation region, it is straightforward to associate that measurement to the track. However, other targets, clutter or spurious detections might conceivably fall inside the validation gate. In such case, there needs to be an algorithm or a logic to associate the measurement with the track. Joint Probabilistic Data Association (JPDA) is a target-oriented data association algorithm that works well with interfering source in presence of Poisson clutter [63], [64]. An interfering source is one that persistently appears inside the validation region of a track/target. A full derivation of JPDA is beyond the scope of this study but can be found in [63], [73] etc. However, a brief formulation is presented as follows.

Assume there are N_t tracks and N_m measurements which are used in conjunction with gating (eq 2.22) to form a validation matrix. A feasibility matrix is then constructed which is a combination of all feasible events, θ, that are possible given the tracks, the measurements, and the validation matrix. Since missed detection is always possible, feasibility matrix has entry for events where the track is assumed to have missed the detection. The probability of each feasible event θ given measurement Y^k (at sample time k) can be

expressed using Bayes' rule,

$$P(\theta|Y^k) = P(\theta|\tilde{y}_1, \cdots, \tilde{y}_M, M, Y^{k-1})$$

$$= P(\tilde{y}_1, \cdots, \tilde{y}_M|\theta, Y^{k-1})P(\theta|M, Y^{k-1}) \qquad (2.23)$$

where, $\tilde{y}_j$ is the innovation of jth measurement ($j = 1, \cdots, M$). The above equation 2.23 can be simplified as [63]

$$P(\theta_{j,t}|Y^k) = \frac{C^\phi}{c} \prod_{\tau_j=1} \frac{exp[-\frac{1}{2}\tilde{y}_{j,t}^T S_t^{-1}\tilde{y}_{j,t}]}{(2\pi)^{M/2}|S_t|^{1/2}} \cdot \prod_{\delta_t=1} P_D \cdot \prod_{\delta_t=0} (1-P_D) \qquad (2.24)$$

where $j = 1, \cdots, M$ are the measurement indices, $t = 1 \cdots N_t$ are track indices, C is the density of false measurements, ϕ is the number of false measurements, c is the normalization constant which is sum of probabilities over all feasible events, θ, $\tau_j = 1$ indicates a valid association, $\delta_t = 1$ indicates target detection, and $\delta_t = 0$ indicates clutter detection (obtained from validation matrix).

With the probability of each feasible event now calculated, the probability of measurement j associated to track t can be expressed as the sum over all feasible events, θ, where the association is valid.

$$\beta_{j,t} = \sum_\theta P(\theta_{j,t}|Y^k) \qquad (2.25)$$

The missed detection probability which is always possible can be expressed as

$$\beta_{0,t} = 1 - \sum_{j=1}^M \beta_{j,t} \qquad (2.26)$$

where, again, $j = 1, \cdots, M$ are the measurements and $t = 1, \cdots, N_t$ are the tracks.

2.6.3 Kalman Filter with JPDA

Kalman Filter, simply put, is a set of mathematical equations that start with a set of measurements, makes the necessary prediction(s) of the state variables (and other parameters), and then updates/corrects the prediction(s) as new measurements arrive. Kalman Filter is an optimal, recursive data processing algorithm [74]. It is optimal in the sense that the algorithm minimizes the estimated error covariances when the underlying process is linear and the noise is white and Gaussian. It is recursive in the sense that the Kalman Filter doesn't require all the previous data to be stored, just the current state and error covariances. A full derivation of Kalman Filter is outside the scope of this study but is included in [62], [75]. At first glance, a linear process with white Gaussian noise may seem like a theoretical construct, but for a band-limited applications like radar, noise can be considered white. The thermal noise in radar systems are generally considered as Gaussian. The assumption of linearity is also generally true, especially for sense and avoid tracking. However, if the motion has higher order derivative (of position) contents (e.g. in maneuvering targets like military fighter jets), they can still be accommodated by choosing models that take those higher order derivatives into account. As detailed in the descriptions as well as discussed in the previous section (2.6.1), this study focuses on constant acceleration motion model.

As aforementioned, the tracker is initialized after first detection or when a measurement is not associated with any existing tracks. All tracks are initialized with a Gaussian initial state as $\mathcal{N}(x_0, P_0)$, where x_0 is the state variable (obtained from the measurement) and P_0 is the initial state covariance. The Kalman Filter algorithm includes steps as summarized below. Please note that for clarity, the time steps, (k and $k-1$) are shown inside parentheses and

the subscripts denote track t and/or measurement j.

- **Prediction:** As soon as track(s) are initialized, each track's next state and state covariance estimates are predicted using,

$$x_t(k|k-1) = Fx_t(k-1|k-1) \tag{2.27}$$

$$P_t(k|k-1) = FP_t(k-1|k-1)F^T + GQG^T \tag{2.28}$$

where $t = 1 \cdots N_t$ is the track index.

- **Gating:** When new measurements/detections, y, arrive, innovation for each track, t, and measurement, m, pair is calculated using,

$$\tilde{y}_{j,t} = y_j - Hx_t(k|k-1) \tag{2.29}$$

where, $j = 1 \cdots M$ is the measurement index.

Then the innovation covariance, S, is calculated as follows,

$$S_t = HP_t(k-1|k-1)H^T + R \tag{2.30}$$

Note that the time dependence (k) is dropped from S because a new S is calculated for each track at each prediction/gating step.

Finally, a binary validation matrix for each track/detection pair is constructed whose valid entries satisfy the following,

$$\tilde{y}_{j,t}^T S_t^{-1} \tilde{y}_{j,t} \leq \gamma^2 \tag{2.31}$$

- **Update:** The measurements are used to update the state vector as well

as the state covariance matrix as,

$$x_t(k|k) = x_t(k|k-1) + W\tilde{y}_t \qquad (2.32)$$

$$P_t(k|k) = P_t(k|k-1) - (1 - \beta_{0,t})W_t S_t W_t^T + \tilde{P} \qquad (2.33)$$

Note, here $\tilde{y}_t$ has only track, t, as subscript and is the combined innovation for that track which is obtained from the weighted sum of innovation from all measurements as

$$\tilde{y}_t = \sum_{j=1}^{M} \beta_{j,t}\tilde{y}_{j,t} \qquad (2.34)$$

W_t is the Kalman Filter Gain for track t. Again, the time dependence k is dropped (as opposed to other literatures) for the sake of clarity and because Kalman Filter Gain is calculated during each update process for each track using the equation,

$$W_t = P_t(k|k-1)H^T S_t^{-1} \qquad (2.35)$$

The last term in equation 2.33, $\tilde{P}$ is

$$\tilde{P} = W \left[\sum_{j=1}^{M} \beta_{j,t}\tilde{y}_{j,t}\tilde{y}_{j,t}^T - \tilde{y}_t\tilde{y}_t^T \right] W^T \qquad (2.36)$$

After the update step is completed, a new prediction is generated for each track. When a new set of measurement arrives, those predictions are updated which is followed by new predictions and so on. The measurements as well as predictions can be displayed to view the "tracks" as the evolution of target

position. In SAA tracking, the tracks can be used to ascertain the position, speed, and heading of other airborne objects (e.g. another plane, weather, etc.) and change course if necessary. A simulated tracking scenario as well as a real time tracking results will be presented in Chapter 5.

Chapter 3

Signal Processing Algorithm Suite

Digitization of analog signals and data capture capability at various stages have paved the way for numerous signal processing algorithms. Those signal processing algorithms can be categorized under real time and offline processing groups. While it may be desirable to process all algorithms in real time, there are still considerations to be made in terms of computation time, and data collection methods. Some of the algorithms are data driven and/or iterative and therefore are not feasible for real time processing. It is conceivable that, in the future, significant technological advancement can bring a change to this.

PARADOX1 as introduced in chapter 2, is used as an example to realize the various multi-mission signal processing capabilities. To that end, this chapter discusses the different algorithms that are implemented in PARADOX1. Note that the list of algorithms presented here, although extensive, are not an exhaustive list of what PARADOX1 can support.

3.1 Pulse Compression and Matched Filter

Pulse Compression is a signal processing technique in which a code (or a waveform) is modulated in the carrier frequency during transmit and demodulated at receive. Traditionally an unmodulated pulse would be transmitted and

targets situated within the pulse-length (translated to distance) couldn't be resolved. However, using the technique of embedding a code within a long pulse, targets within the pulse can be resolved. At receive, the frequency response of the radar can be thought of as a lowpass filter as the carrier frequency is demodulated out [2]. It is desirable to have a filter that maximizes the Signal to Noise Ratio (SNR) which is one of the most important metric of a radar system as all the processing algorithms and detections depend on it. Such a filter is called Matched Filter. Matched filter is theoretically derived to maximize SNR for a point scatterer in presence of an additive white Gaussian noise. Matched filter can be formally defined as complex conjugated, time-reversed copy of transmitted waveform. Matched filter operation can be realized by correlating returned signal with complex conjugated, time-reversed copy of transmitted waveform. The correlation operation can also be performed as multiplication in frequency domain which can be time efficient especially if the data size is large. Pulse compression and subsequent Matched filtering, in effect, "compresses" the pulse to allow for finer range resolutions and hence the name. The derivation of Matched filter is not included here as the derivation is quite straightforward and included in a variety of radar books [2], [60], [76], [77].

3.2   Adaptive Pulse Compression

Currently, pulse compression and Matched filtering is performed in most modern radars. As aforementioned, Matched filter is theoretically proven to provide the best SNR for a single scatterer when the noise is White and Gaussian. The assumption of White-Gaussian noise holds fairly well in terms of radar for most situations, however, there are exceptions. In addition to deliberate interference/jamming, with ever so busy spectrum, the possibility of inadvertent

interference cannot be discounted. These interferences not only increase the noise floor but also strip away the white Gaussian property of the noise. Then there is the fact that most radars operate in a scene where multiple targets are present. Apart from very specific radar systems (mostly the ones that scan at high elevation angles), all of the radars aim to scan at few kilometers above the earth's surface. Human beings, almost exclusively, operate on and interact with this region of few kilometers above the earth's surface. Naturally, that is where the radar coverage is wanted/needed. The earth's surface itself and the lower level atmosphere present a target dense environment with man made, natural, as well as meteorological targets. Even airborne radars often scan towards the earth's surface. This kind of target rich environment challenges the assumption made during Matched filter derivation and a problem arises in a peculiar way as described below.

Since Matched filter operation is, in fact, the autocorrelation of the transmitted waveform, the output contains autocorrelation sidelobes [78]. These sidelobes can also be thought of arising due to the rectangular-like spectrum of pulse compression waveforms. The sidelobes manifest themselves in time (or range bins in terms of radar) and are in effect energy leakage onto neighboring time/range cells. The sidelobes scale with the target RCS due to which a weaker target can potentially be masked in presence of one or more stronger targets. The range sidelobes can also be viewed as self interference whereby a stronger target masks the returns from nearby weaker targets [79]. There have been ongoing studies to mitigate this issue. Some take the path of designing and optimizing waveforms with lower autocorrelation sidelobes such as linear frequency modulated (LFM) [76], [80], non-linear frequency modulated (NLFM) [81], [82], [83], phase coded waveforms [60], [77], etc. while others take the

path of designing mismatched filters [84], [85], [86].

In recent years, there is an ongoing study on a new class of algorithms that can adaptively develop a filter that is optimal for the environment [78]. These algorithms are data driven and waveform independent. Adaptive pulse compression algorithms can be applied in "raw" I/Q data as well as Matched filtered data to realize an enhanced resolution in range, azimuth, and Doppler domains. This enhancement in resolution is also referred as "super-resolution." Super-resolution can be achieved in time/range domain, angular domain, Doppler domain or in a combination of those domains. A discussion of range super-resolution is presented in [87]. In general, super-resolution is achieved using various optimization algorithms onto the measured data. While some super-resolution algorithms work on oversampled data, oversampling is not a hard requirement for APC algorithms. The availability of high sampling rate Analog to Digital Converters (ADC) coupled with relative low waveform bandwidth ensures oversampling in most modern radar systems. Please note that, in radars, although the carrier frequency is in the order of GHz, the actual waveform bandwidth is in the range of MHz or even KHz. One such algorithm that can produce super-resolution in range using minimum mean-square error formulation is described in [88], [89]. Another algorithm that can offer adaptive pulse compression and subsequent resolution enhancement in range, and azimuth is described in [90]. In this study, yet another adaptive pulse compression algorithm that can achieve enhanced resolution in range, and Doppler domain [56], [57] is described in greater detail.

3.3 Weather Sensing Data Quality Control Algorithms

As the name implies, these algorithms produce an estimation of ground truth in the form of radar variables. For a single polarized radar, the radar products are Reflectivity, mean Doppler Velocity, and Spectrum Width. These products are also called spectral moments. Reflectivity is related to the signal power and is called the zeroth moment. It is mostly a measure of water content in a meteorological element. A detailed derivation of reflectivity is presented in section 2.4 of Chapter 2. The mean Doppler velocity (or the first moment) is the radial velocity as seen by the radar. Spectrum width (or the square root of the second moment about the first moment of the normalized spectrum) is related to the turbulence of (weather) targets in the remote region. A derivation of Doppler velocity as well as a discussion of radar signal spectrum characteristics (extents, location, and width) were discussed in section 2.5 of Chapter 2.

For a dual polarized radar, three additional radar products can be calculated due to the diversity in transmit and receive polarizations. Those are differential reflectivity, specific differential phase, and correlation coefficient. Differential Reflectivity is the measure of difference between horizontally and vertically polarized returns. It can be used to estimate the shape of the remote scatterer which further aids on classifying the type of hydrometeor (e.g. rain, hail, snow, ice, etc.). Specific differential phase is the range derivative measure of difference in propagation phase shifts between horizontally and vertically polarized returns. This difference in phase is caused, in part, by the shape of remote scatterers and therefore can be used to estimate the shape of remote scatterers. Correlation coefficient is the measure of similarity between horizontally and vertically polarized returns. It can be used to measure the consistency of the remote scatters in the resolution volume. High correlation coefficient is indicative

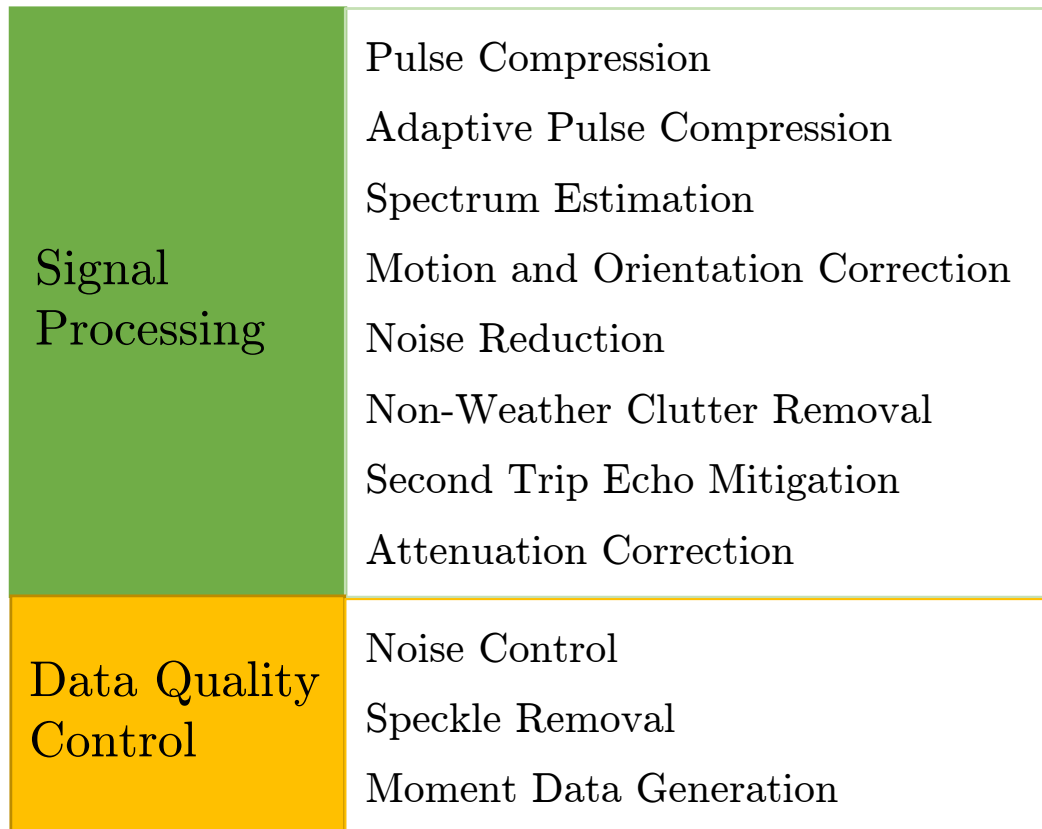|	
Signal Processing	Pulse Compression
	Adaptive Pulse Compression
	Spectrum Estimation
	Motion and Orientation Correction
	Noise Reduction
	Non-Weather Clutter Removal
	Second Trip Echo Mitigation
	Attenuation Correction
Data Quality Control	Noise Control
	Speckle Removal
	Moment Data Generation

Figure 3.1: Processing Framework for PARADOX1 radar

of meteorological scatters while lower correlation coefficient indicates non-meteorological scatters (e.g. birds, buildings, aircrafts, etc.).

Since the current generation of PARADOX is single polarized, this study discusses the single polarized radar products in greater detail. The first step is generally Matched filtering as most modern radar systems employ pulse compression. As discussed in the previous section, there are adaptive pulse compression algorithms which can be applied before or after Matched filter operation. Two such algorithms will be derived and discussed in this study; Iterative Adaptive Approach which is applied before Matched filter operation and Matched Filter base Iterative Adaptive Approach which is applied after
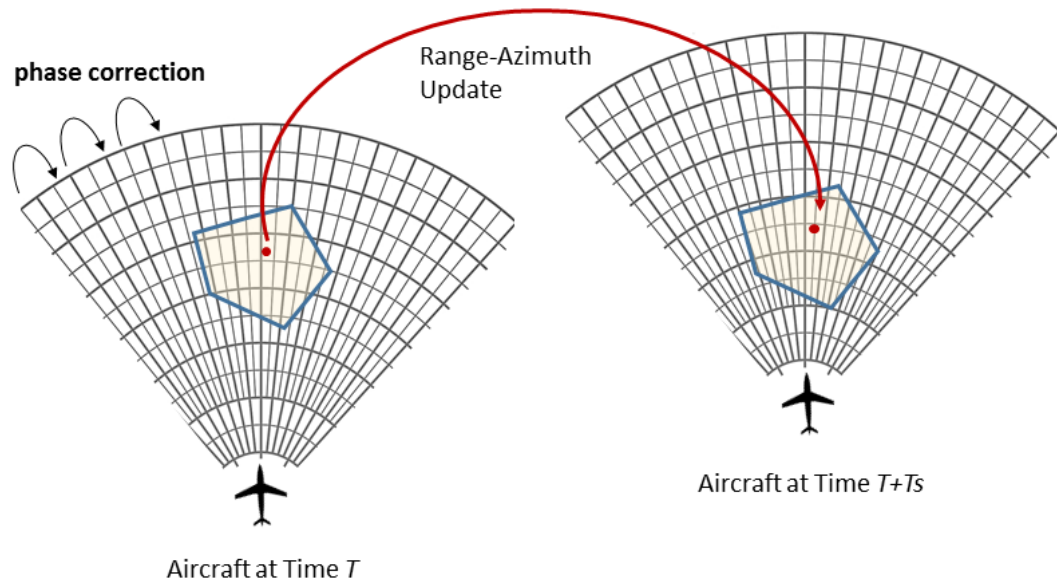
Figure 3.2: Motion Compensation for Micro-Physics Validation mode

Matched filter operation.

Figure 3.1 shows the overall processing framework for PARADOX1. The first step of pulse compression and basic spectrum estimation are carried out inside the radar package, using embedded, real-time processors. The waveform generation and control (which includes choice of pulse-length, bandwidth, windowing functions, etc.) are performed through preloaded scripts. Mitigation of range and antenna sidelobes are performed in the step of the Adaptive Pulse Compression (APC). Note the sequence of algorithm executions in each category (signal processing and data quality control) may not follow the exact order as they are listed in Figure 3.1. Based on different operational modes and radar configurations, they can be adjusted.

3.3.1 Motion Compensation for Micro-Physics Validation Mode

Aircraft motion will have an impact on the measurements for micro-physics validation, severe weather observation mode, as well as target detection of PARADOX1. The affect of aircraft motion on the received data, especially, the spectrum of the received data is well studied [3], [91], [92], [93]. The impacts of aircraft orientation also needs to be corrected for phase, and Doppler as discussed in [94] which is built in PARADOX1 pre-processing. Furthermore, the method of motion correction by using the aircraft navigational systems as described in [37], and [38], is also implemented in the PARADOX1.

For micro-physics validation, the main concern is the range migration of remote scatterers within a scan. Range migration is the phenomena in which remote targets' range bin changes within one unit of measurement (e.g. CPI or a scan). In case of PARADOX1, due to the platform/aircraft motion, range migration is possible in a scan but unlikely in one CPI/dwell. If the micro-physics properties of the weather are sufficiently uniform over the number of range bins aircraft travels through, then we can simply average the radar data along these range gates to "smooth out" the effects of aircraft motion. For many cases, dwell-to-dwell measurements are sufficient, and no spatial compensation is needed. However, for other cases and scan configurations, the spatial distribution of weather/cloud from scan to scan may be of interest. In those cases and for the overall optimal usage of accumulated measurements, a coherence between measurements need to be maintained among the scans. Existing approach [95] which is similar to video encoding and processing through "block-matching" among scan images may be used for motion compensation. This approach is useful for post-processing; whereas for accurate compensation
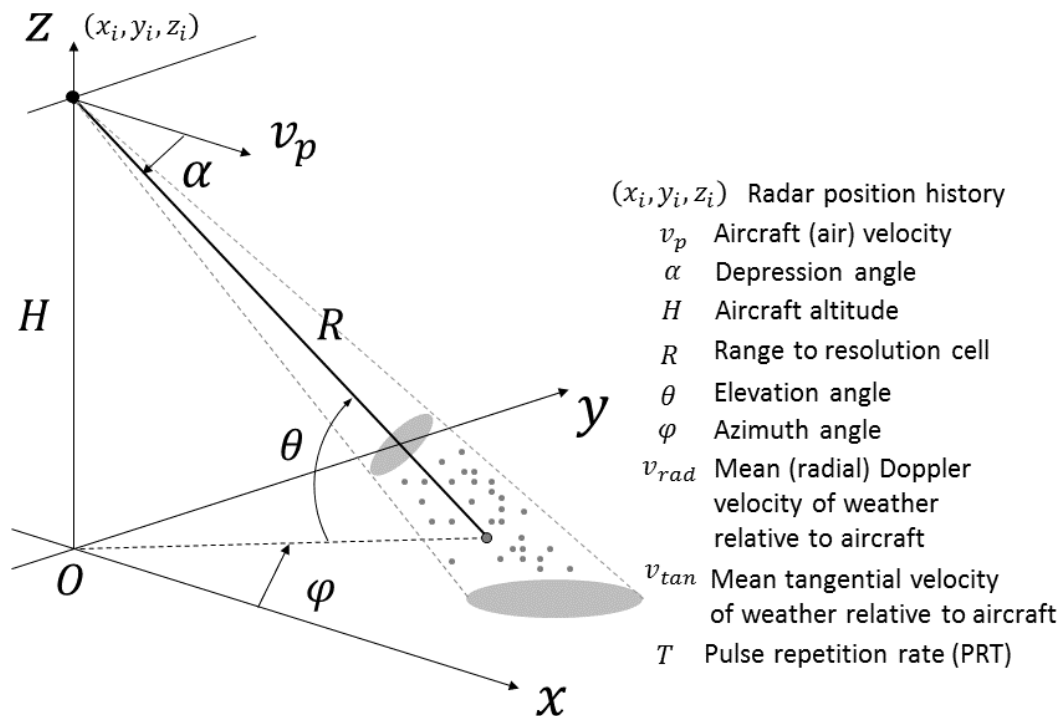
Figure 3.3: Geometry for predicting motion-phase and compensation from distributed scatterers
Obtained from [96]

at the signal processing level, the phase corrections need to be performed at I/Q level of data. A lower-level motion effect mitigation approach for PARADOX1 is "predictive scan correlation" (PSC) algorithm, which is based on an idea of "tracking" the weather blocks from scan to scan. As shown in Figure 3.2, the aircraft performs PPI scans at time T and $T + T_s$, (i.e. each scan takes T_s amount of time). For PARADOX1, T_s is about 3 sec for a 120° azimuthal scan. The scan at time T can be used as a reference to predict how each cell in this scan evolves into a new cell in the next scan. As a result, a progressive and "tracked" state estimation of the same weather block for every aircraft update interval can be established. This motion compensation involves three steps:

1. **Dwell-to-Dwell phase re-alignment:** Phase coherence is maintained

from dwell-to-dwell, so the retrieval algorithms that depend on the phase accuracies, such as KDP computation, in the future, can achieve coherent results over the spatial zone of interest. Range re-alignment is performed from dwell-to-dwell at each range gate where each dwell is correspondent to one radial direction or a range profile. Small range re-alignment based on applying a progressive phase correction for a number of consecutive pulses or dwells is applied to the received signal to compensate the motion of platform at adjacent dwells. The phase compensation is based on the following relation between the received complex signal s_r and the corrected signal s_l.

$$s_l(\phi, t) = s_r(\phi, t) \exp\Big[-j\frac{2\pi}{\lambda}\Big\{2v_{rad}mT + \frac{v_{tan}^2}{R}(mT)^2+$$
$$(x_i cos\phi + y_i sin\phi)cos\theta - z_i sin\theta\Big\}\Big] \quad (3.1)$$

for $m = 1, 2, \cdots, M$ pulses where $v_{rad} = v_p cos\alpha$ and $V_{tan} = v_p sin\alpha$. The associated geometry is depicted in Figure 3.3.

2. **Scan-to-Scan tracking:** The relative velocity of the weather block is used to predict the location (updated range and azimuth) of the weather block in the next scan. This step is similar to [95] while using predictive motion alignments rather than inter-frame matching.

3. **Signal calibration:** A power level adjustment on the weather pixels based on updated relative location to radar and the updated radar resolution volume size is applied for the same weather block. Then the adjusted time series from the previous scan is combined with the time series at the next scan for further processing (such as noise reduction for the weather region of interest).
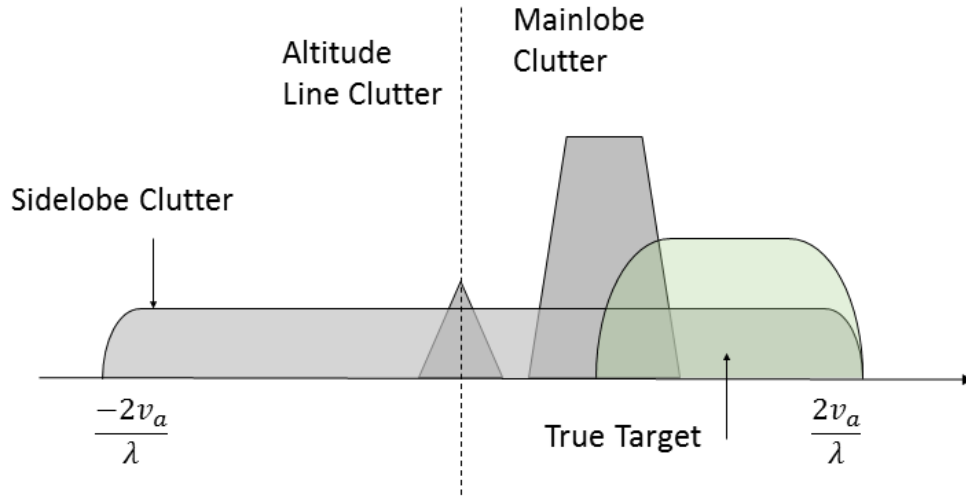
Figure 3.4: Pulsed Airborne Radar Spectrum

3.3.2 Motion Compensation for Severe Weather Observation Mode

For severe weather observation mode, the impact of aircraft motion is mainly on Doppler estimation and Doppler spectrum distortion, which is similar to most airborne pulsed Doppler radars [37], [38], [97]. By knowing accurate air-speed and radar parameters like the antenna center location/orientation, the airborne radar spectrum center can be shifted "back" to be equivalent to a ground-based radar observation. This basic approach derived from [38] has been implemented in previous similar work on airborne remote sensing [47]. Typical airborne radar spectrum contains the desired weather target spectrum and different clutters, which are folded through the non-ambiguity Doppler extents as shown in figure 3.4. In PARADOX1, the altitude line return is usually ignored, and the mainlobe clutter usually centers close to the zero-Doppler line. Spectrum transformation method is used to transform the airborne measured spectrum to an equivalent ground-based radar spectrum,

by removing (shifting) the effects of aircraft motion velocity. This approach is proven to be effective for the existing PARADOX1 data measurements, and has the added benefit of easier implementations down the processing chain using ground-radar based radar algorithms. Mainlobe ground clutters and altitude line clutters will return to zero-Doppler after the spectrum transformation processing, which is removed using typical notch filtering. The sidelobe clutters are more complicated and currently they are treated as enhanced noise power in noise reduction processing. More advanced processing of such clutters can be applied if multiple phase centers are available, which is planned for future PARADOX upgrades.

3.3.3 Noise Reduction, Attenuation Correction, and Calibration

A simple technique of thresholding the return power is used as the method of noise control and reduction. For weather sensing, the targets are generally dense. Furthermore, convective storm clouds often have high reflectivity. These high reflectivity weather targets often provide ample SNR to effectively use thresholding as a way of suppressing noise level. Attenuation correction can be performed by adding the range squared dependence to the raw power return. A simple threshold can be kept to avoid overcompensation of clear-air attenuation. The calibrated reflectivity can then be obtained by comparing with well established ground based radars like NEXRAD's PPI or CAPPI (Constant Altitude PPI) which is done by evaluating the reflectivity values from PARADOX1 radar and NEXRAD for the same beam coverage region of weather.

As part of the calibration procedure, in addition to the radar constant cali-
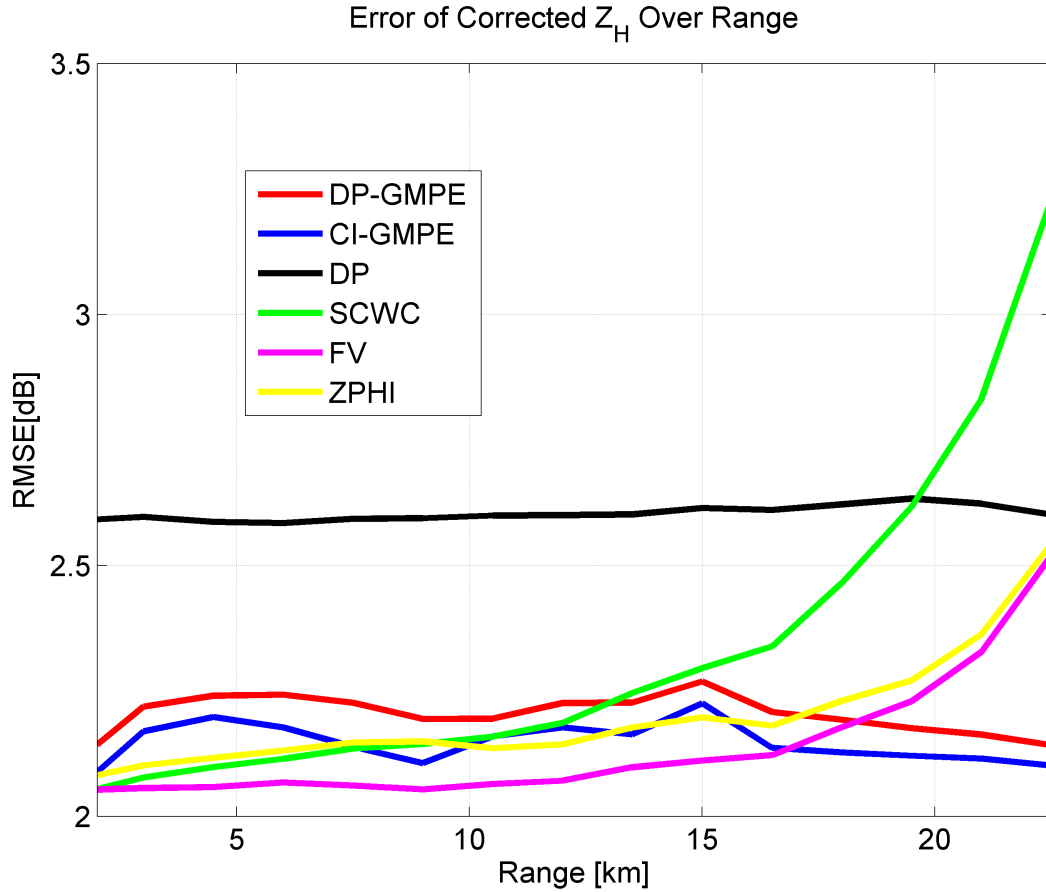
Figure 3.5: Performance of GMPE for X-band attenuation corrections (using simulated weather radar range profile based on weather models) and comparison with existing technologies. DP: Phase Parametrization, CI: Constant Iterative, FV: Final Value, SCWC: Self-Consistent With Constraints
Obtained from [61]

bration and range square dependence calibration, atmosphere attenuation due to hydrometeors need to be corrected for weather radars operating at X-band or higher frequencies. For example, based on numeric hazard detection simulations, the impact of path attenuation can reduce the hail detection probability to 30-40% compared to attenuation-free detections. The GMPE (Gaussian-Mixture Parameter Estimator) trained by Monte-Carlo simulations has been successfully developed for attenuation correction and has been compared to

existing methods (as shown in Figure 3.5, with more detailed discussion in [61]). GMPE not only demonstrated lower averaged "Root Mean Square" errors, but also revealed a rather "even" level of errors through the range. This is a big advantage over other techniques, which have either a higher level of estimation error (such as the power-law related approach), or possible accumulation of errors in cases with longer range. GMPE based attenuation estimation is appropriate for radars with a longer observation range, thus providing a possible earlier warning of "weather hazards behind hazards".

3.3.4 Doppler and Spectrum Width Estimation

Motion compensated spectrum is used to estimate proper Doppler velocity and Spectrum Width. Basic algorithms for estimating radial velocity and spectrum width use standard the Lag-1 and Lag-2 pulse-pair estimators as described in [3]. Selecting a higher PRF allows more accurate estimate of velocity (as the Doppler spectrum has wider span and therefore includes more of the non-aliased spectrum peak due to higher velocities) while at the same time decreases maximum unambiguous range. The maximum unambiguous velocity as expressed in equation 2.11 is,

$$v_{ua} = \pm \frac{\lambda \cdot PRF}{4} \tag{3.2}$$

while, the maximum unambiguous range is

$$R_{ua} = \frac{c}{2PRF} \tag{3.3}$$

The ambiguity relationship between range and velocity can then be expressed as [3]

$$R_{ua}v_{ua} = \frac{c \cdot \lambda}{8} \tag{3.4}$$

where, c is the speed of light and λ is the wavelength. Therefore, PRF selection impacts not only velocity estimates but also range estimates. However, multiple PRF's can be staggered to achieve higher values of the maximum unambiguous velocity while at the same time being able to measure further in range [3], [60]. For example if a second PRF's is chosen such that $PRF_2/PRF_1 = 3/2$, then the maximum unambiguous velocity triples than that of using single, $PRF1$ and doubles than that while using only PRF_2. Additionally, more than two PRF's can be staggered. Furthermore, there are multiple schemes for implementing the staggered PRF's to achieve a non-aliased velocity estimate. The PRF's can be staggered between pulses, dwells/CPI's, or scans.

Since PARADOX1 can support multiple CPI's, different PRF's can be used to increase the maximum unambiguous velocity [98] without changing the maximum unambiguous range. One specific case using this method is presented in chapter 6 of this study. More advanced "multi-lag" algorithms are also possible to use, but are limited by the number of pulses available for airborne CPI's. In the low-SNR cases, noise reduction for Lag-1 phase outputs may sometimes be needed to enhance the quality of velocity estimate. One important aspect is the choice of noise floor, which not only affects the reflectivity result plots after quality control, but also affects the spectrum width estimation results.

3.4   End-to-end Radar Simulator

A multi-mission radar study naturally includes development of novel signal processing techniques and algorithms. These algorithms need to be properly tested and validated for data originating from a variety of radar systems. Each of these radar systems is accompanied by its own set of advantages and shortcomings. While it may be desirable to acquire and operate on a "real" measured data, often, such data could be hard to obtain due to lack of resources. On the other hand, data with certain features prove to be more important for algorithm development. It might be desired to operate on an ideal dataset or data with specific properties like SNR levels or specific radar parameters like waveform, antenna pattern, etc. Furthermore, it is impractical to seek measured data from every conceivable pair of radar parameters and environment variables. Therefore, it is prudent to develop a software based simulation suite that can generate data with various properties originating from various radar/environment combinations. Undoubtedly, such simulator also needs to be able to generate a realistic data.

An end-to-end radar simulator is constructed using various system objects from Mathworks®Matlab Phased Array System Toolbox [99]. A generalized workflow of the simulator is depicted in 3.6 where each block represents a system object. The toolbox is, in essence, an API (Application Programming Interface) that allows creation of, interactions with, and manipulations of various radar system components. For instance, a customized antenna object can be created with a field measured antenna pattern. This antenna can be the sensor for Radiator and/or Collector system objects. The interaction of Radiator/Collector objects with the environment is accomplished through the toolbox routines. The end result is the generation of the data as if it were
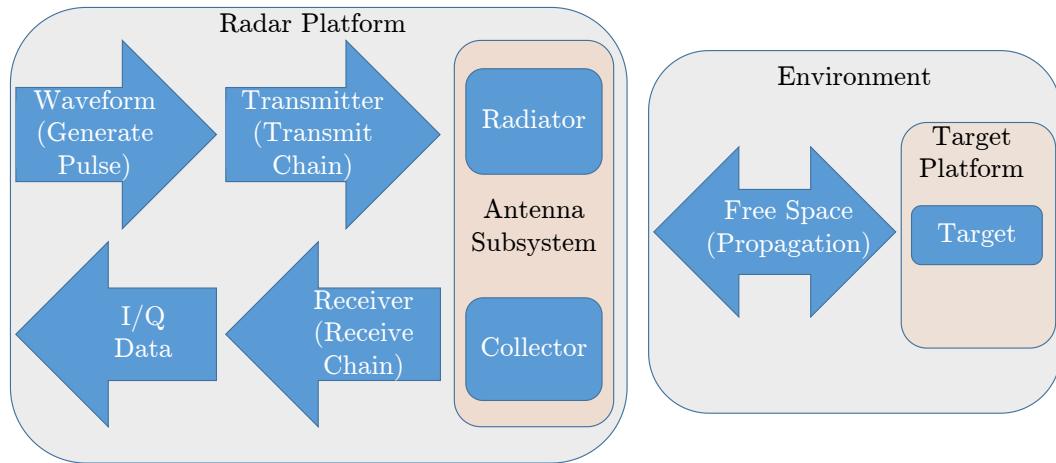
Figure 3.6: Radar Simulator Objects and Interactions

measured by an antenna with the given (field measured) pattern. There are various other objects and routines that not only relieve some of the burden that accompanies a realistic simulation environment but also help reduce the potential for errors.

However, the toolbox is neither an end-all package nor it provides all the required routines that is necessary for radar studies such as this one. Since this study is mostly concerned with the steps after the I/Q data generation, the toolbox is used to generate the I/Q data whenever feasible and appropriate. Advanced signal processing algorithms presented in this study are not a part of the Mathworks®Matlab Phased Array System Toolbox software suite and are fully coded, tested, and validated. The toolbox provides a software based testing and validation platform for algorithms presented in this study.

Although software based radar simulators have been used in various radar studies for a long time, Mathworks®Matlab Phased Array System Toolbox is a relatively new product. The Phase Array System Toolbox based radar simulator is part of an ongoing effort to create software based validation tool. It has been
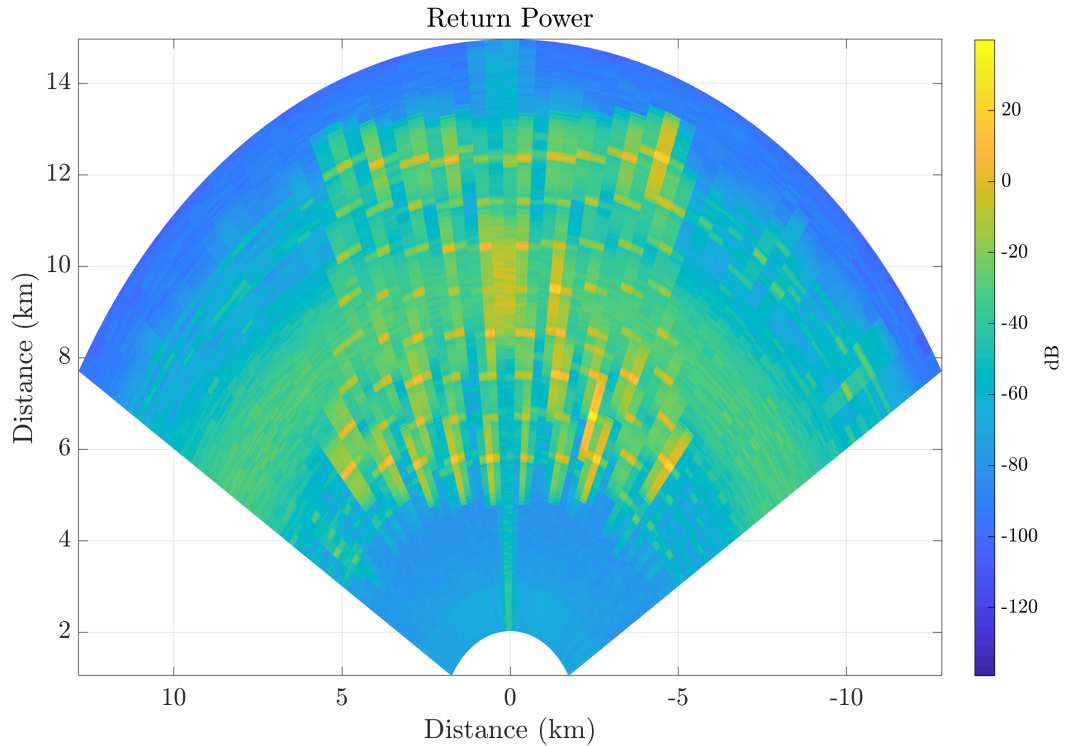
Figure 3.7: Simulated PPI of a Wind Farm
Obtained from [47]

a part of previous studies like [47]. In that particular study, radar returns from Wind Turbines were simulated and machine learning methods were employed to recognize the Micro-Doppler signatures from the Wind Turbine. The radar platform in the simulation was an airborne radar whose parameters matched PARADOX1 system parameters (except antenna whose beamwidth was $\sim 2°$ in the simulation). The scene comprised of the radar scanning downwards, towards a wind farm that contained a moving target. Ground Clutter returns in the simulation were calculated using constant-gamma clutter model. The scan extent was ~15 km in range and $120°$ sector in azimuth with a single elevation angle. Each CPI consisted of 64 pulses with a PRF of 10 KHz. The PPI of the scan is shown in Figure 3.7 which shows the gridded Wind Turbines
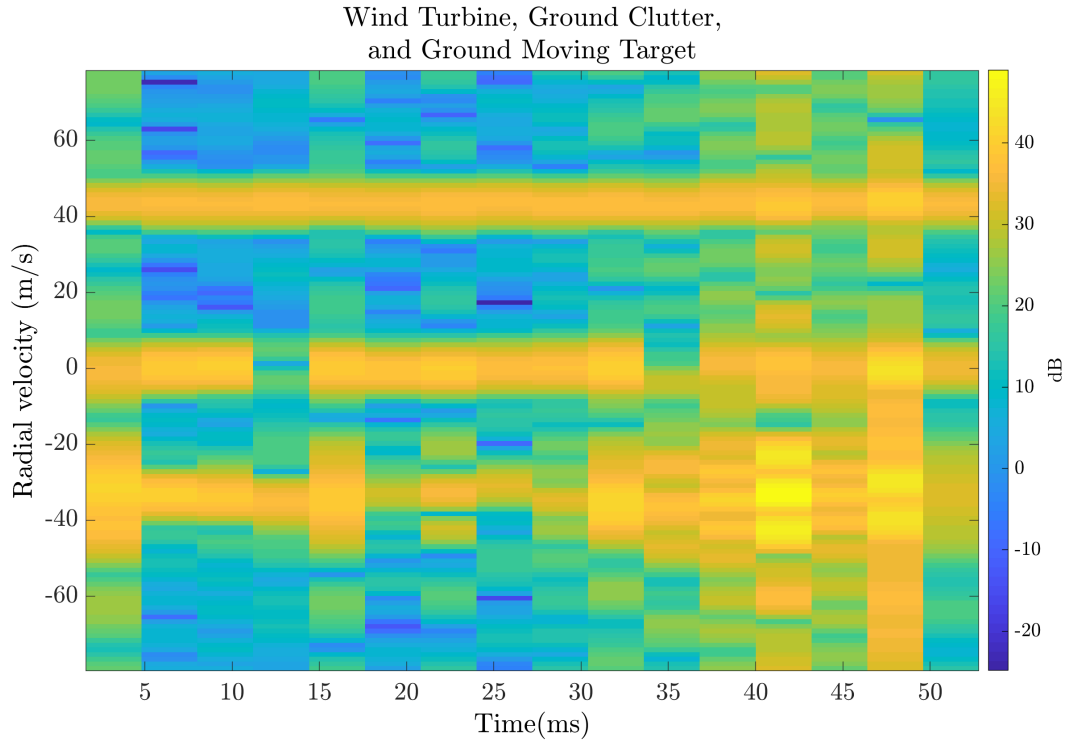
Figure 3.8: Micro-Doppler features of a range-azimuth cell containing Wind Turbine, Ground Clutter, and ground moving target
Obtained from [47]

in the middle of the plot as well as ground clutter at about 10 km in slant range.

In addition to return power calculation, the simulator is also capable of simulating Doppler phase changes due to the target/platform motion. The same study, [47], focuses on recognizing Micro-Doppler signatures and therefore proper calculation of Doppler phase shift in the simulation was necessary. Figure 3.8 shows the Time-Doppler plot of a range-azimuth cell that contains a Wind Turbine, Ground Clutter, and a ground moving target. The constant Doppler (around 0 m/s and 40 m/s velocity) with respect to time are indicative of targets with linear motion with a constant velocity for 50 ms of illumination time. On the other hand, around -40 m/s velocity, there is an apparent spread

of energy in various Doppler bins with respect to time. This spread of energy is caused by the rotational motion of the Wind Turbine blades. The simulator is, therefore, capable of simulating the intricate Micro-Doppler patterns associated with rotating Wind Turbine blades. Please note that the Doppler modulation due to the platform motion is corrected in this plot.

In this study, the simulator is used to generate I/Q as well as Matched Filter returns for validating super-resolution algorithms like Iterative Adpative Approach (IAA) and Matched filter based Iterative Adaptive Approach (MF-IAA). IAA and MF-IAA can enhance resolution in range, and Doppler domain. Both of these algorithms will be derived as well as discussed in greater length in Chapter 4. The simulated data to validate those algorithms were generated using the aforementioned simulator, although, in this case, only a single azimuth/elevation angle were simulated. The results of the simulator will be presented in the context of those super-resolution algorithm discussions.

The simulator was also used to generate a series of scan data which was used to validate Sense and Avoid tracking for a two-target scenario. The simulator in this case played a very important role as flying multiple planes for tracking validation is an expensive endeavor. The results, again, will be presented in Chapter 5 in the context of SAA tracking.

Chapter 4

Real-Aperture Super-Resolution

Cost versus performance trade-off is omnipresent in technology and a radar is not particularly distinct. Especially for an airborne radar, there are additional stringent requirements in size, weight, and power (together referred as C-SWaP). As mentioned previously, this study focuses on software based enhancement to the radar systems as a way of addressing the various shortcomings associated with low C-SWaP systems. One particular area of concern is resolution. It is always desirable to have high resolution in range/angle/Doppler so that targets in close proximity can be properly resolved. However, airborne radars often use relatively small aperture size (12 inches or less) but are still expected to provide enough resolution for proper target discrimination. Low sensor resolution results in wrong information (e.g. number of targets in the scene), inaccurate information (in range, bearing or velocity of the target), and overall degradation of system performance.

One potential cause of such degradation is Matched filter sidelobes which can mask weaker targets in the vicinity of stronger targets. Therefore, an Adaptive Pulse Compression (APC) algorithm is often desired using which the effect of sidelobes can be mitigated while simultaneously enhancing resolution [55], [57], [100]. The APC algorithms are expected to perform at lower Signal

to Noise Ratio (SNR) and support diversified waveforms while minimizing the disruptions to the processing chain of current generation of radars. Such algorithms, many of which are iterative, require intensive computations although real-time implementation is highly desirable in an airborne sense and avoid scenario. Furthermore, Doppler processing is being used as an enhanced approach for sense and avoid tracking process, the result of which is the capability of removing clutter as well as resolution enhancement.

One such APC algorithm is Iterative Adaptive Approach (IAA) [56], [101] and Matched Filter based Iterative Adaptive Approach (MF-IAA) [57]. Both IAA and MF-IAA are non-parametric, iterative, weighted least square based spectral estimation algorithms. IAA algorithm is versatile in the sense that it can also applied to array antennas [102], [103]. The amplitude and phase at the output of those algorithms translate to a resolution enhanced estimate of of RCS amplitude and Doppler frequency of the ground truth. IAA takes its input as non-matched-filtered "raw" I/Q data while MF-IAA does the same with matched-filtered data.

4.1 Problem Formulation

For radar sensing of remote targets, especially from a mobile (airborne) platform, there is a challenge of utilizing limited physical aperture size, dwell time, and signal bandwidth to achieve the best estimate (of remote target properties). Therefore, it is desirable to have algorithms that can mimic an ideal radar system and provide better estimates of target properties (e.g. range, velocity, RCS, etc.). The goal of adaptive pulse compression algorithm is to achieve the best estimate of remote target properties using limited information measured from a non-ideal system. Figure 4.1 depicts a typical scenario and return signal
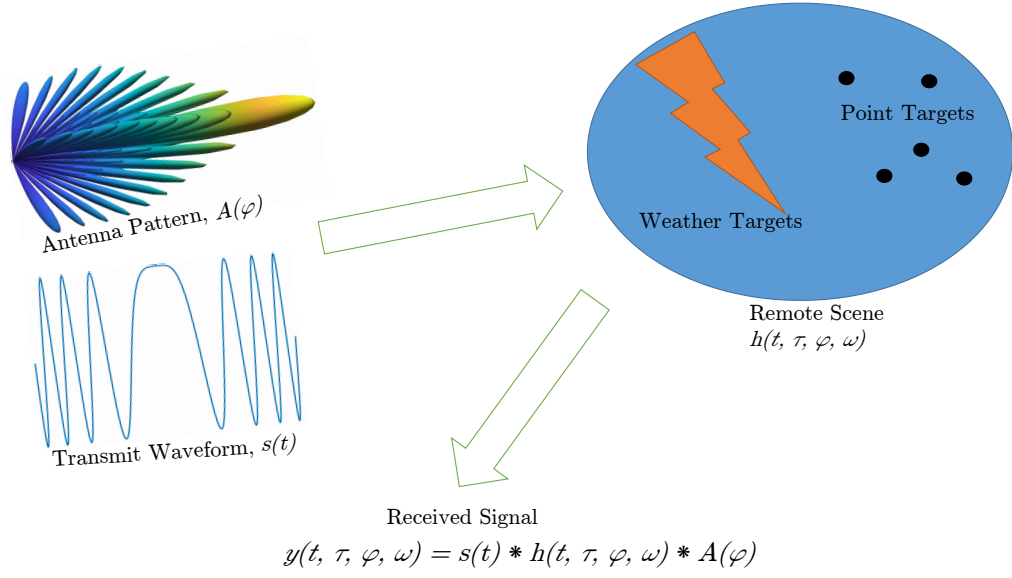
Figure 4.1: Depiction of Radar Signal Model

description for an airborne radar system.

For a radar system transmitting a single pulse where the target is stationary, the return signal to the radar can be modeled as the convolution between the transmitted waveform and complex RCS (corresponding to the targets in the scene) which can be represented as,

$$y(n) = \sum_{k=0}^{N-1} s_k \alpha_{n-k} + \epsilon_n \qquad n = 1, 2, \cdots N \qquad (4.1)$$

where ϵ_n is receiver noise and s is the phase-coded transmit waveform with N subpulses which can be further expressed as,

$$s_k = e^{j2\pi\phi} \qquad k = 1, 2, \cdots N \qquad (4.2)$$

here, α_k is the complex impulse response (of a target) whose amplitude is proportional to radar cross section (RCS) of the ground truth and the phase is

65

the Doppler modulation due to the motion of the target in the kth range cell. Please note that in equation 4.1 the effect of antenna pattern is not taken into account because for a range profile (considering a single azimuth and elevation angle), the antenna pattern is an invariant gain factor which can be removed for simplicity.

4.2   Iterative Adaptive Approach (Single Pulse Case)

A single pulse can be used to estimate Doppler velocity provided the pulse is long enough and the target has high enough velocity. The extreme example of such a system is a continuous wave radar which can precisely measure Doppler velocity. From a mathematical point of view, as long as the target produces a measurable Doppler shift, a proper estimate of radial velocity can be made. The single pulse case of Iterative Adaptive Approach (IAA) is more of a theoretical construct as most modern radar systems are capable of transmitting multiple coherent pulses.

The reflected signal from a stationary target is, simply, an amplitude modulated copy of the transmitted signal and can be expressed as $y = \alpha s + \epsilon$ where y is the returned signal, α is the complex amplitude/voltage response related to radar cross section (RCS) of the remote target, $s = [s_0, s_1, \cdots, s_{N-1}]^T$ is the length N (sub-pulses) transmitted waveform and ϵ is the receiver noise. If the target possesses some radial velocity, an incremental Doppler phase shift would be introduced to the received signal due to the time delay between sub-pulses. The Doppler modulation can be added to the transmitted signal because Doppler shift due to target motion is equivalent to that due to the radar platform motion. In that case, the reflected signal from a moving target

can be expressed as,

$$y = \alpha s(\omega) + \epsilon \tag{4.3}$$

where, $s(\omega) = [s_0, s_1 e^{j\omega}, s_2 e^{j2\omega}, \cdots, s_{N-1} e^{j(N-1)\omega}]^T$. If multiple targets, stationary and moving, are present in the range profile, N continuous return signal from the lth range bin can be written as [102]

$$y_l = \sum_{d=1}^{D} \alpha_{l,d} s(\omega_d) + \sum_{\substack{n=-N+1 \\ n \neq 0}}^{N-1} \sum_{d=1}^{D} \alpha_{l+n,d} \mathbf{J}_n s(\omega_d) + \epsilon_l \tag{4.4}$$

Here, $\alpha_{l,d}$ denotes the complex RCS for l^{th} range bin and d^{th} Doppler bin. There are total L range bins and D Doppler bins. The matrix $\mathbf{J}_n$ is of the form,

$$\mathbf{J}_n = \begin{bmatrix} 0 & \cdots & 1 & \cdots & 0 \\ \vdots & \ddots & & \ddots & \vdots \\ 0 & & \ddots & & 1 \\ \vdots & \ddots & & \ddots & \vdots \\ 0 & \cdots & 0 & \cdots & 0 \end{bmatrix} \tag{4.5}$$

and is a square matrix of size N. $\mathbf{J}_n$ has 1s in n^{th} sub diagonal and 0s elsewhere. $\mathbf{J}_n = \mathbf{J}_{-n}^T$ and $\mathbf{J}_n = 0$ for $|n| \geq N$. As can be seen in equation 4.4, return signal is a composite of reflected signal from the range (and Doppler) bin of interest (l^{th} range bin, and d^{th} doppler bin) as well as reflected signal from the adjacent range bins from $l - N + 1$ to $l + N - 1$ due to propagation time difference among the sub-pulses. With this signal modeling, equation (18-19) in [102] have given the iterative solution to the equations of IAA as,

$$\hat{\alpha}_{l,d} = \frac{s^H(\omega_d) \mathbf{R}_{(i-1)}^{-1}(l) y_l}{s^H(\omega_d) \mathbf{R}_{(i-1)}^{-1}(l) s(\omega_d)} \tag{4.6}$$

For range bins $l = 1, \cdots, L$ and Doppler bins $d = 1, \cdots, D$. The covariance matrix, $\mathbf{R}$, can be calculated as,

$$\mathbf{R}_{(i-1)}(l) = \sum_{n=-N+1-K_l}^{N-1+K_r} \sum_{d=1}^{D} |\alpha_{l+n,d}|^2 \mathbf{J}_n s(\omega_d) s^H(\omega_d) \mathbf{J}_n^T \tag{4.7}$$

4.3   Matched Filter Output

Matched Filter is the complex-conjugated, time-reversed copy of the transmitted pulse. In cases where transmitted signal is known (like in radars), it is theoretically proven to yield the maximum signal to noise ratio (SNR) in presence of additive stochastic noise. The output after applying Matched Filter to equation 4.4 takes the form [56],

$$\hat{x}_l = s^H y_l = \sum_{d=1}^{D} \alpha_{l,d} s^H s(\omega_d) + \sum_{\substack{n=-N+1 \\ n \neq 0}}^{N-1} \sum_{d=1}^{D} \alpha_{l+n,d} s^H \mathbf{J}_n s(\omega_d) + s^H \epsilon_l \tag{4.8}$$

where, $\hat{x}_l$ is the output of the Matched Filter which is (in general) the output of a radar system itself. As in the case of I/Q data (eq 4.4) and apparent in equation 4.8, Matched Filter output doesn't exclusively depend on the target at l^{th} range bin, and d^{th} Doppler bins but also on the targets in nearby range, and Doppler cells. This is shown by the addition of $s^H \mathbf{J}_n s(\omega_d)$ terms. These additions are due to the contributions through sidelobes which often results in sub optimal performance, especially, in target dense environments. Hence, the Matched Filter outputs from multiple continuous range cells can be used to generate a better estimate of the ground truth state. Let $\tilde{x}_l = [\hat{x}_{l-K_l}, \cdots, \hat{x}_l, \cdots, \hat{x}_{l-K_r}]^T$ be the vector of Matched Filter outputs that includes $0 \leq |K_l| \leq N - 1$ neighboring cells in the left and $0 \leq |K_r| \leq N - 1$ neighboring cells in the right around l^{th} range cell of interest [102]. Note that K_l and K_r don't need to be

equal but a balanced filter usually yields better result. $\tilde{x}_l$ can be written as,

$$
\tilde{x}_l =
\begin{bmatrix}
\sum_{d=1}^{D} \alpha_{l,d} s^H J_{-K_l} s(\omega_d) + \sum_{\substack{n=-N+1 \\ n \neq K_l}}^{N-1} \sum_{d=1}^{D} \alpha_{l+n-K_l,d} s^H \mathbf{J}_n s(\omega_d) + s^H \epsilon_{l-K_l} \\
\vdots \\
\sum_{d=1}^{D} \alpha_{l,d} s^H s(\omega_d) + \sum_{\substack{n=-N+1 \\ n \neq 0}}^{N-1} \sum_{d=1}^{D} \alpha_{l+n,d} s^H \mathbf{J}_n s(\omega_d) + s^H \epsilon_l \\
\vdots \\
\sum_{d=1}^{D} \alpha_{l,d} s^H J_{-K_r} s(\omega_d) + \sum_{\substack{n=-N+1 \\ n \neq -K_r}}^{N-1} \sum_{d=1}^{D} \alpha_{l+n+K_r,d} s^H \mathbf{J}_n s(\omega_d) + s^H \epsilon_{l+K_r}
\end{bmatrix}
\tag{4.9}
$$

Let, $g_n(\omega_d) = [s^H \mathbf{J}_{n+K_l} s(\omega_d), \cdots, s^H \mathbf{J}_n s(\omega_d), \cdots, s^H \mathbf{J}_{n-K_r} s(\omega_d)]^T$, then equation 4.9 can be re-written in a compact form as,

$$
\tilde{x}_l = \sum_{n=-N+1-K_l}^{N-1+K_r} \sum_{d=1}^{D} \alpha_{l+n,d} g_n(\omega_d) + \tilde{\epsilon}_l
\tag{4.10}
$$

where $\tilde{\epsilon}_l = [s^H \epsilon_{l-K_l}, \cdots, s^H \epsilon_l, \cdots, s^H \epsilon_{l+K_r}]^T$. There iterative solution at the ith iteration to equation 4.10 is [101], [102],

$$
\hat{\alpha}_{l,d} = \frac{g_0^H(\omega_d) \mathbf{R}_{(i-1)}^{-1}(l) \tilde{x}_l}{g_0^H(\omega_d) \mathbf{R}_{(i-1)}^{-1}(l) g_0(\omega_d)}
\tag{4.11}
$$

For range bins $l = 1, \cdots, L$ and Doppler bins $d = 1, \cdots, D$. Then the covariance matrix, $\mathbf{R}$, can be calculated as,

$$
\mathbf{R}_{(i-1)}(l) = \sum_{n=-N+1-K_l}^{N-1+K_r} \sum_{d=1}^{D} |\alpha_{l+n,d}|^2 g_n(\omega_d) g_n^H(\omega_d)
\tag{4.12}
$$

4.4 Doppler Shifted Matched Filter

Equation 4.8 formulates the Matched filter operation without Doppler phase shift. Effectively, the Matched filter operation is conducted assuming zero Doppler modulation in the returned signal. This is potentially a cause for

degradation in SNR as the Doppler modulation within sub-pulses do not match. Equation 4.8 can be updated to reflect the sub-pulses Doppler modulation as follows,

$$\hat{z}_{l,q} = s^H(\tilde{\omega}_q)y_l = \sum_{d=1}^{D} \alpha_{l,d} s^H(\tilde{\omega}_q)s(\omega_d)+$$

$$\sum_{\substack{n=-N+1 \\ n \neq 0}}^{N-1} \sum_{d=1}^{D} \alpha_{l+n,d} s^H(\tilde{\omega}_q)\mathbf{J}_n s(\omega_d) + s^H(\tilde{\omega}_q)\epsilon_l \quad (4.13)$$

where, $\tilde{\omega}_q$ is the Doppler-shifted Matched filter. Note that $\tilde{\omega}_q$ may not be necessarily from the Doppler bins set $\{\omega_d\}$ nor it needs to be within the Doppler interval of interest. However, it may be desirable to select $\tilde{\omega}_q$ from the set of Doppler bins $\{\omega_d\}$. Matched filter responses from multiple Doppler bins may be grouped together for further processing. Let $\tilde{z}_l = [\hat{z}_{l,1}, \hat{z}_{l,2}, \cdots, \hat{z}_{l,Q}]^T$ be such a vector where Q is the total number of Doppler bins where Matched filtering is performed. $\tilde{\mathbf{z}}_l$ can be expressed as,

$$\tilde{\mathbf{z}}_l = \begin{bmatrix} \sum_{d=1}^{D} \alpha_{l,d} s^H(\tilde{\omega}_1)s(\omega_d) + \sum_n \sum_{d=1}^{D} \alpha_{l+n,d} s^H(\tilde{\omega}_1)\mathbf{J}_n s(\omega_d) + s^H(\tilde{\omega}_1)\epsilon_l \\ \sum_{d=1}^{D} \alpha_{l,d} s^H(\tilde{\omega}_2)s(\omega_d) + \sum_n \sum_{d=1}^{D} \alpha_{l+n,d} s^H(\tilde{\omega}_2)\mathbf{J}_n s(\omega_d) + s^H(\tilde{\omega}_2)\epsilon_l \\ \vdots \\ \sum_{d=1}^{D} \alpha_{l,d} s^H(\tilde{\omega}_Q)s(\omega_d) + \sum_n \sum_{d=1}^{D} \alpha_{l+n,d} s^H(\tilde{\omega}_Q)\mathbf{J}_n s(\omega_d) + s^H(\tilde{\omega}_Q)\epsilon_l \end{bmatrix}$$
$$(4.14)$$

where, for the second summation, $n = -N+1, \cdots, -1, 1, \cdots, N-1$ and note $n \neq 0$.

If we let $\mathbf{S} = [s(\omega_1), s(\omega_2), \cdots, s(\omega_D)]$ and $\tilde{\mathbf{S}} = [s(\tilde{\omega}_1), s(\tilde{\omega}_2), \cdots, s(\tilde{\omega}_Q)]$, we can express equation 4.14 in a more compact form as,

$$\tilde{\mathbf{z}}_l = \mathbf{F}\alpha_l + \epsilon_l \quad (4.15)$$

where, $\mathbf{F} = \tilde{\mathbf{S}}^H\mathbf{S} = [f_1, f_2, \cdots, f_D]$ and,

$$\epsilon_l = \sum_{\substack{n=-N+1 \\ n \neq 0}}^{N-1} \tilde{\mathbf{S}}^H\mathbf{J}_n\mathbf{S} + \tilde{\mathbf{S}}^H v_l \tag{4.16}$$

Equation 4.15 can be solved using the IAA algorithm. IAA estimation at the ith iteration is,

$$\hat{\alpha}_{l,d}^{(i)} = \frac{f_d^H\mathbf{R}_{(i-1)}^{-1}(l)\tilde{z}_l}{f_d^H\mathbf{R}_{(i-1)}^{-1}(l)f_d} \tag{4.17}$$

for range bin $l = 1, \cdots, L$ and Doppler bin $d = 1, \cdots, D$, where the covariance matrix $\mathbf{R}$ is,

$$\mathbf{R}_{(i-1)}(l) = \sum_{n=-N+1}^{N-1} \sum_{d=1}^{D} |\alpha_{l+n,d}^{(i-1)}|^2\tilde{\mathbf{S}}^H\mathbf{J}_n s(\omega_d)s^H(\omega_d)\mathbf{J}_n^T\tilde{\mathbf{S}} \tag{4.18}$$

Computation of MF-IAA algorithm depends largely on the modified filter length, Q. Selection of ω_q can be flexible and lead to a much smaller filter than the original filter $(Q << N)$ which results in more efficient MF-IAA.

4.5   MF-IAA: Multipulse Case

In most radar systems, multiple pulses are transmitted and received which can be combined to generate a better output using the MF-IAA algorithm. The N continuous returned signal for l^{th} range bin from the pth pulse can be written as [101],

$$y_l(p) = \sum_{n=-N+1}^{N-1} \sum_{d=1}^{D} \alpha_{l+n,d}e^{j(p-1)T_r\omega_d}\mathbf{J}_{-n}s(\omega_d) + \epsilon_l(p) \tag{4.19}$$

where T_r is the pulse repetition time divided by the duration of a single subpulse (numbers of subpulses within one Pulse Repetition Time, PRT). If the return from the pulses $y_l(p), 1 \leq p \leq P$ are stacked on top of each other, the return

takes the form [101],

$$y_l = \sum_{n=-N+1}^{N-1} \sum_{d=1}^{D} \alpha_{l+n,d} p(\omega_d) \otimes (\mathbf{J}_{-n} s(\omega_d)) + \epsilon_l \qquad (4.20)$$

where $y_l = [y_l^T(1), \cdots, y_l^T(P)]^T$, $\otimes$ is the Kronecker Matrix Product, and $p(\omega) = [1, e^{jT_r\omega}, \cdots, e^{j(P-1)T_r\omega}]^T$.

The matched filter response takes the form,

$$\hat{x}_l = s^H y_l = \sum_{n=-N+1-K_l}^{N-1+K_r} \sum_{d=1}^{D} \alpha_{l+n,d} p(\omega_d) \otimes (\mathbf{J}_{-n} \tilde{s}(\omega_d)) + s^H \epsilon_l \qquad (4.21)$$

where, $\tilde{s}(\omega) = [\tilde{s}_{-N+1-K_l}(\omega), \cdots, \tilde{s}_0(\omega), \cdots, \tilde{s}_{N+1+K_r}(\omega)]^T$ and,

$$\tilde{s}_k(\omega) = \sum_{n=-N+1-K_l}^{N-1+K_r} s_n^H s_{n-k}(\omega) \qquad k = -N+1-K_l, \cdots, 0, \cdots, N+1+K_r \qquad (4.22)$$

Note, $\mathbf{J}_n$ here is a square matrix of size $2N + K_l + K_r$ that has 1s in n^{th} sub-diagonal and 0s elsewhere. If we let $f_n(\omega_d) = p(\omega_d) \otimes (\mathbf{J}_n \tilde{s}(\omega_d))$, and $s^H \epsilon_l = \epsilon$ then we can re-write equation 4.21 in a compact form as,

$$\hat{x}_l = \sum_{n=-N+1-K_l}^{N-1+K_r} \sum_{d=1}^{D} \alpha_{l+n,d} f_n(\omega_d) + \epsilon \qquad (4.23)$$

Equation 4.23 can be solved by applying the IAA algorithm [102]. The estimate at the ith iteration is,

$$\hat{\alpha}_{l,d}^{(i)} = \frac{f_0^H \mathbf{R}_{(i-1)}^{-1}(l) \hat{x}_l}{f_0^H \mathbf{R}_{(i-1)}^{-1}(l) f_0} \qquad (4.24)$$

and,

$$\mathbf{R}_{(i-1)}(l) = \sum_{n=-N+1-K_l}^{N-1+K_r} \sum_{d=1}^{D} |\alpha_{l+n,d}|^2 f_n(\omega_d) f_n^H(\omega_d) \qquad (4.25)$$

4.6   Simulation Studies

Iterative Adaptive Approach (IAA) and Matched Filter Iterative Adaptive Approach (MF-IAA) can both produce super-resolution results. Numerical simulations are used to test the overall performance of IAA and MF-IAA against Matched Filter results. The simulation method/software used is described in Chapter 3. While there are multitude of approaches as well as metrics for comparisons, this study focuses more on the impact of waveforms and Signal-to-Noise-Ratio (SNR). The Range-Doppler image from Matched Filter output is generated using FFT-based spectrum estimator and compared against Range-Doppler image generated by the IAA and MF-IAA algorithms. Note that both IAA, and MF-IAA are spectral estimators and their outputs are Range-Doppler images of the scene.

4.6.1   Impact of Waveforms

4.6.1.1   IAA

I/Q returns are simulated for a variety of transmit waveforms and compared against IAA outputs. For the simulations, 20 pulses are transmitted with a Pulse Repetition Frequency (PRF) of 10 KHz. This provides a frequency resolution of 500 Hz in Range-Doppler image using traditional spectrum estimation from Matched Filter output. The Iterative Adaptive Approach (IAA) algorithm attempts to improve the resolution by a factor of 10 (i.e with final resolution of 50 Hz, same as transmitting 200 pulses). The algorithm is iterated 10 times in each case. In the resulting figures, the circles represent ground truth with darker color corresponding to higher SNR for the targets. IAA is used with all 20 pulses in each iteration.
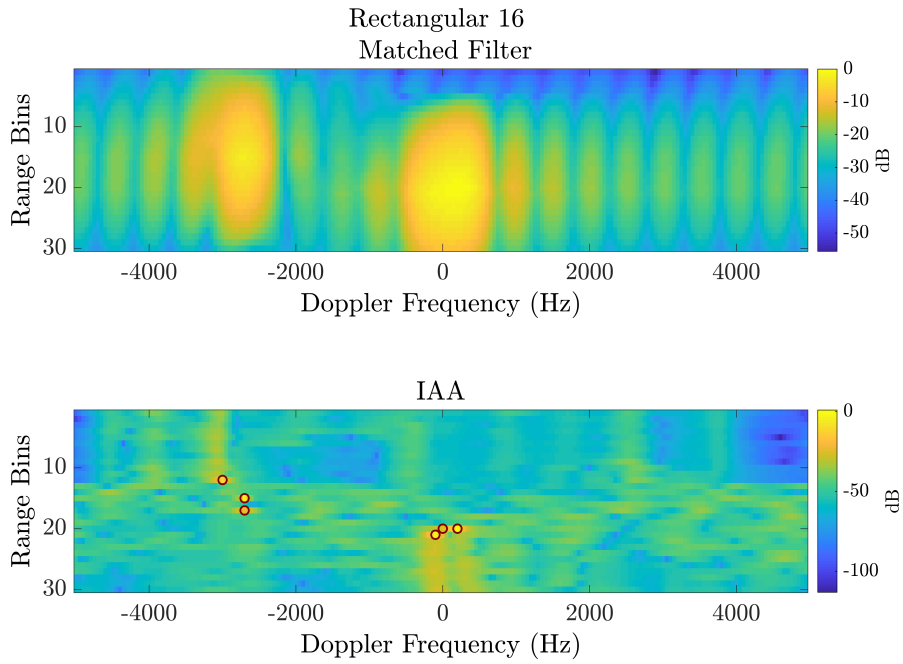
Figure 4.2: Comparison between Range-Doppler Images resulting from Matched Filter and IAA outputs for 16 bits rectangular pulse waveform
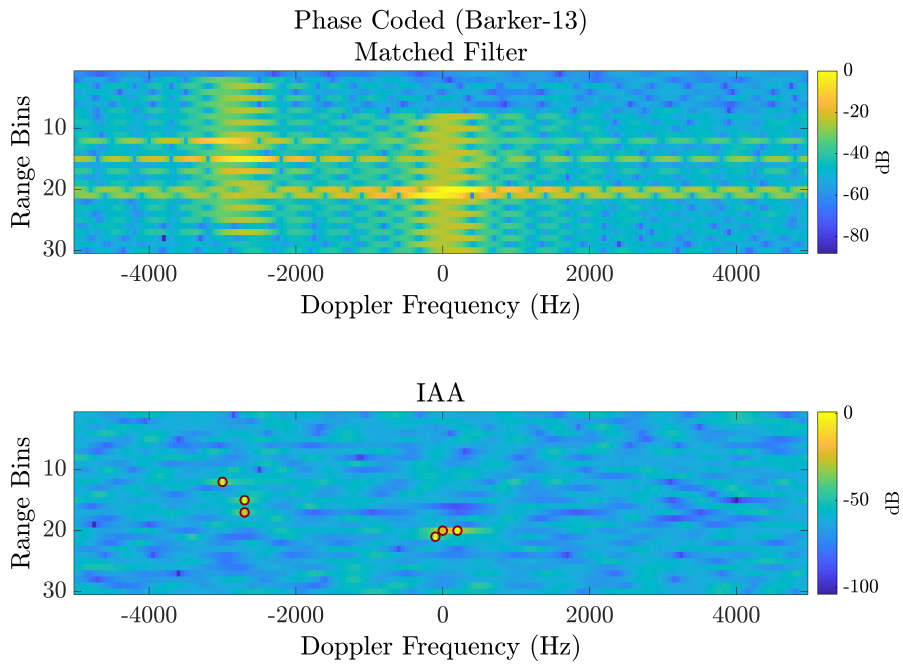

Figure 4.3: Comparison between Range-Doppler Images resulting from Matched Filter and IAA outputs for 13 bits Barker Code waveform
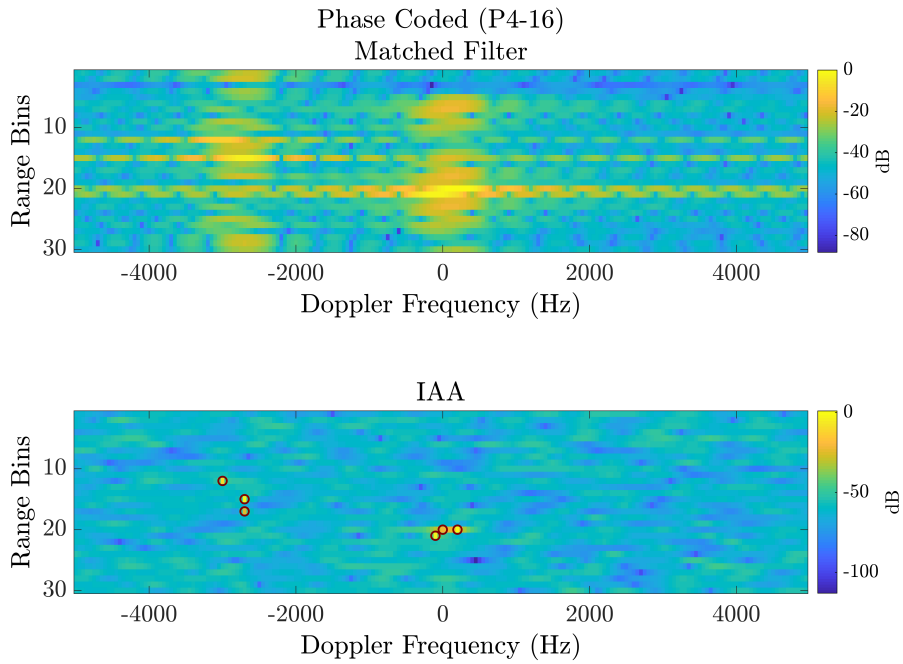
Figure 4.4: Comparison between Range-Doppler Images resulting from Matched Filter and IAA outputs for 16 bits P4 Code waveform
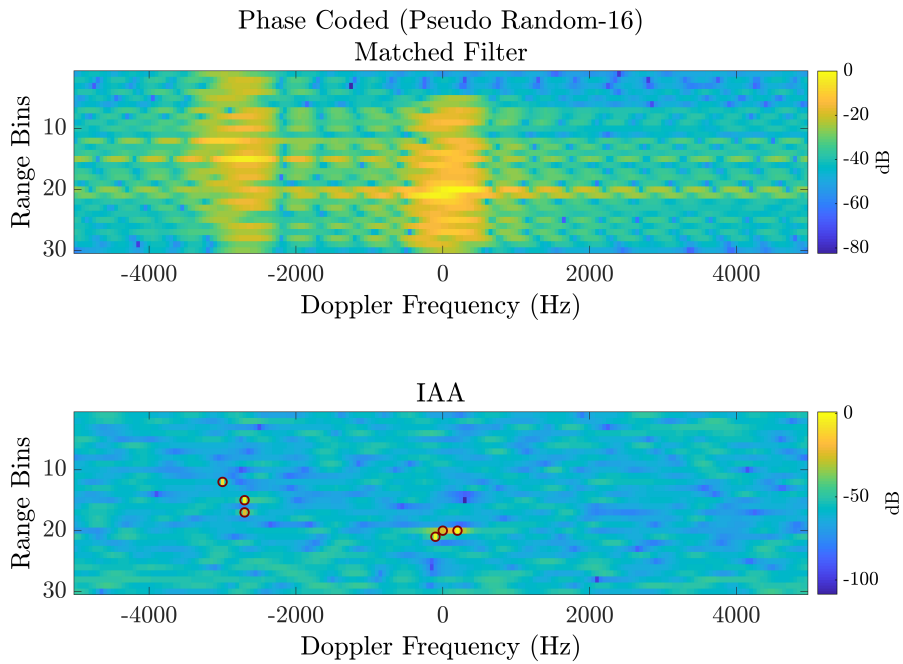

Figure 4.5: Comparison between Range-Doppler Images resulting from Matched Filter and IAA outputs for 16 bits Pseudo Random Code waveform

Figures 4.2, 4.3, 4.4, and 4.5 depict the Range-Doppler image from Matched filter output (the upper portion) and IAA algorithm output (the lower portion) for rectangular pulse, phase coded 13 bits Barker Code, 16 bits P4 code, and 16 bits Pseudo Random code respectively. It can be seen from the figures that IAA does achieve super-resolution in Range-Doppler domain while properly estimating the ground truth. IAA does work for all of the waveforms tested and the impact of waveform has more to do with the autocorrelation function (which is also the matched filter output) of the particular waveform. As anticipated, the rectangular pulse in figure 4.2 has no modulation within the pulse and therefore has the worst performance. For phase coded waveforms with similar lengths (Barker, P4, and Pseudo Random) there are significant differences in Matched Filter based Range-Doppler image whereas there are no significant difference in IAA based Range-Doppler image. Again, these differences in Matched Filter output can be attributed to the autocorrelation function of those waveforms from which IAA doesn't seem to be impacted. While leaving room for future studies, it can be reasonably asserted that the performance of IAA doesn't depend on the type of waveform used.

As aforementioned, there are different methods to use the multiple available pulses. In figures 4.2, 4.3, 4.4, and 4.5 IAA is directly extended to multi-pulse case and all 20 pulses are used in all iterations. Another way of testing is by dividing the pulses in a CPI into multiple groups, applying multi-pulse IAA to each group and then averaging the IAA outputs from those groups. This can potentially improve the SNR by way of averaging and thereby reducing the noise floor. Figure 4.6 illustrates the results for the case of Pseudo Random Phase Coded waveform. There are 20 available pulses from which 4 groups of 5 pulses each are created. IAA algorithm is separately applied in each of
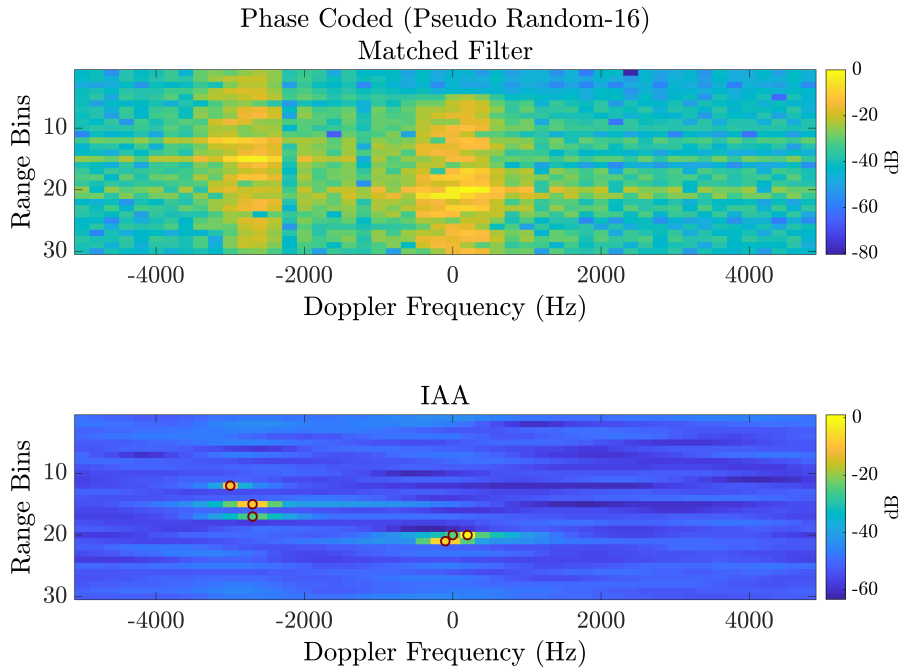
Figure 4.6: Comparison between Range-Doppler Images resulting from Matched Filter output and IAA (obtained by averaging groups of pulses) output for 16-bits Pseudo Random Coded waveform

those 4 groups, then the outputs are averaged, and finally compared to the Matched Filter Range-Doppler output. As can be seen from figure 4.6, when compared to the Matched Filter output, both the Range-Doppler resolution as well as the SNR are improved by applying this technique. This technique of grouping followed by IAA and finally averaging can also be compared against the previous case of using all the pulses once. It can be seen that the averaging technique produces lower resolution (in Doppler) image apparent by the spread of targets' energy in the Doppler bins. The SNR, on the other hand, seems to be better using the averaging technique. The lower resolution but higher SNR is expected as using a smaller number of pulses doesn't quite provide the same resolution as using a larger number of pulses. The averaging process naturally decreases the noise floor value resulting in an increased SNR.
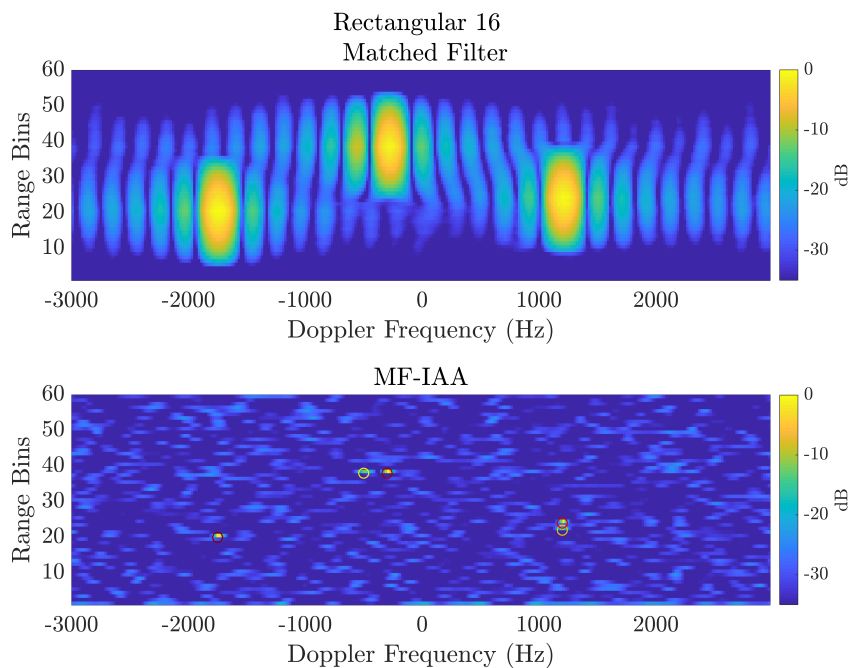
Figure 4.7: Comparison between Range-Doppler Images resulting from Matched Filter and MF-IAA outputs with 16 bits Rectangular pulse waveform

4.6.1.2 Matched Filter IAA

As in the case of traditional Iterative Adaptive Approach, the impact of waveforms were also tested in MF-IAA algorithm and compared against Range-Doppler image from Matched Filter output. In this part of numerical simulations, 30 pulses are used with a PRF of 6 KHz where the SNR is maintained ~ 15 dB. This results in a Doppler resolution of 200 Hz in Matched Filter case while MF-IAA improves the resolution by a factor of 10 (i.e. final Doppler resolution of 20 Hz). Again, the circles represent the ground truth and darker color represent higher SNR for the targets. Similar to the case of traditional IAA, MF-IAA algorithm is also iterated 10 times in each case and in general, the convergence is achieved in less than 10 iterations.

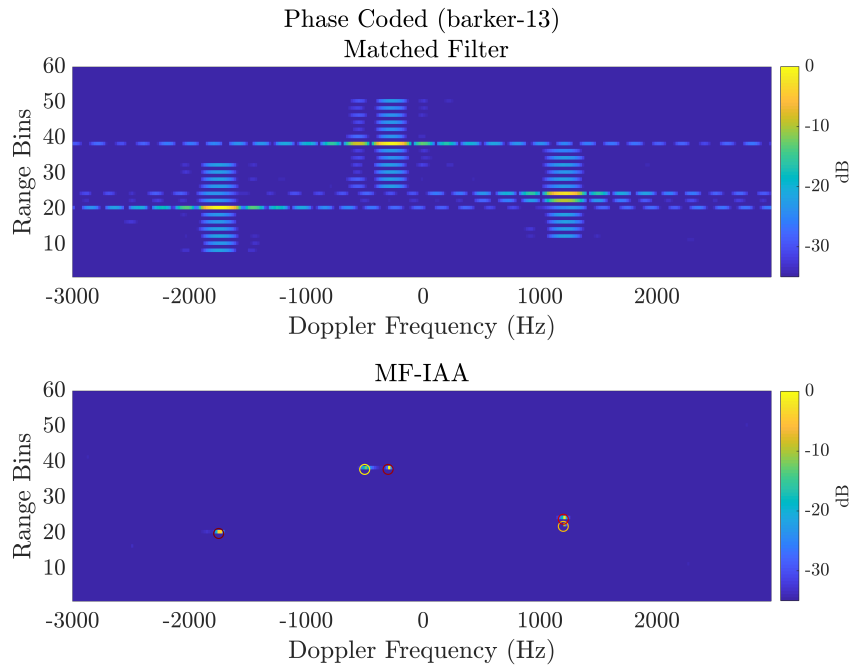The Matched Filter output (the upper portion) and the MF-IAA output

78

Figure 4.8: Comparison between Range-Doppler Images resulting from Matched Filter and MF-IAA outputs with 13 bits Barker Code as waveform
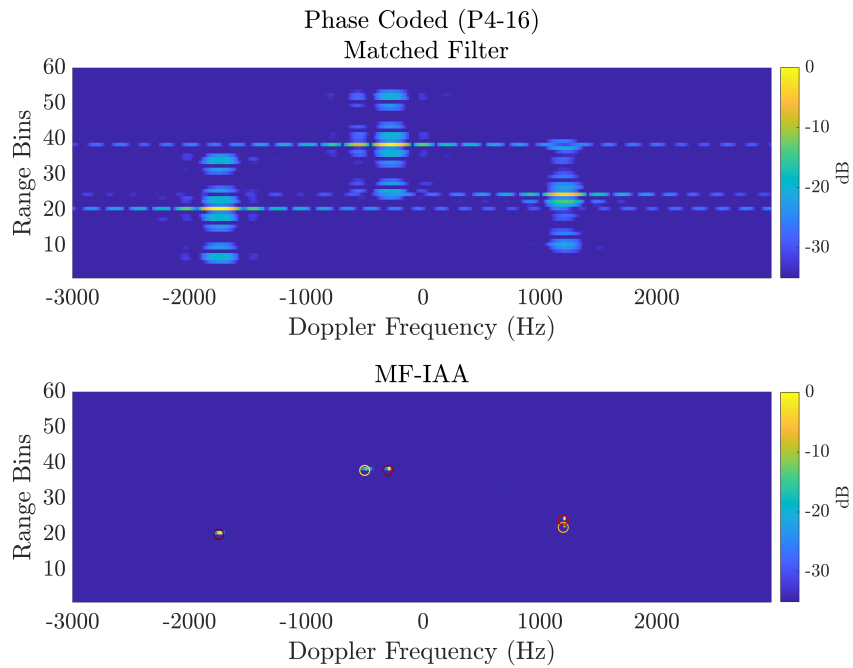

Figure 4.9: Comparison between Range-Doppler Images resulting from Matched Filter and MF-IAA outputs with 16 bits Phase Coded (P4) waveform
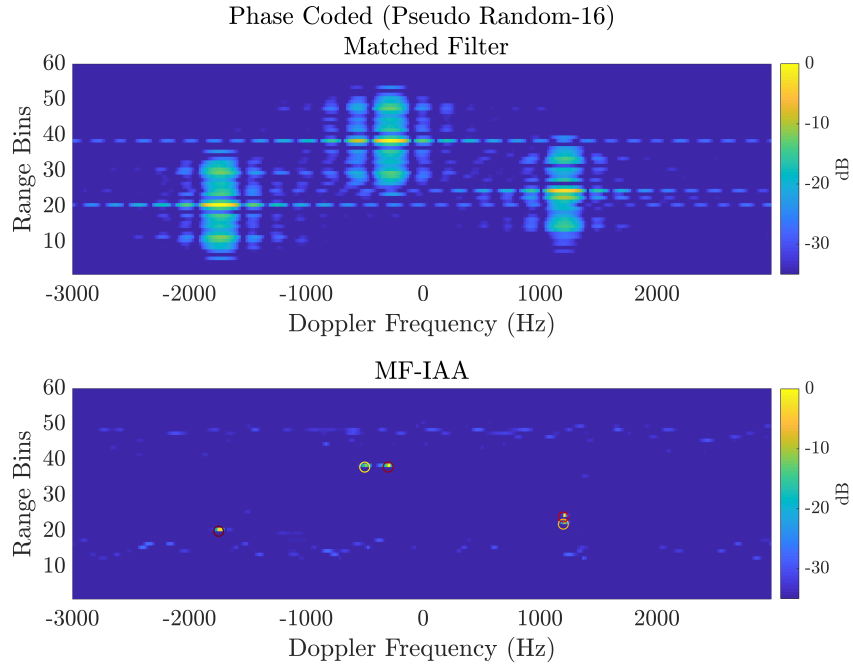
Figure 4.10: Comparison between Range-Doppler Images resulting from Matched Filter and MF-IAA outputs with 16 bits Pseudo Random waveform

(the lower portion) results in Figures 4.7, 4.9, 4.8, and 4.10 aim to compare the impacts of four different transmit waveforms; 16 bits Rectangular Pulse, 16 bits P4 phase coded, 13 bits Barker, and 16 bits Pseudo Random phase coded waveform respectively. As can be seen from figure 4.7, with a rectangular transmit pulse, Matched Filter output does not have good range resolution and suffers with low resolution in (Doppler) frequency domain. The MF-IAA output shows much better resolution in both range and Doppler domains. This is because MF-IAA is able to use the autocorrelation of the transmit waveform while estimating the ground truth. For rectangular waveform, autocorrelation is a "sinc" function which can provide better range resolution. Doppler resolution is a function of number of pulses and sub-pulses transmitted so MF-IAA can properly estimate the Doppler resolution. Figures 4.8, 4.9, and 4.10 show some difference in Matched Filter output; sidelobes of P4 waveform seem to be lower

than that of Pseudo Random waveform while Barker waveform is somewhere in the middle. This is due to the property of the transmitted waveforms themselves, more specifically because of their autocorrelation functions. In MF-IAA case, the noise floor of P4 and Barker waveforms seem to be slightly lower than that of Pseudo Random waveform. As for the targets themselves, P4, Barker and Pseudo Random waveforms have similar resolution both in terms of range and Doppler. Hence, it can be concluded that, while low sidelobe waveforms provide some advantages, the overall performance of MF-IAA is invariant with the type of waveforms used. The results (from MF-IAA) in all cases are better than that of traditional Matched Filter.

4.6.2   MF-IAA: Impact of Signal to Noise Ratio (SNR)

A similar simulation study is performed to evaluate MF-IAA performance with regards to the SNR metric. Similar to previous case, 30 pulses are used with a Pulse Repetition Frequency, PRF, of 6 KHz. The transmit waveform in all cases is a Linear Frequency Modulated (LFM) waveform of length 100 μs with a bandwidth of 6 MHz. Again, the Doppler resolution in traditional Range-Doppler image from Matched Filter output is 200 Hz which has been improved to 20 Hz. The number of iterations remains to be 10 which generally results in convergence.

Figures 4.11, 4.12, and 4.13, show the comparison between Range-Doppler Image resulting from Matched Filter outputs (the upper portion) and MF-IAA outputs (the lower portion) for three different SNR levels while using the same LFM transmit waveform. The circles in MF-IAA results are the ground truth. The varying colors in the ground truth circles represent the target radar cross section (RCS) amplitude. It can be seen that the resolution in range-Doppler
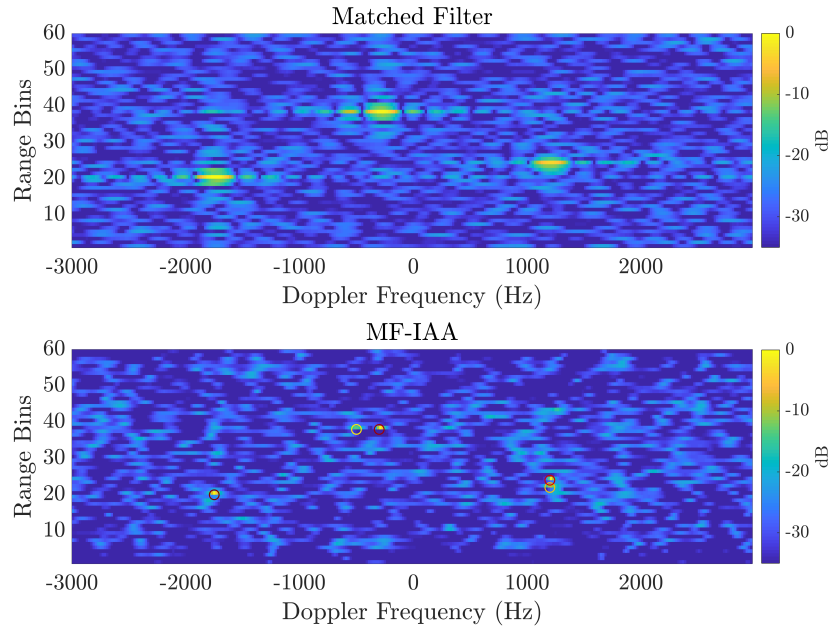
Figure 4.11: Comparison between Range-Doppler Images resulting from Matched Filter (Top) and MF-IAA (Bottom) outputs for SNR $\sim 0dB$ (for each pulse)

domain has improved in all of the three cases. Figure 4.11 depicts the results for the first case where SNR is $\sim$ 0 dB in each pulse. There are only 3 discernible targets in the Range-Doppler plot from Matched Filter output when there are five different targets in the simulation. MF-IAA is able to enhance the RCS signatures of five targets but because of low SNR, the targets are not as distinct as desired. Figure 4.12 shows results from the second case where SNR is $\sim$ 5 dB in each pulse. Again, in the Matched Filter case, there is no proper distinction between the targets while in MF-IAA case, there are five vivid targets. The final case has the highest SNR ($\sim$ 10 dB in each pulse), and is presented in figure 4.13. In Matched filter case, the two targets at the farthest range are more distinct (both targets have same range but different Doppler frequency); however, the two targets in mid-range (same Doppler frequency but distinct and near range) appear as a single target. Two nearby targets
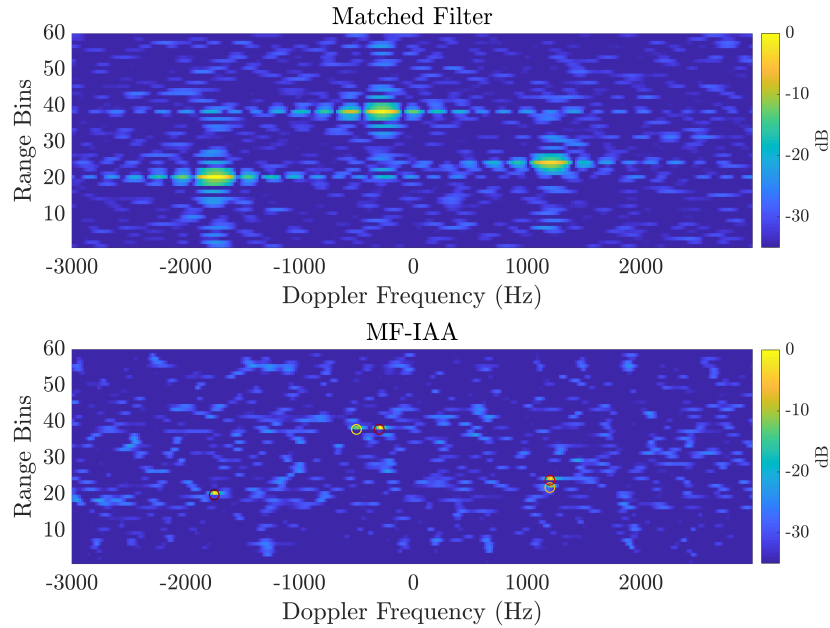
Figure 4.12: Comparison between Range-Doppler Images resulting from Matched Filter (Top) and MF-IAA (Bottom) outputs for SNR $\sim 5dB$ (for each pulse)

with similar Doppler frequency is a common scenario in radar and it can be observed that MF-IAA was able discriminate such targets whereas Matched Filter was not. Hence, it can be agreed that MF-IAA performs better than Matched Filter even in low SNR cases.

4.7   Measurement Data

For validation using measured data, PARADOX1 as described in Section 2.1 of Chapter 2 was used to collect returns from a nearby water tower. The Range-Doppler image generated from Matched Filter output was compared against those generated by IAA and MF-IAA algorithms. In addition, radar returns were collected from an airborne target (Piper Seneca) through coordination with University of Oklahoma, School of Aviation. Those returns were Matched
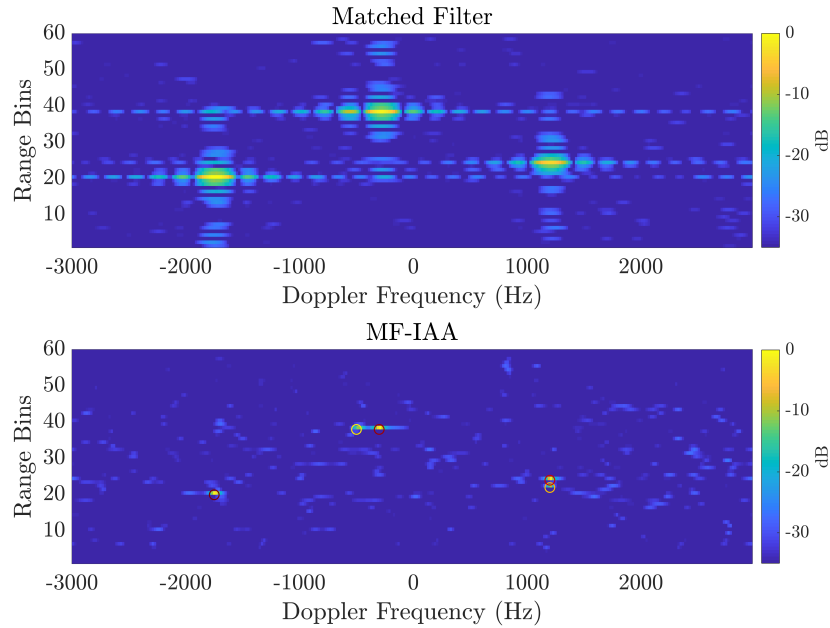
Figure 4.13: Comparison between Range-Doppler Images resulting from Matched Filter (Top) and MF-IAA (Bottom) outputs for SNR $\sim 10dB$ (for each pulse)

Filtered and the generated Range-Doppler image was compared against IAA and MF-IAA outputs.

Figure 4.14 shows the Plan Position Indicator (PPI) scan of a scene that comprises of the water tower about 6.6 km from the radar. A sample range profile, highlighted as the white dotted line in the figure (4.14), is extracted in which IAA and MF-IAA algorithms were applied. Each coherent pulse interval (CPI) in this case consisted of 30 pulses with PRF of 5 KHz (Doppler resolution of about 166 Hz). Both IAA, and MF-IAA were used to enhance the Doppler resolution by a factor of 10 (new Doppler resolution is about 16 Hz). Both results show significant enhancement in resolutions. The water tower target appears in 0 Hz and about 6.6 km in each case. In the IAA case, the individual scattering centers is seen while in MF-IAA just a single target with a weaker range sidelobe is seen. Doppler Resolution in both cases are enhanced; evident
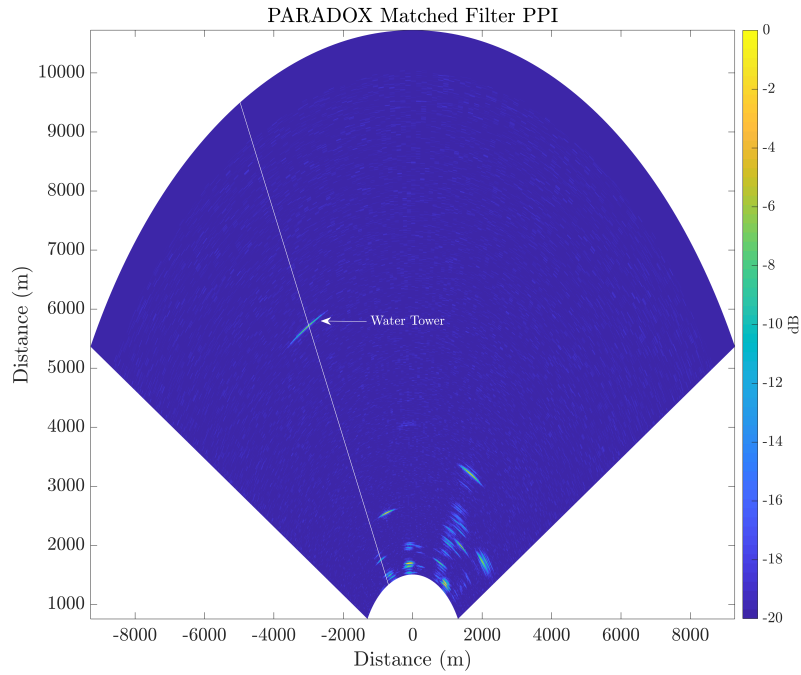
Figure 4.14: PPI Scan from PARADOX1 for a scene containing a Ground Target. The dotted line is the azimuth angle used for IAA and MF-IAA
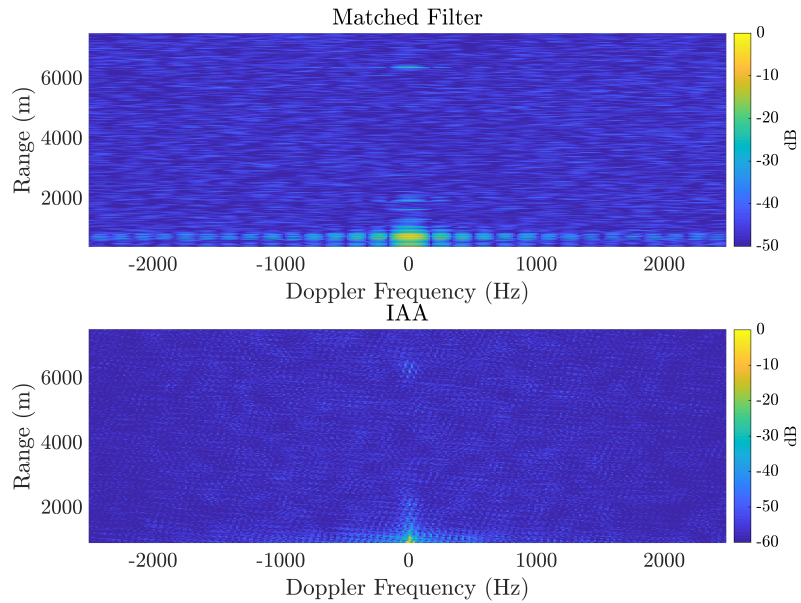

Figure 4.15: Comparison between Range-Doppler Images resulting from Matched Filter Output (Top) and IAA Output (Bottom) for Ground Target (Water Tower)
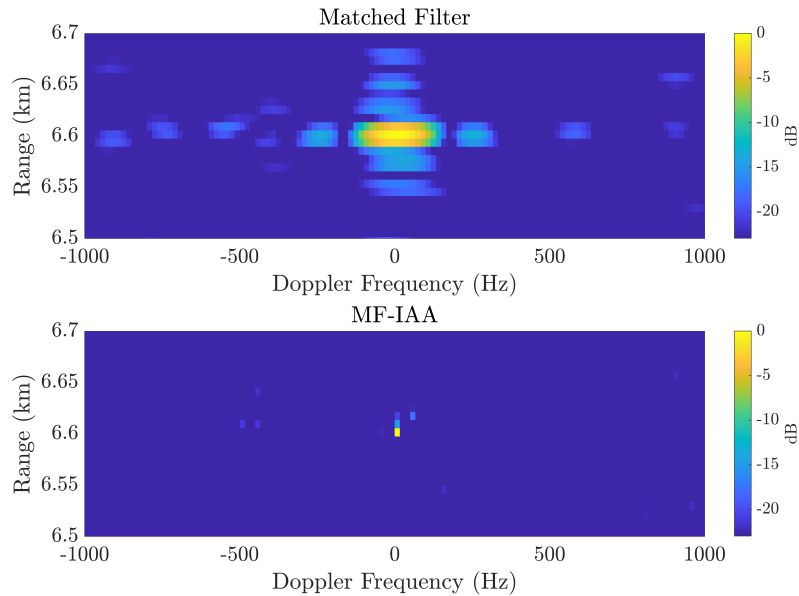
Figure 4.16: Comparison between Range-Doppler Images resulting from Matched Filter Output (Top) and MF-IAA Output (Bottom) for Ground Target (Water Tower)

by the fact that the target spans a single Doppler bin. There are no Doppler sidelobes in the IAA as well as MF-IAA results.

Similarly, figure 4.17 shows the PPI scan of a scene containing an airborne target (Piper Seneca). The PARADOX1 radar was located at the rooftop while the plane flew over in a predetermined path. As in previous case, the dotted white line highlights the range profile extracted for MF-IAA processing. Each CPI in this case consisted of 20 pulses at 5 KHz PRF (Doppler resolution is 250 Hz). Again, MF-IAA was used to enhance the resolution by a factor of 10 (resulting in 25 Hz Doppler resolution). Figure 4.18 shows the Matched Filter output (on the top portion) and MF-IAA output (on the bottom portion). The improvement in resolution can be clearly seen. In contrast to the Matched Filter output, MF-IAA output shows target energy in very few range-Doppler cells, which is a clear indication of enhanced resolution. While the resolution
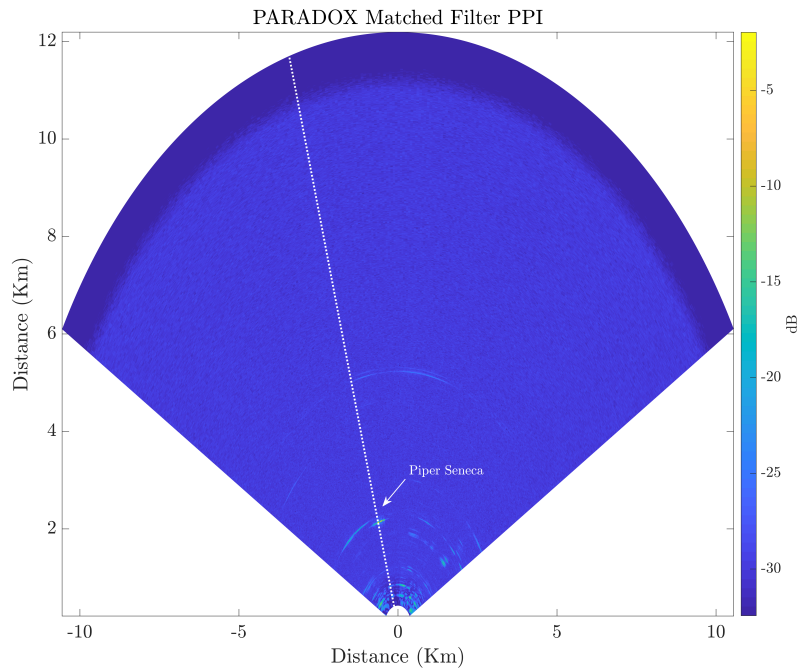
Figure 4.17: PPI Scan from PARADOX1 for a scene containing an airborne target. The dotted line is the azimuth angle is used for MF-IAA
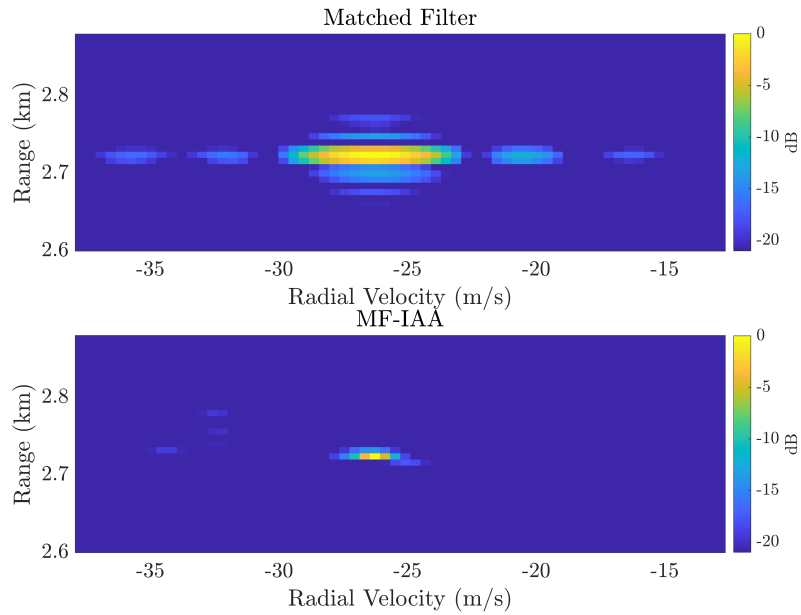

Figure 4.18: Comparison between Range-Doppler Images resulting from Matched Filter Output (Top) and MF-IAA Output (Bottom) for Airborne Target

is enhanced when compared to Matched Filter output, the MF-IAA output show the RCS signature of the airborne target (Piper Seneca) in about two range bins and several Doppler bins. The lack of finer Doppler resolution can be attributed to the small number of pulses in the CPI. The lower SNR of the airborne target (note the Piper Seneca has much less RCS than the water tower) might also have contributed to the suboptimal performance. The Doppler sidelobes can also be attributed to a mismatch in the Doppler shifted Matched Filter estimate. The result from MF-IAA is still a big improvement over the result from Matched Filter and an adequate detection algorithm can easily separate the peak in MF-IAA case.

4.8   Summary and Conclusions

In this chapter, a class of non-parametric, iterative, super-resolution algorithms, namely, Iterative Adaptive Approach (IAA) and Matched Filter based Iterative Adaptive Approach (MF-IAA) are presented. IAA operates on the "raw" I/Q data while MF-IAA operates on Matched Filtered data to produce a resolution enhanced Range-Doppler image. A detailed derivation for both algorithms are presented which starts with a convolution based problem formulation and ends with an optimized iterative solution. The algorithms are tested using simulated data originating from a variety of transmit waveforms as well as Signal to Noise Ratio scenarios. The resulting Range-Doppler images from both, IAA and MF-IAA were compared with those generated from traditional Matched Filter algorithm. The resolution was enhanced by a factor of 10 in each case and both of the algorithms were shown to be waveform independent. The impact of SNR was visible in the sense that higher SNR produced clearer peaks while resolution enhancement was apparent in all SNR levels.

Additionally, the algorithms were also evaluated using field measured data from PARADOX1 radar. PARADOX1 was used in a ground based configuration to measure a nearby water tower target and a general aviation aircraft target. In both cases, both algorithms achieved resolution enhancements when compared with Matched Filter based Range-Doppler Image. While comparing side-by-side, for the airborne target, IAA showed better result than MF-IAA. IAA results had a more distinct peak in Doppler and lower sidelobes in range. MF-IAA results, on the other hand, still had a distinct peak but the sidelobe levels were higher. It is demonstrated that IAA and MF-IAA algorithms can achieve resolution enhancements in range and Doppler domain. Both of those algorithms are validated to be appropriate for a multi-mission radar like PARADOX1.

Chapter 5

Sense and Avoid Function Validations

Sense and Avoid (SAA) tracking is considered as one of the fundamental missions for airborne multi-mission radars like PARADOX1. Indeed, the airspace is getting populated with increasing number of commercial and research vehicles in addition to meteorological as well as natural objects. Therefore, it is necessary to demonstrate SAA tracking capability to designate PARADOX1 as an airborne multi-mission radar. In this chapter, the overall system configuration introduced in section 2.1 of Chapter 2 as Polarimetric Airborne Radar Operating at X-band – Generation 1 (PARADOX1) is used for validation of Sense and Avoid (SAA) tracking functionality. The multi-mission concept depiction was presented in Figure 2.2 of Chapter 2. As mentioned in Chapter 2, PARADOX1 supports attachment of various modules for signal processing. These signal processing modules help achieve improvements such as super-resolution (SR), range/azimuth/Doppler enhancement, sidelobe reduction etc. Currently, **R**eiterated **M**inimum **M**ean **S**quare **E**rror (RMMSE) [104] based deconvolution algorithm is applied for the azimuthal SR and Matched Filter based Iterative Adaptive Approach (MF-IAA) algorithm is used for Range-Doppler SR. To support real-time performance, all the SR processing are performed after Pulse Compression. The target detection is based on a simple "pixel-centroid"
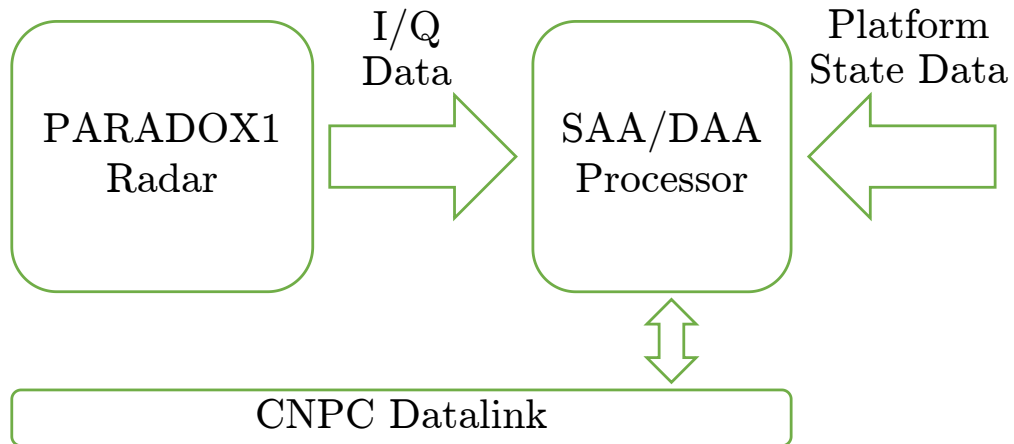
Figure 5.1: Configuration of the Airborne Radar test system

extraction based on [105] from the binary detection output using enhanced pulse compression algorithm. The tracking of multiple collision hazards is implemented through Kalman filter and Joint Probabilistic Data Association (JPDA). A detailed explanation of tracking based on Kalman Filter and JPDA was presented in Chapter 2. The chapter also detailed the motion model used and presented various equations as well as overall algorithm used in tracking. The end-to-end processing chain is validated through both simulations and measurements. The simulation environment is detailed in section 3.4 of Chapter 3. Another novel aspect of this study is the demonstration of the simultaneous monitoring of weather and air-traffic targets through the same aperture and same signal processing chain, which is also tested through measurements.

5.1   SAA Processor and Algorithms

Figure 5.1 shows a simplified block diagram of the current system configuration. The data (I/Q or matched filtered) stream from the airborne radar is transported through Gigabit Ethernet Interface which is then processed in real-time at
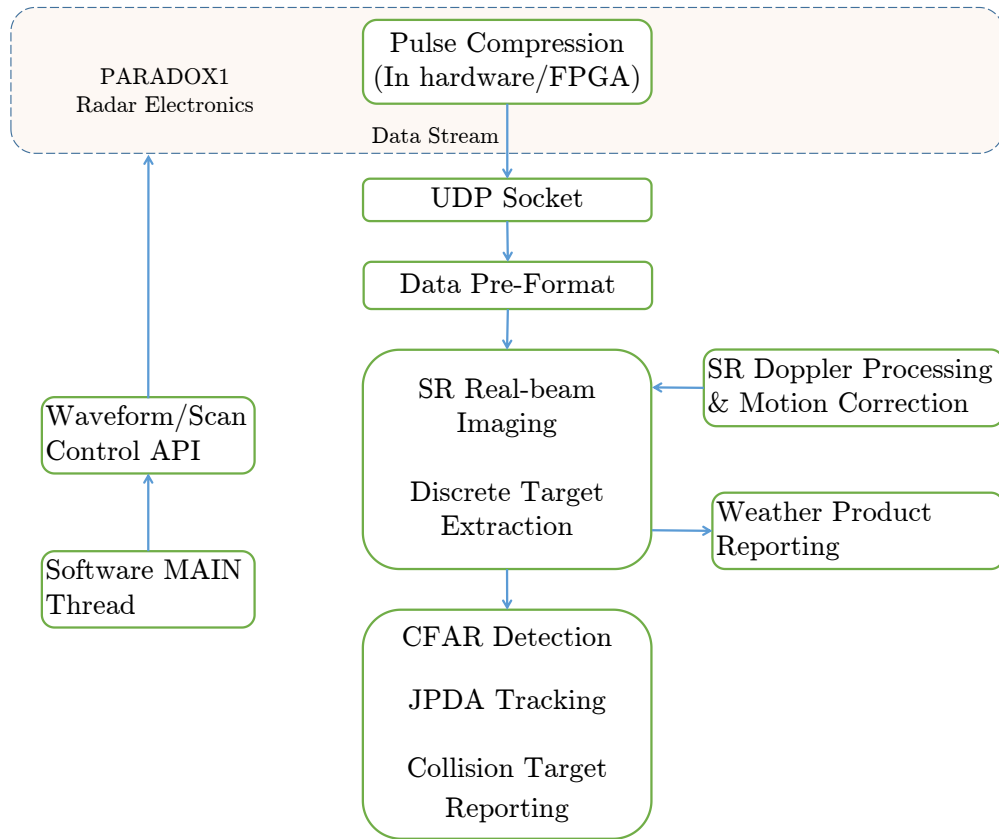
Figure 5.2: Diagram summary of processing flow executed in a SAA/DAA processor

the external processor. A more detailed depiction of the external processor is presented in Figure 5.2.

There are three major steps in the processing flow – data pre-formatting, real aperture (or real-beam scan) imaging, and target tracking. Data pre-formatting is a simple step to organize the scan data into structures that are easy to navigate through; given the processor architecture and programming language used. Real-aperture imaging takes either pre-compressed or post-compressed pulses and generates a scan image, which includes the steps of SR processing, Doppler processing/correction and target detection as well as centroid extraction. This step also classifies different types of hazards (such

as discrete vs distributed) and sends output to programs that handle those different types of hazards. Collision targets are tracked in the third step which include complete logic for track initiation, maintenance, and termination. The focus of this chapter is the SAA radar processor which is currently a small form factor PC. Other embedded processors based on Field Programmable Gate Array (FPGA), and Digital Signal Processor (DSP) are also available but they are not included in this study. In a complete SAA/DAA radar, the SAA processor needs to receive aircraft status data (such as GPS data and orientation information like heading, pitch, roll, yaw) and communicate with other avionics units. The algorithm developed and applied in this chapter is adequate to be executed in either real-time or at a reasonable speed on a simple embedded PC platform.

5.2   Real-Aperture Imaging

Real-aperture imaging is essentially the result from a three-dimensional convolution between antenna pattern, time domain waveform and the target's space-time impulse response. For 2D scan, the problem is simplified as a convolution between azimuth antenna pattern, time waveform, and the target 2D (range-azimuth) response. This concept is illustrated in the Figure 4.1 of Chapter 4. Ideally, an impulse radar with infinite aperture size would be the desired sensor to retrieve the "ground truth" of the targets of interest. In reality, both the aperture size and the waveform bandwidth are limited. The adaptive pulse compression (APC) is introduced in [88] and provides estimation of h from y (as shown in Figure 4.1 of Chapter 4), which is equivalent to emulating an infinite bandwidth, ideal impulse radar through signal processing and software algorithms. Traditional APC algorithms emphasize on resolution

improvements and sidelobe suppression while in real-world, target velocities also need to be discriminated. Super-resolution on Doppler domain is usually achieved through multi-pulse spectrum estimation. One method of Doppler super-resolution was discussed in Chapter 4.

5.2.1   Azimuth Super-Resolution

Azimuth super-resolution (SR) has been studied in the previous studies [106]; in this section, the focus is the effect of SR in the target detection and extraction as well as SAA tracking performance for multiple targets. The distributed target results in the case of weather studies will be presented in Chapter 6. Firstly, each real-beam scan, is converted to a binary image using a threshold, followed by a pixel detection. Center of mass of each group of pixels is recorded as a detected target. If there is a single disconnected pixel, it is discarded considering the fact that most targets illuminate multiple pixels because of higher sampling rate (there are multiple samples in each main-beam coverage) as well as the presence of sidelobes (in range/azimuth/Doppler). Thus, a single pixel illumination is most likely a false alarm. The azimuth resolution is the most significant here. With 6° of mainbeam width, the azimuth or "cross-range" span can reach more than 1 km at 10 km range. In cases with multiple nearby targets, low resolution causes significant detection bias in addition to loss of detection for some targets. This phenomenon causes transmission of wrong information to the tracker resulting in wrong evolution of track and in the worst case loss of a track altogether. To address this challenge, the SR solution overcomes this problem by discriminating discrete scatterers from main beam returns after which proper detection and tracking can continue.

Figure 5.3a shows a scenario with two targets close in both range and

azimuth. The wider beamwidth as well as the azimuthal sidelobes result in a single lumped target as opposed to two discrete targets in the Matched Filter Output. Changing the threshold here offers little benefit as the sidelobes' return from the (left) stronger target is comparable to the mainlobe return from the weaker (right) target. Figure 5.3b depicts the resulting detections from the matched filter output. The "plus" sign shows the truth location whereas the "circle" shows the location where detection was made. There is a single detection in this case, in other words, the tracker's input will have a single target in the wrong location. This will undoubtedly cause wrong evolution of tracks.

Figures 5.4a and 5.4b show the output of RMMSE SR algorithm output and the resulting detections respectively. The two distinct targets are quite vivid in both algorithm's output plot and resulting detection plot. The truth and detection locations in Figure 5.4b match quite well for the target towards the left except for the limitation due to which the lower left grid point of each range-azimuth cell is plotted as the detection point. For the right-side target, there is a bias between detection and truth because there is a bias between measurement and truth which can be observed in both Figure 5.3a and Figure 5.4a. Those detections are more representative of the ground truth and will lead to better tracking performance when compared to tracking done with Matched Filter based detections.

5.3 Simulated multi-target SAA scenario

Since conducting a close by flights using multiple aircrafts was not feasible, a two-target scenario was simulated using MATLAB® Phased Array System toolbox. The details of this simulation environment were presented in Chapter
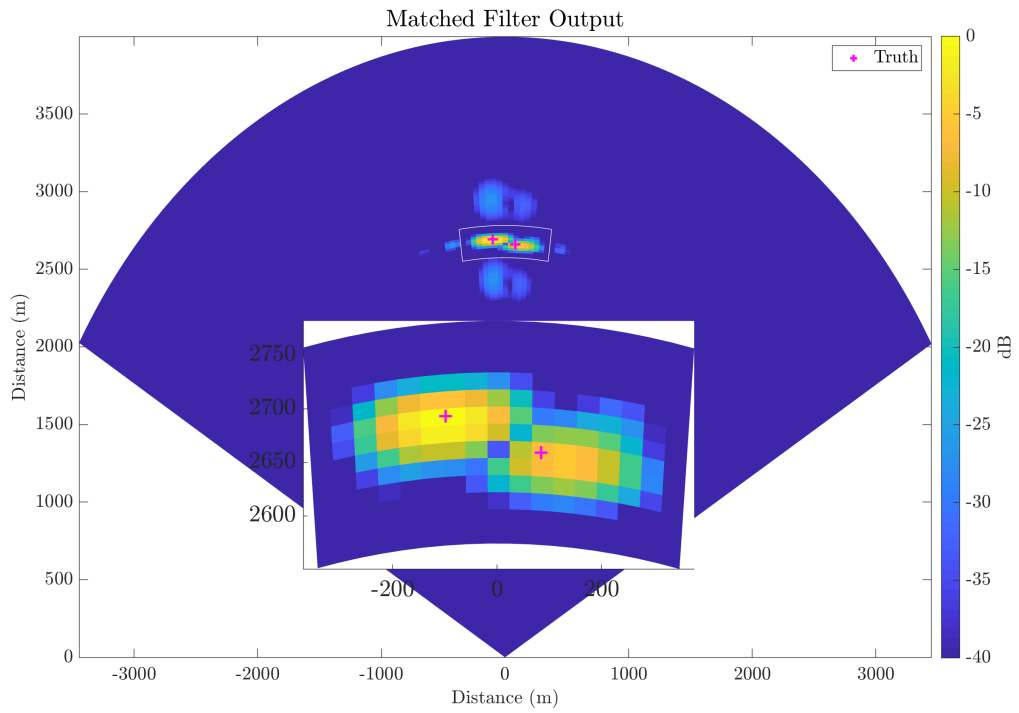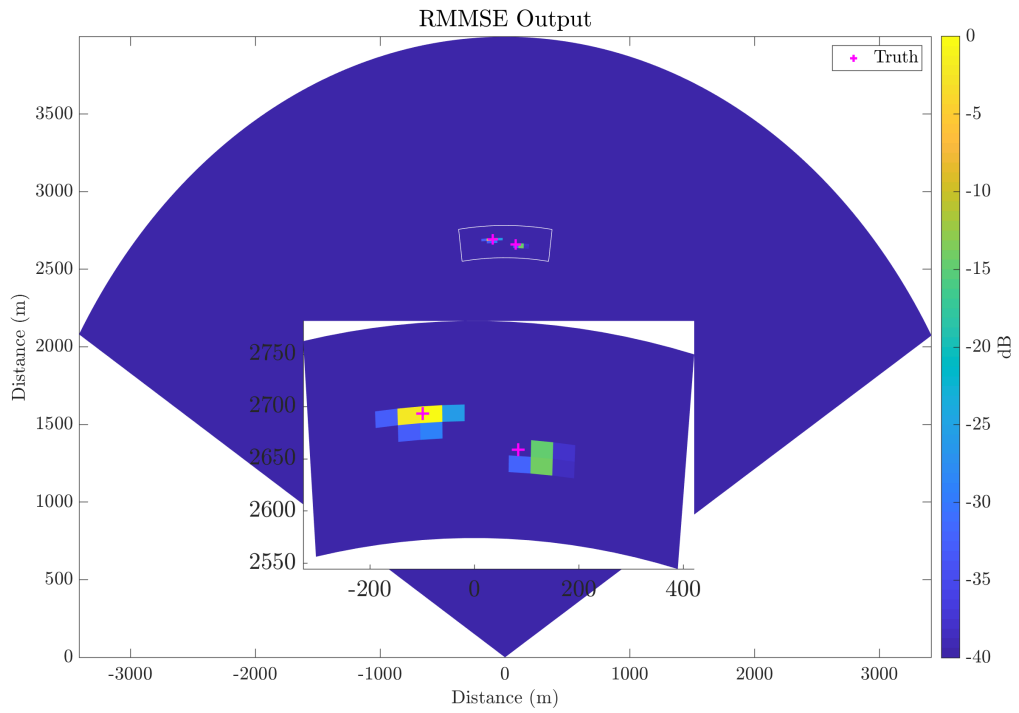
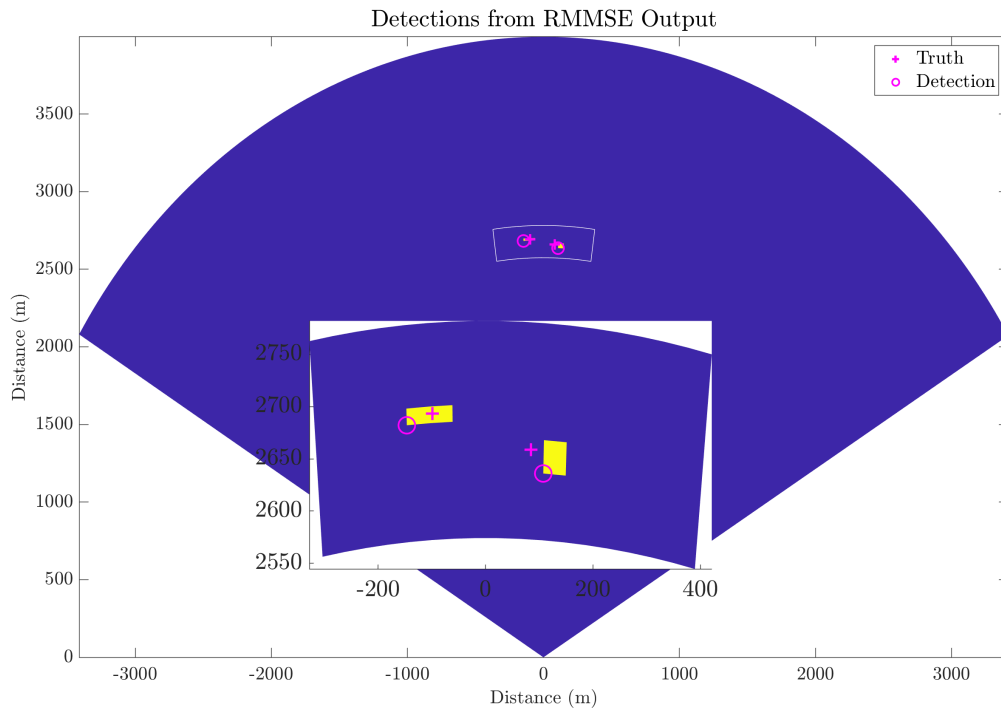(a) Matched Filter Output for two close targets
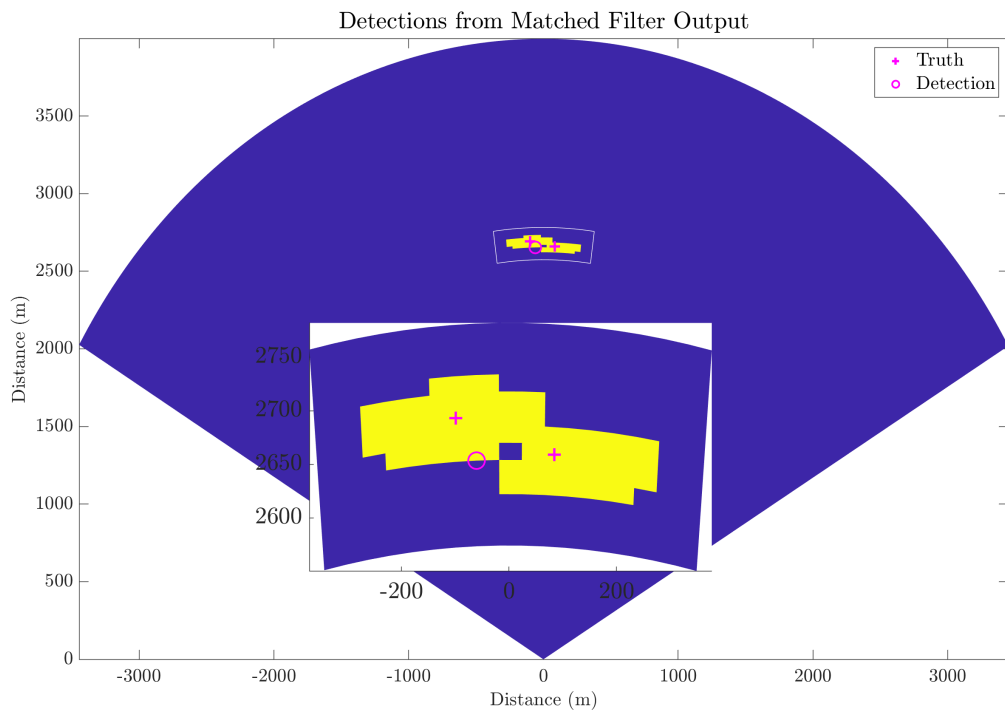
(b) Detections resulting from Matched Filter Outputs

Figure 5.3: Matched Filter output and resulting Detection

(a) RMMSE Super-Resolution Algorithm Output

(b) Detections resulting from Super-Resolution Algorithm Output

Figure 5.4: RMMSE-SR Output and resulting Detection

3. The simulation parameters were chosen to match the specifications of PARADOX1 as described in Table 2.1 except for the antenna. The antenna used for simulation is a linear phased array antenna with 4.5° azimuthal beamwidth. Since all scans are performed in the same elevation, the elevation beamwidth is not significant in simulation. Furthermore, using a linear array (with only azimuth beamforming) instead of a planar array (allows for both azimuth and elevation beamforming) kept the antenna elements at a lower number which eased the computational burden during the simulation procedure. There are two closely moving targets in the simulation scene. The target and the radar positions are updated after each pulse. Random number of false targets are also added at random locations throughout the scan area for each scan to generate false detections. The number of random targets for each scan is generated using Poisson random number generator. Since the simulation is computationally expensive, scans are generated and saved which were later fed into the tracker one scan at a time. In other words, although the simulation and tracking didn't happen concurrently, the tracker still received the data one scan at a time as would happen in a field measurement. This method also allows for an independent evaluation of tracker performance.

The motion model used in SAA tracking is a constant acceleration model (as described in Chapter 2). In this model, process noise is incorporated as perturbations in acceleration. The process noise, itself, is modeled as a Gaussian random variable with 0 mean and standard deviation of 6 m/s^2 in range direction and 2 m/s^2 in cross-range direction. A scan snapshot of Matched Filter output along with its resulting detection as well as RMMSE super-resolution algorithm output along with its resulting detection were shown in Figures 5.3a, 5.3b and Figures 5.4a, 5.4b respectively. These results

were also discussed in the previous subsection (5.2.1). In this section the tracking performance before and after RMMSE super-resolution algorithm will be discussed. RMMSE-SR algorithm is used in this case (as opposed to IAA) primarily because the two targets are in separate azimuth angles. IAA algorithm is used in cases where there are multiple targets in same azimuth angle (same range profile) but with different yet unresolvable range and Doppler frequencies.

Figures 5.5 and 5.6 show tracking results with Matched Filter based detections and RMMSE-SR based detections respectively. Matched Filter algorithm was not able to resolve the two targets adequately which lead to a single detection and finally a single track was formed between the two true tracks. Scan to scan variation of the target RCS caused the detections to spread around the true tracks. Furthermore, some detections also arose from the false targets that were added randomly as described above. In some cases, sidelobes from the stronger target also registered as detection. Since the two targets were not resolved due to low azimuth resolution, most of the detections appear towards the middle of two tracks. This resulted in the formation of a single lumped large target in the binary detection image. Therefore, the detection point was the center of mass of that lumped large target as discussed in section 5.2 and depicted in Figures 5.3a and 5.3b. As a simple threshold detector was used, the trade-off between having the ability to detect smaller targets (by setting lower threshold) and preventing sidelobes registering as targets (by setting higher threshold) became more consequential. Due to the limitation in azimuthal resolution, matched filter based tracker resulted not only in wrong number of targets/tracks but also in wrong evolution/estimation of the track.

In case of RMMSE-SR based detection and tracking, the two tracks are
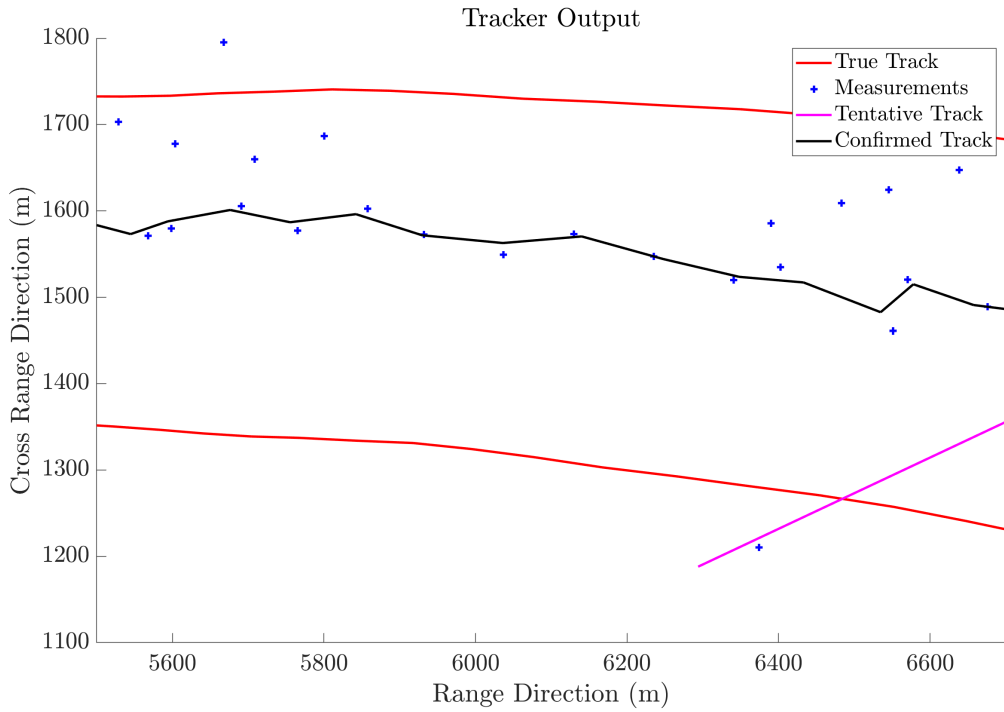
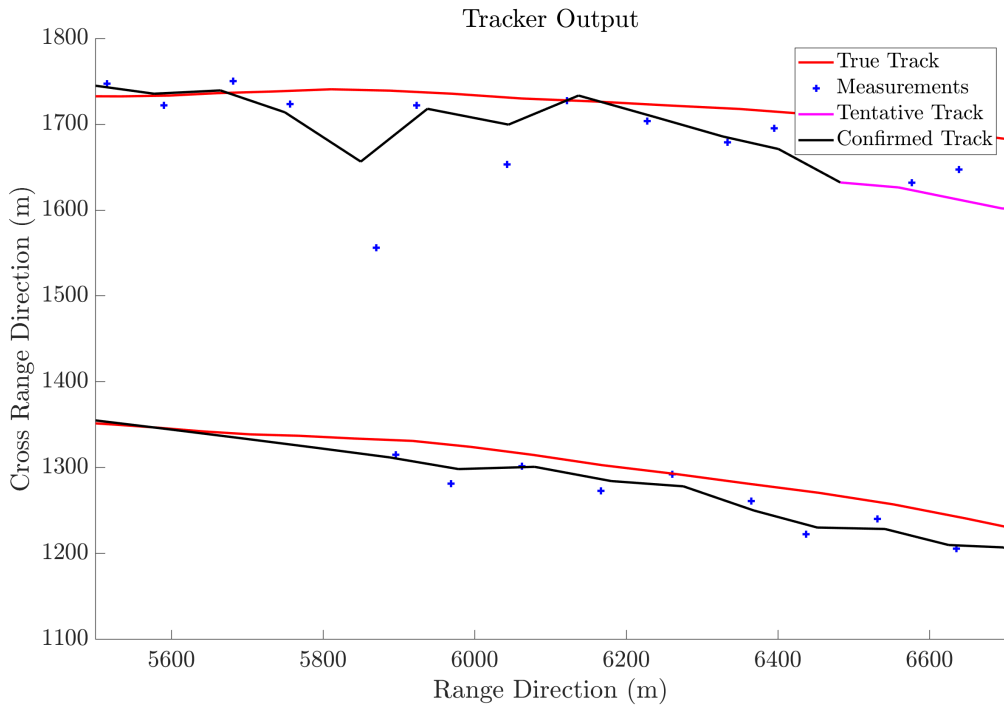Figure 5.5: Tracking Results with Matched Filter based Detections

Figure 5.6: Tracking Results with RMMSE based Detections

clearly visible. Although, there were few detections away from the truth, most of the detections were close to the truth and so were the generated tracks. False detections and measurement noise are potentials reasons for the detections away from the truth. Since the data is simulated, the only source of measurement noise is assumed to be the inaccuracies caused by range and azimuth resolution. For example, if the range resolution is 10 meters, the range accuracy of a detection cannot be better than 10 meters. Therefore, the deviation of measurements from the truth data is caused by fluctuations in RCS and resolution limitation. Despite those limitations, the tracks closely follow the detections. Note that the performance of the tracker is a function of detections and not necessarily the truth. In case of a real radar, calibration procedures aim to correct measurement noise but the limitation due to resolution as described above still remains. In RMMSE based tracker result (Figure 5.6), there is loss of detection (lower track left side), but the tracker continues prediction for few scans without significant degradation. The track updates when next measurement falls inside the gate (of predicted position).

5.4   Ground Measurement and Results

A ground measurement test was conducted to demonstrate and evaluate the feasibility of real time tracking using PARADOX1 radar. As aforementioned, tracking was done in Track While Scan (TWS) mode. For this ground test, the radar was placed on the roof of a two story building while a small twin engine aircraft was flown in a predetermined path. A sketch of flight trajectory and radar location in addition to a picture of PARADOX1 setup is depicted in Figure 5.7. The required elevation angle of the radar was designed to be sufficiently high to eliminate ground clutter returns which more closely mimics

air-to-air tracking scene. In this particular test, the elevation of the radar was kept constant and the plane was allowed to fly in and out of the beam coverage in elevation. Note that for an airborne collision avoidance operation, elevation angle of the radar platform may be changed between scans. Collision threats that are flying in a constant altitude would then be in and out of the beam coverage in elevation similar to the current ground test setup. However, the most compelling scenario occurs when the collision threat is located in the same horizontal plane (thus at the zero elevation) of the radar platform. For such case, measurement data points will increase due to better scan coverage which results in improved tracking performance when compared to current setup of ground measurement. In this setup the speed of airplane is maintained around 55 m/s (with some fluctuations causing from the wind, pilot control/maneuvering, etc.) and the radar scan update time is about 2.5 seconds.

The module used for SAA tracking consisted of a small form factor PC with Intel$^©$ Core^{TM} i7 processor and 16 GB of DDR3 Random Access Memory (RAM). The module operated a generic GNU/Linux Operating System. Data from the radar sensor was fed into the module using gigabit speed Ethernet port which was read and processed by MATLAB$^®$ using various C functions. The output to a connected monitor was the PPI plot of the current scan and tracks resulting from previous scans. With this test configuration, the hardware was adequate to perform SAA tracking between each scan update time of about 2.5s. Figure 5.8 shows the module for SAA/DAA tracking.

Figure 5.9 shows a sample tracking result for the current ground tracking test. The figure clearly depicts a confirmed track around the measurement points. The measurements are scattered around the ground truth (as opposed to be coincident). This is most likely due to the measurement error. The
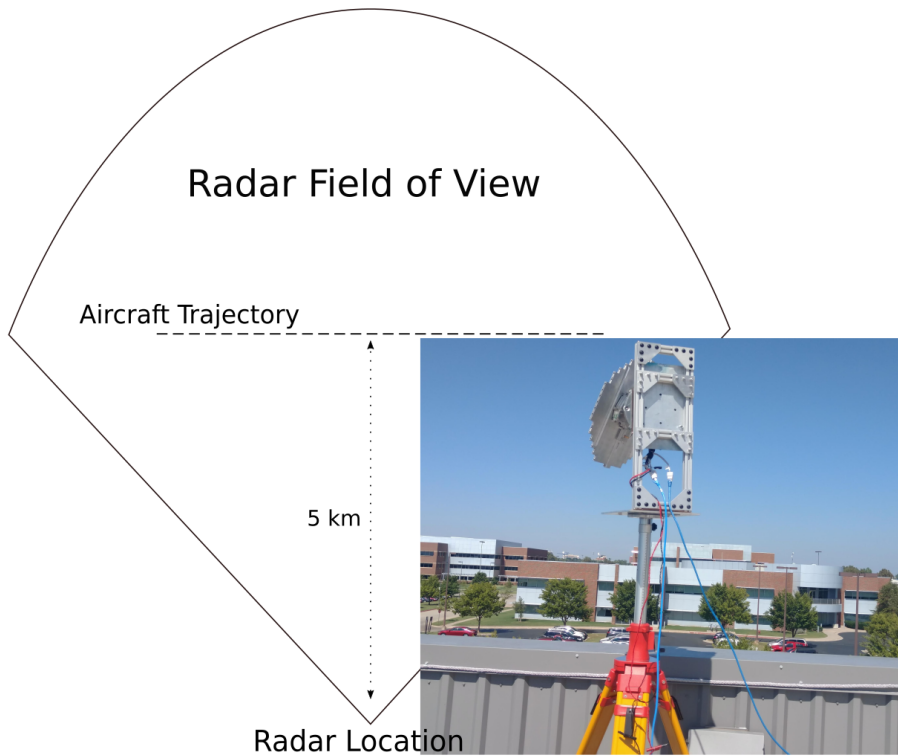
Figure 5.7: Real Time Ground Tracking Flight Trajectory
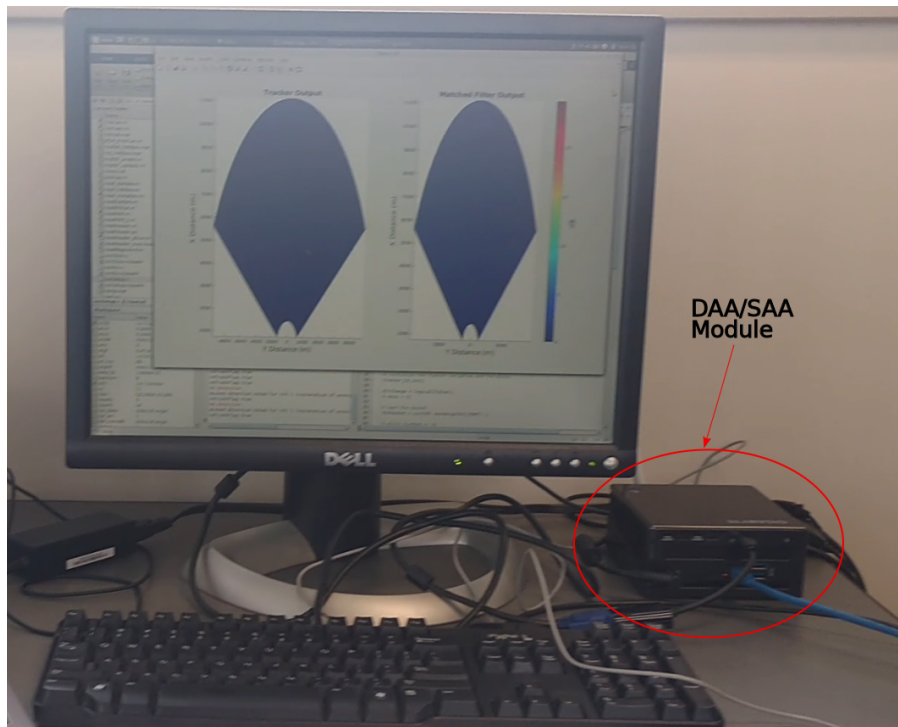
Figure 5.8: Real Time Ground Tracking Module
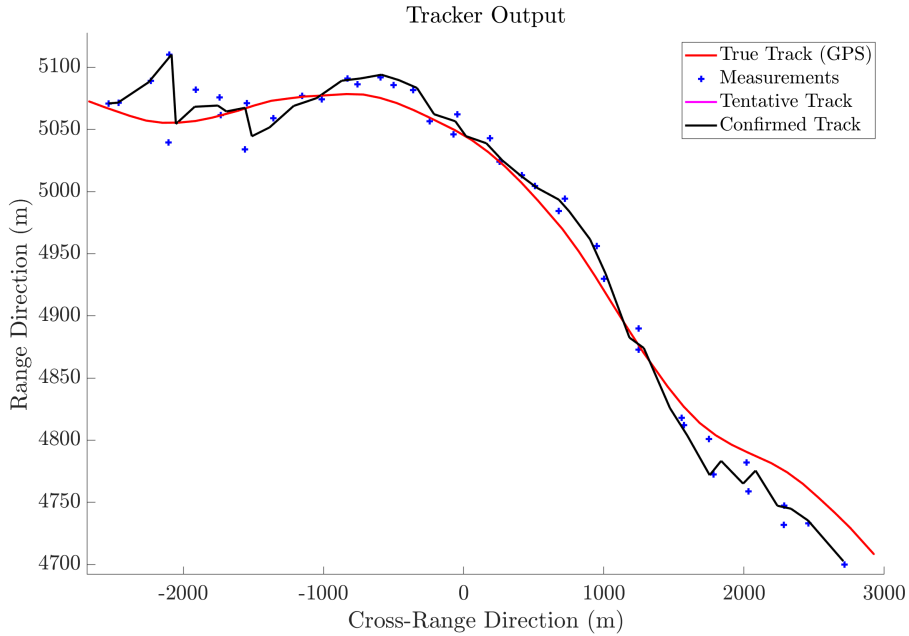
Figure 5.9: Real Time Ground Tracking Results

Matched Filter output is used to generate a "cluster" of detections and the center of the cluster is regarded as the measurement. The range as well as azimuthal sidelobes can alter the detection and cause errors in measurement. Furthermore, since, the signals are "quantized" in range and angle, the inherent resolution limitation likely causes additional errors. The current setup of PARADOX1 has a 18 inch antenna with a beamwidth of 5.6° in both elevation and azimuth; whereas the range resolution is 16 meters. The plane employs a Differential GPS system which is much more accurate than the one used by the ground based radar. Therefore, the GPS truth is considered accurate. The update time also plays an important role in the bias of measurements. A faster update time generally means less target movement between scans and consequently less bias.

The performance of Kalman Filter and JPDA based tracker appears to be adequate in this case. The tracker was able to track the measurements

104

Statistic	Range Dir. (m)	Azimuth Dir. (°)
Maximum Square Error	43.6	2.07
Minimum Square Error	0.53	0
Mean Square Error	16.46	0.76
Std Deviation of Square Error	19.87	0.95

Table 5.1: Error Statistics for PARADOX1 during Ground Based SAA Tracking

and maintain the track in real time for the duration of target visibility. An error analysis is performed between measured values and truth values which is presented in Table 5.1. Although the error in azimuth direction is expected to be high as it is significantly affected by the azimuthal beam spread, in reality, the values are lower because of the detection procedure (center of mass of centroid is assumed to be the measured position). The Mean-Square-Error (MSE) in range dimension is about one range resolution distance which is acceptable. The maximum error in range is about 43 meters which could be due to the misalignment of radar scan update rate and plane GPS update rate. In the future, timestamps for each pulse can be collected to decrease this error.

5.5 Summary and Conclusions

The sense and avoid tracking functionality of PARADOX1 was developed, tested, and validated. First, a two targets scan scenario was simulated using parameters that matched closely to that of PARADOX1. Tracking was performed with and without super-resolution processing and the results were discussed. Furthermore, a real-time tracking experiment was performed through a single target flight scenario. In both (simulated and measurement cases), state estimation and update were carried out using Kalman Filter and the data associations were performed using Joint Probabilistic Data Association algorithm. Both of those algorithms were discussed in detail in Chapter 2.

For the simulated two-target case, the targets were placed at close proximity so that Matched Filter would not be able to resolve them. Azimuthal super-resolution was performed using RMMSE algorithm which was able to differentiate the two targets. Tracking was performed in each of the cases (Matched Filter and RMMSE). Since the targets were not resolved in the Matched FIlter case, the results showed a single track in between the two true tracks. In RMMSE case, the targets were resolved and therefore two separate tracks were formed and maintained. Therefore, RMMSE-based super-resolution and KF/JPDA-based tracking is successfully validated.

In the single target, real-time tracking scenario, the radar was placed on a rooftop while the plane flew over, getting in an out of the radar beam coverage. An x86 based PC was used as a SAA processor and the generated track as well as true track (as measured by Differential GPS) were plotted. The results validated the basic real-time SAA functionality of PARADOX1 radar. The error statistics show maximum MSE in range to be 43.6 meters (less than 3 range bins). The maximum MSE in azimuth was about 2° which is much less than the azimuth resolution.

Chapter 6

Weather Surveillance

As a continued development of multi-mission capability of PARADOX1, this chapter aims to scrutinize the weather measurements from PARADOX1. As aforementioned, airborne radars are already being used for weather hazard monitoring and providing situational awareness to the pilots. However, for scientific as well as research purposes, more specialized and high cost Active Electronically Scanned Array (AESA) radars have been historically used. The reluctance of using low C-SWaP radars for research and scientific purposes stems from the necessity of high quality data. Since most low C-SWaP radars are not built for the purpose of gathering scientific data, often the quality of electronics tend to be subpar. Fortunately, in modern times, the quality and reliability of components have increased with a simultaneous decrease in cost. PARADOX1 (introduced in 2.1) is used as an example of a multi-mission airborne radar which can measure weather from airborne platforms with research grade data. Various weather surveillance algorithms introduced in Chapter 3 are implemented and validated in this chapter.

A thorough assessment of meteorological data quality (obtained from PARA-DOX1) is complicated primarily due to the unavailability of airborne meteo-rological truth data. Indeed, airborne flight campaigns are expensive. Such

campaigns, if at all conducted, are usually done at specific geographical regions for a specific time to measure a specific meteorological event. The only reliable, time-continuous, and geography-contiguous source of validation data comes from NEXRAD [6]–[8]. Therefore, as a method of assessment of data quality (of PARADOX1), NEXRAD data are used which was obtained from [9].

NEXRAD (**Nex**t Generation **Rad**ar) is a network of 159 S-band ground-based pulsed Doppler radar in the US operated by National Weather Service. They are also known as WSR-88D (Weather Survelliance Radar 1988 Doppler). It is to be noted that NEXRAD operates at a different frequency and has a "bottom-up" view of weather events which is in contrast to PARADOX1. PARADOX1 operates at X band, and has a "top-down" view of the weather event. Additionally, due to the difference in aspect angle, direct comparison of radial velocities are not possible to make. In spite of these limitations, and in lieu of proper airborne validation data, NEXRAD data is still the best choice for this comparison due to the wide coverage and availability of data.

In addition to NEXRAD, PX-1000 (Polarimetric X-band 1000) [107], [108] radar operated by Advanced Radar Research Center (ARRC) is also used for comparison and validation of weather measurements. PX-1000 is an X-band polarimetric weather radar with transmit power of 200 Watts in each polarization. It has a receiver bandwidth of 5 MHz and the antenna's azimuth and elevation beamwidth is 1.8°.

For scientific studies, PARADOX1 radar supports two operational modes: micro-physics validation and severe weather observation. Figure 6.1 depicts the concepts of these two operational modes. For the micro-physics (MP) validation mode, the radar probes short range within or near clouds (range from ∼100 m to 20 km). Once the aircraft passes through some distance, the

Microphysics Validation Mode

Comparing received radar data
with probe data collected onboard

Short-range (< 10 km) FWD-looking,
slow scanning/no scanning

Severe Weather Observation Mode

Medium-short range,
downward
Looking of storm tops

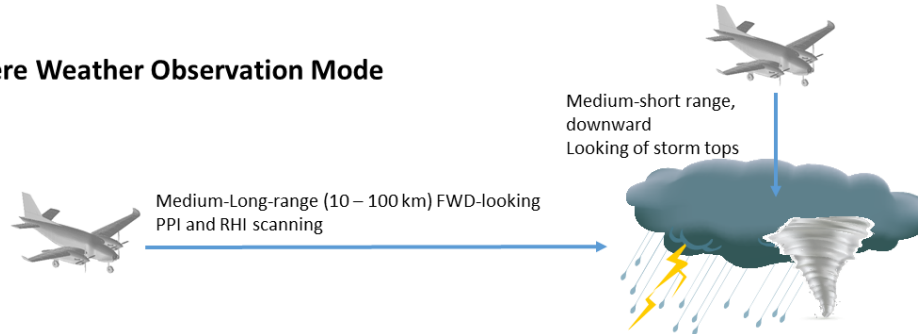Medium-Long-range (10 – 100 km) FWD-looking
PPI and RHI scanning

Figure 6.1: Operation modes of PARADOX1: Micro-Physics Validation (with Polarimetric measurements) (Top), Airborne Severe Weather Observation (Bottom)

received radar data can be compared with the on-board micro-physics/particle probes for cross-validations. The MP validation mode focuses on a narrow forward-looking sector always in front of the aircraft heading direction. Slow scan and relatively fast dwell are used to ensure that the aircraft motion can be compensated for the radar returns from range cells. High range and angular resolutions are needed. Also for this mode, short pulse waveforms need to be used to achieve the shortest possible blind range or adaptive pulse compression need to be used for the mitigation [58], [89], [90].

For the severe weather observation mode, PARADOX1 can measure the weather (e.g. storm or precipitation) using either forward-looking or downward-looking scanning configurations. For the forward-looking scenario, the aircraft is located 10-100 km distance from the convective activities. Plan Position Indicator, PPI, and Range Height Indicator, RHI, scans are used to cover the
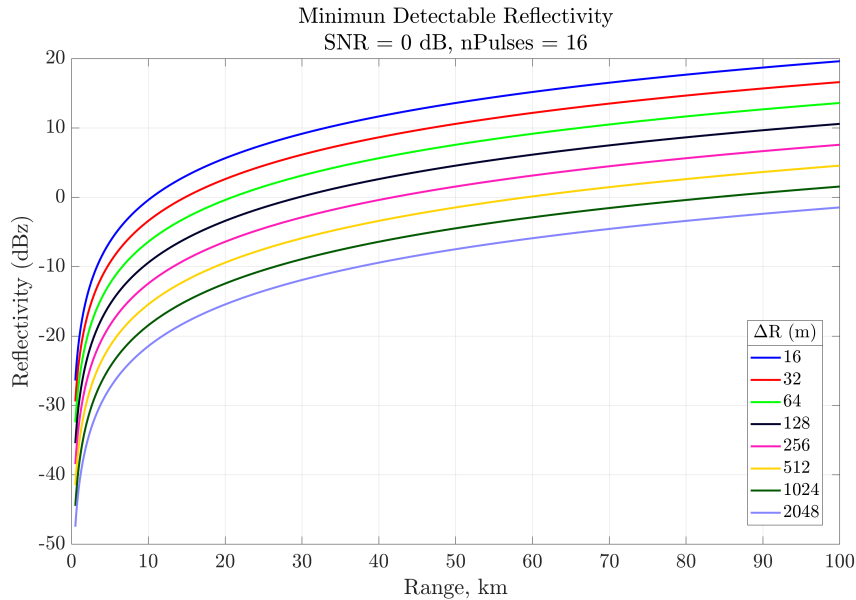
Figure 6.2: Sensitivity Curves (Minimum detectable Reflectivity vs range) of PARADOX1 for Micro-Physics Validation Mode for various range resolutions, ΔR. SNR is constant at 0 dB

larger observation volume. For downward looking from higher altitudes, the observations (so-called "storm-tops") have scientific values for studying stratospheric hydration, ozone observations, and convective activity identifications. Longer pulse (or larger duty cycle) is needed to observe at further distance. Larger scale, "ensemble target" observations are provided for data assimilation and storm dynamics analysis. The resolutions can be enhanced through the processing mentioned in chapters 3 and 4. In addition to micro-physics validation and severe weather observation modes, PARADOX1 has a long-range operation mode that can capture and display weather echoes up to 300 km which is a mode mainly used for early warning of severe weather.

The micro-physics validation mode requires good sensitivity for a shorter range, while the severe weather observation mode requires sufficient sensitivity for storm observations at longer range. It is possible to use similar waveforms
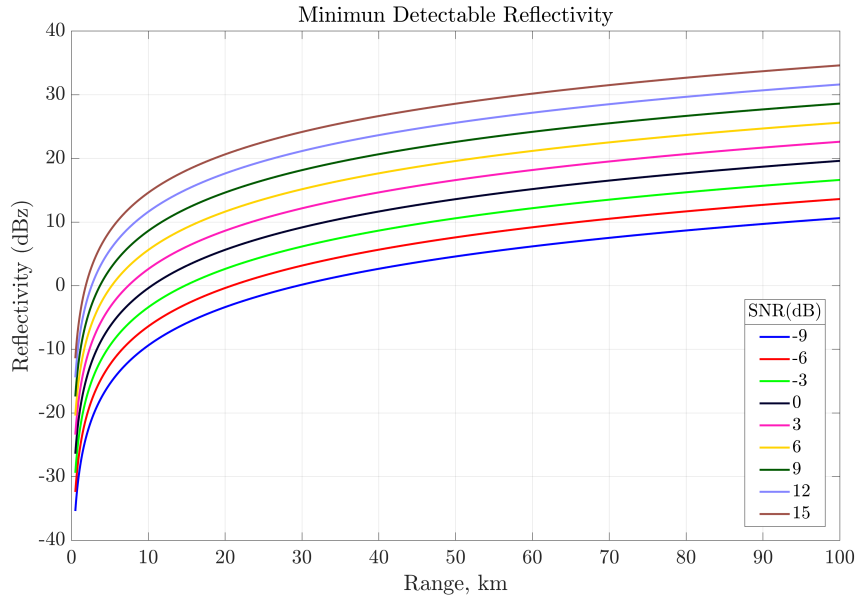
Figure 6.3: Sensitivity Curves (Minimum detectable Reflectivity vs range) of PARADOX1 for Airborne Severe Weather Observation Mode for various SNRs. Range resolution is constant at 16 m

to achieve both requirements. A pulse width of 13.66 μs is used as an example waveform configuration with 9.375 MHz LFM modulation bandwidth (16 m range resolution). Based on system parameters in Table 2.1 and assuming a 16-pulse integration, the sensitivity/link budget curves for short range, and medium–long range operations are shown in Figures 6.2 and 6.3 respectively. The expected system sensitivity is suitable for both modes of operations. Please note that there are a lot of variations in waveform and other radar parameters that can be applied. Figures 6.2 and 6.3 depict the sensitivity for a few of such parameters' combinations.

6.1 Resolution Enhancement using RMMSE Algorithm

As briefly discussed in Chapter 3 with more details as well as derivations in Chapter 4 and an example in Chapter 5, adaptive pulse compression algorithms

were shown to enhance the resolution in range, azimuth, and Doppler domains. For an airborne platform such as PARADOX1, the aperture size is generally small (due to restrictions in C-SWaP as mentioned in Chapter 2). Therefore, it is necessary to have signal processing algorithms that are able to resolve and discriminate various types of targets. The super-resolution results using IAA and MF-IAA for point targets (buildings etc.) were discussed in chapter 4. In this section, two dimensional sidelobe mitigation and resolution enhancement algorithm as described in [90], is validated for weather targets. Furthermore, the results are compared with PX-1000 and the similarities as well as the differences are discussed.

In addition to the hard-target detection scenario (presented in Chapter 5), RMMSE Super-Resolution algorithm can also be used in distributed target scenarios like weather events. Figures 6.4a, 6.4b, 6.5a, and 6.5b show an example of application of RMMSE-based super-resolution algorithm regarding weather targets. These are uncalibrated power level data from the PPI scans of PARADOX1 and PX-1000 radar. The data was collected during a field campaign in Fall 2016. Figures 6.4a, 6.4b, and 6.5a respectively show the matched filter output, RMMSE-SR output and range downsampled RMMSE-SR output for the PARADOX1 radar. The range was downsampled to achieve a better comparison with PX-1000 PPI scan which is depicted in figure 6.5b. The two radars were located about 10 meters apart and they scanned over the same light to moderate rainfall area. Note that due to beam blockage, PX-1000 output missed some data around the 0° azimuth. In the same region, PARADOX1 shows lower SNR values. A proper data quality assessment as well as removal of such "unreliable" data will be presented in the following sections.
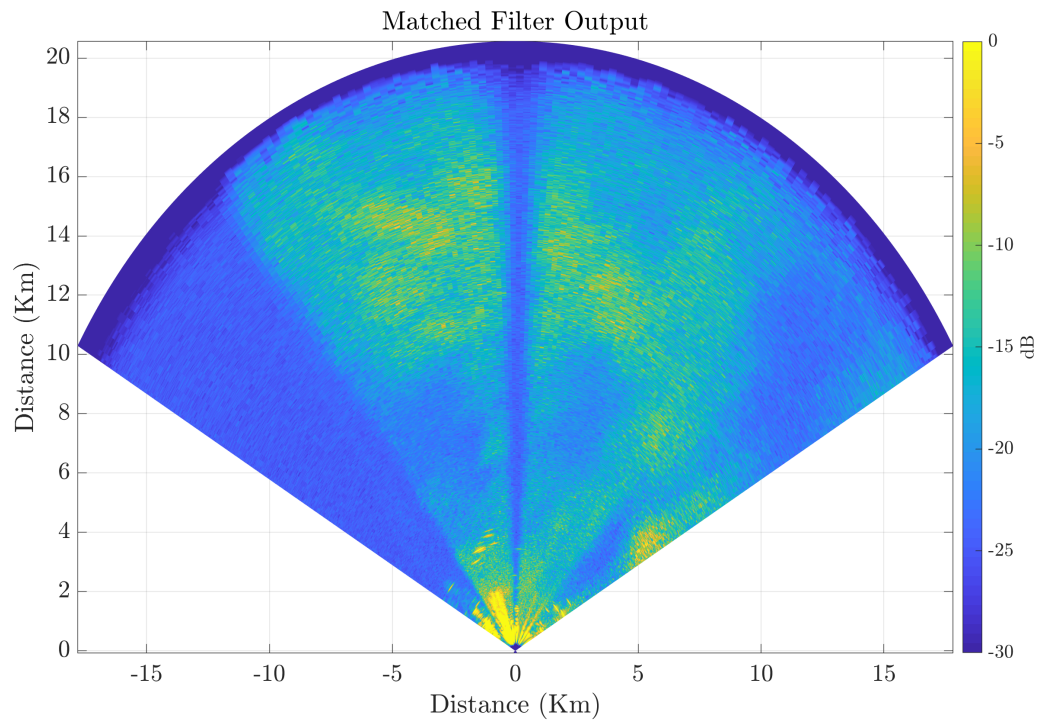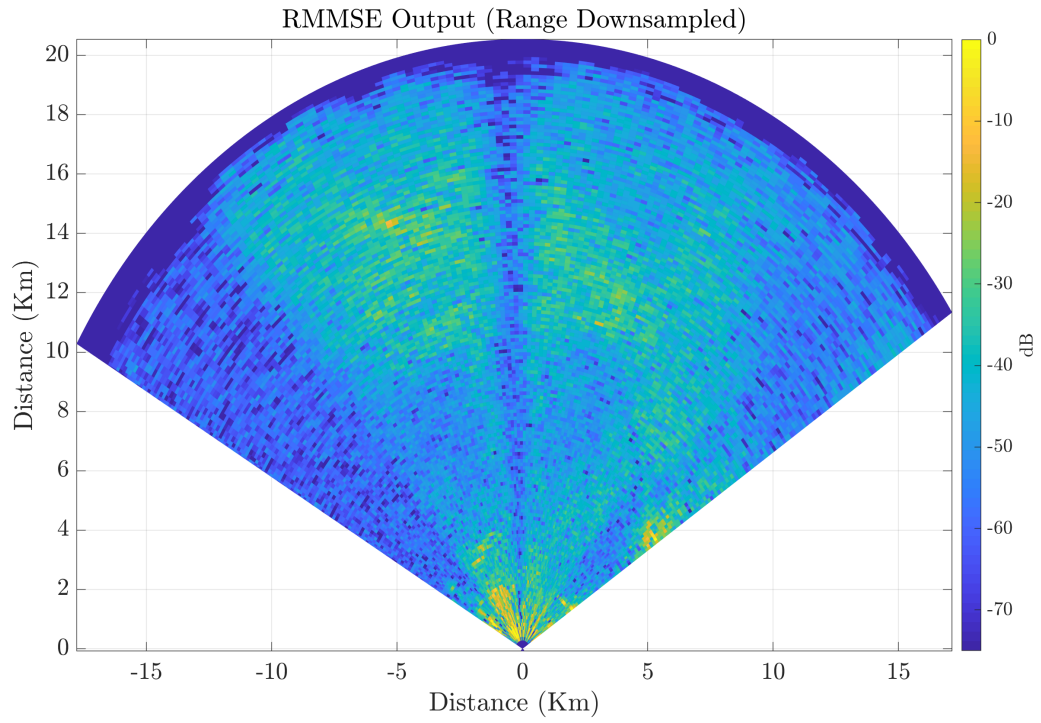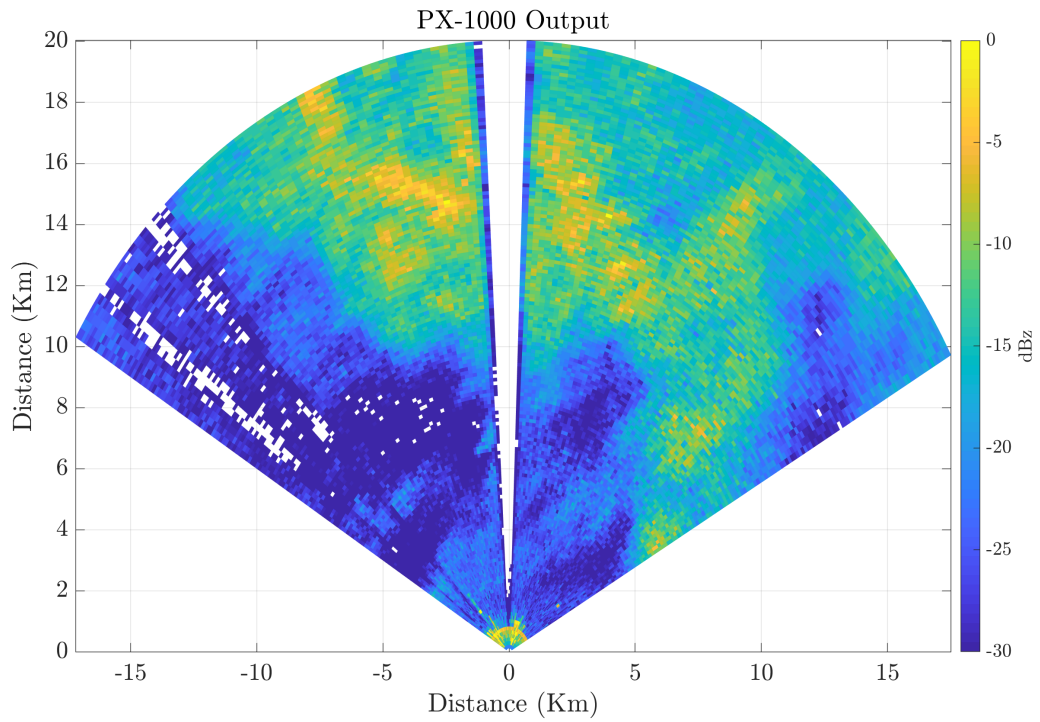
(a) Matched Filter Output PPI
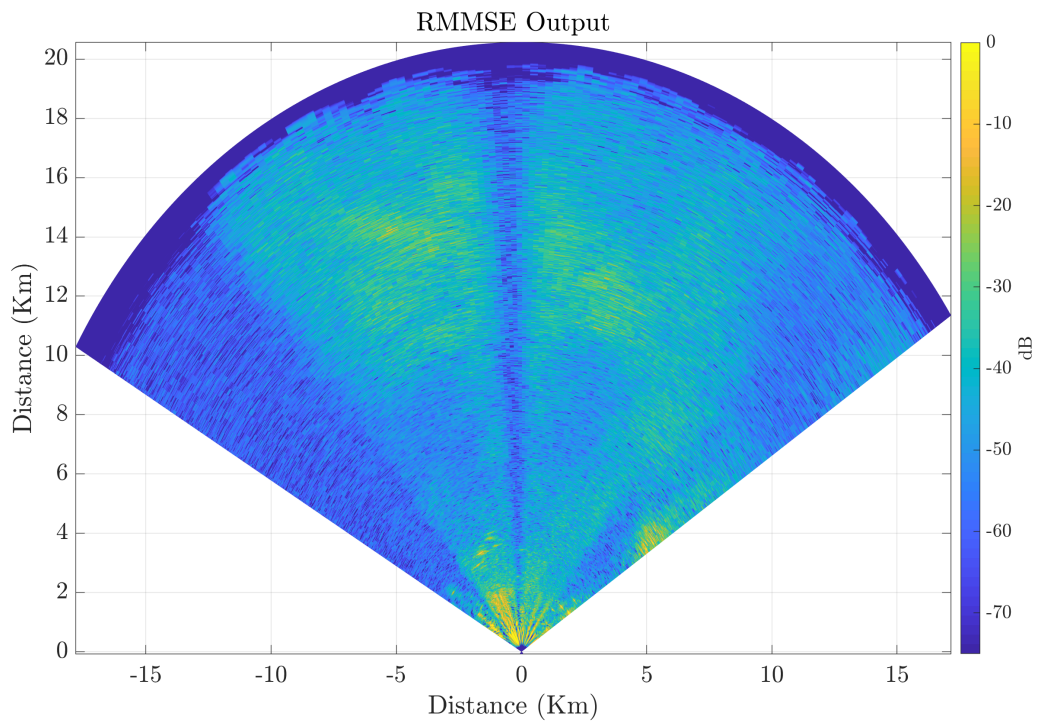
(b) RMMSE Super-Resolution Algorithm Output PPI

Figure 6.4: Matched Filter and SR output for distributed weather target for PARADOX1

(a) Range Downsampled RMMSE results PPI from PARADOX1

(b) Reflectivity PPI from PX-1000

Figure 6.5: Downsampled Super-resolution output from PARADOX1 compared with PX-1000 outputs for distributed weather target

As is the case with most weather events, an accurate ground truth is often difficult to obtain. However, at first glance, and while looking at just the uncalibrated power returns, it can be reasonably asserted that RMMSE-SR produces better azimuthal resolution. In addition to increasing the dynamic range, the RMMSE-SR results show less smearing around more prominent weather regions, e.g. around 14 km range and -12° azimuth, 12 km range and 8° azimuth, and 3 km range and 60° azimuth. When PARADOX1 data is compared against PX-1000 data, although there is a difference in sensitivity, the overall picture of the weather appears to be similar. The high Reflectivity areas as well as the transition of higher Reflectivity to lower Reflectivity in the scan have a general agreement. A complete data quality analysis will be performed in the following sections which will enable us to properly examine the validity and feasibility of PARADOX1 as a research-grade weather measurement capable radar. For the time being, it can be concluded that RMMSE-SR can be used to enhance the azimuthal resolution in cases of both point targets (as shown in Chapter 5) as well as distributed weather targets.

6.2   PARADOX1: Airborne Flight Campaign of 2017

Airborne flight test campaigns have been routinely performed since 2015 for validation of the system performance and data quality of the PARADOX radars. A recent flight campaign was performed in spring of 2017 where the airborne PARADOX1 radar measured weather returns in a forward-looking scenario in a region around Southern Oklahoma. The radar location, weather event location as well as radar field of view is depicted in Figure 6.6. Please note that the map is rotated so that the heading direction points towards the positive Y-axis. The radar parameters configurations and the aircraft supplemental
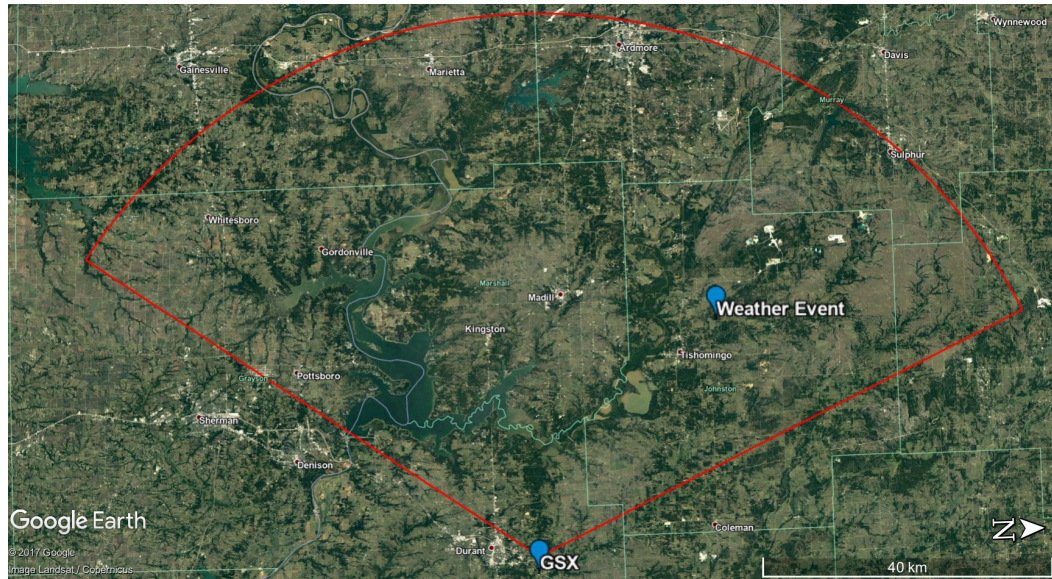
Figure 6.6: Airborne Campaign 2017: Scan extent of PARADOX1 in Google Earth®

information are listed in Table 6.1.

As listed in Table 6.1, the radar was at 10 km altitude scanning downward (at -1° elevation). In the airborne configuration, the earth surface was more than 550 km away in slant range. Examining the two different PRF's, the maximum unambiguous ranges were calculated to be about 149.89 km (for 1000 Hz PRF) and 99.93 km (for 1500 Hz PRF). Although the maximum unambiguous ranges (associated with both of the PRF's) could potentially cause multi-trip echoes in high power radars, PARADOX1 is a low C-SWaP radar. Furthermore, the earth surface was at a sufficiently large distance. Therefore, multi-trip echo was not considered in this case. As discussed in Chapter 3, the three most important spectral moment were estimated. This was followed by the application of basic motion compensation algorithm to obtain the "true" Doppler measurement of weather targets. Next, basic noise reduction, and removal were performed. Finally, staggered dual PRF CPI's

Radar Parameter	Value
Radar Frequency	9.376 GHz
Waveform Type	Linear Frequency Modulated
Pulse width	82.4μs
Waveform Bandwidth	686 KHz
Pulse Repetition Frequency (PRF)	1000 Hz and 1500 Hz
Radar Altitude	10057 m
Scan Elevation	-1°
Scan Azimuth	-60° to +60° from Heading Direction
Aircraft Latitude and Longitude	34.05° N and 96.38° W
Aircraft Heading	-84.6°
Aircraft Ground Speed	119.5 m/s

Table 6.1: PARADOX1 Parameters used in Airborne Measurement Campaign of 2017

were employed to increase the maximum unambiguous velocity extents. Please note that the clutter is (generally) not strong for a forward-looking air-to-air scenario, and therefore additional spectrum compensation as well as clutter mitigation strategies were not performed in this case.

From the raw signal power plot at Figure 6.7a, a significant weather phenomenon can be seen at about 45 km (40 km heading and 20 km cross-heading) from the radar. The Matched Filter output from PARADOX1 was passed through a threshold detector that removed fluctuating values around noise floor; the threshold was set at 20 dB. The output after thresholding is depicted in Figure 6.7b. For the airborne case, there were no near-range clutter as in the ground data collection case, and overall, the scene didn't have many scatterers either. Therefore, the 20 dB threshold setting was able to provide an adequate distinction between the weather phenomenon and its surroundings. The spatial resolution appeared to be satisfactory for this severe weather observation case; so no further resolution enhancement processing was applied.

The first spectral moment or the Radial Velocity PPI is shown in Figure
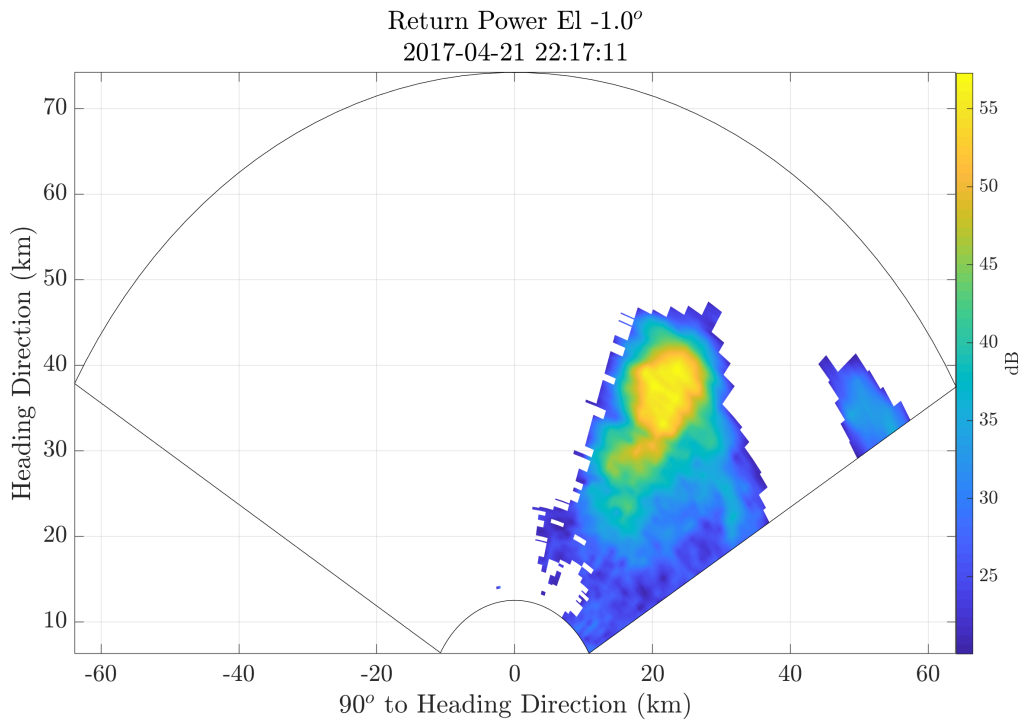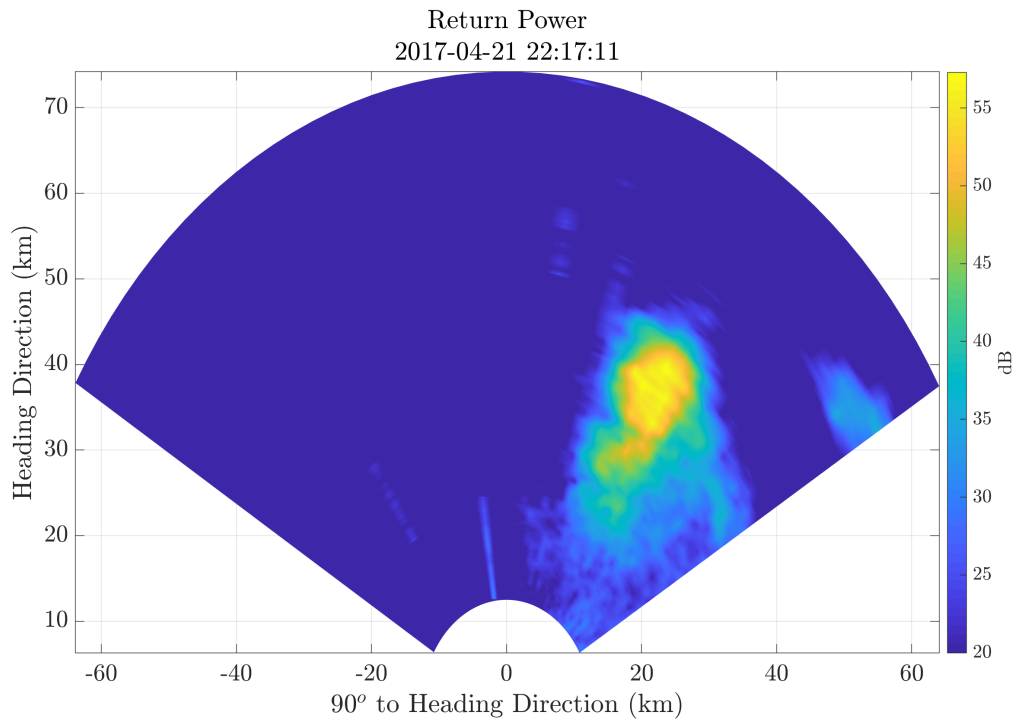
(a) Raw Return Power

(b) Raw Return Power after noise control processing

Figure 6.7: Airborne Case: Return Power Plots

(a) Radial Velocity Plot
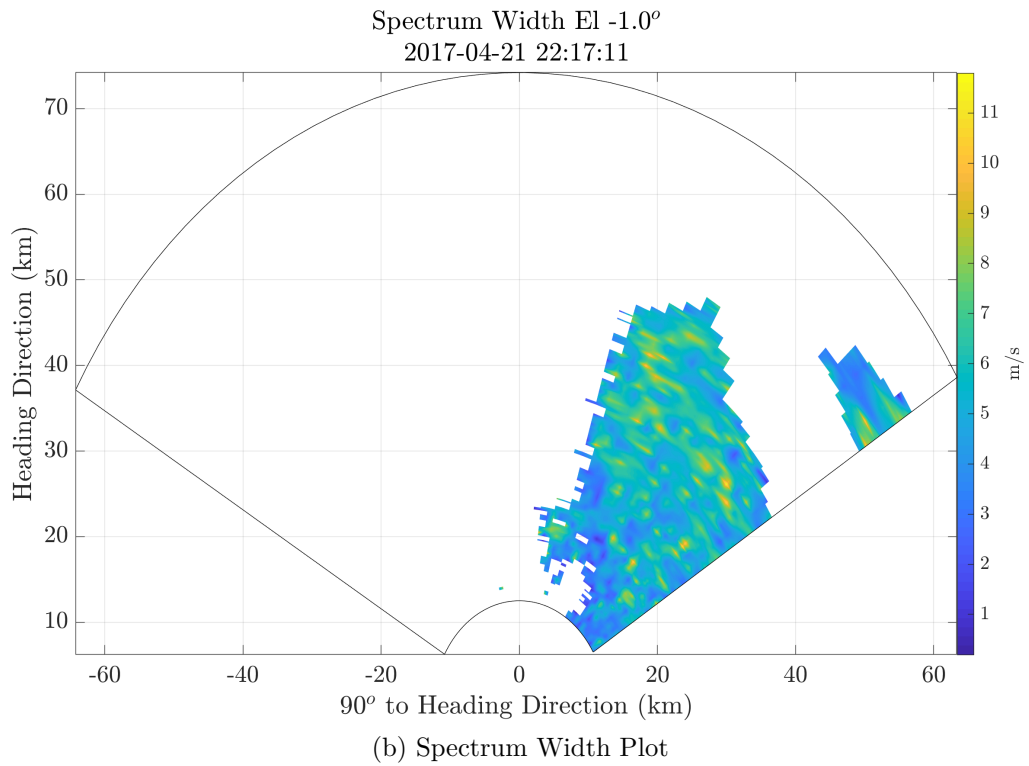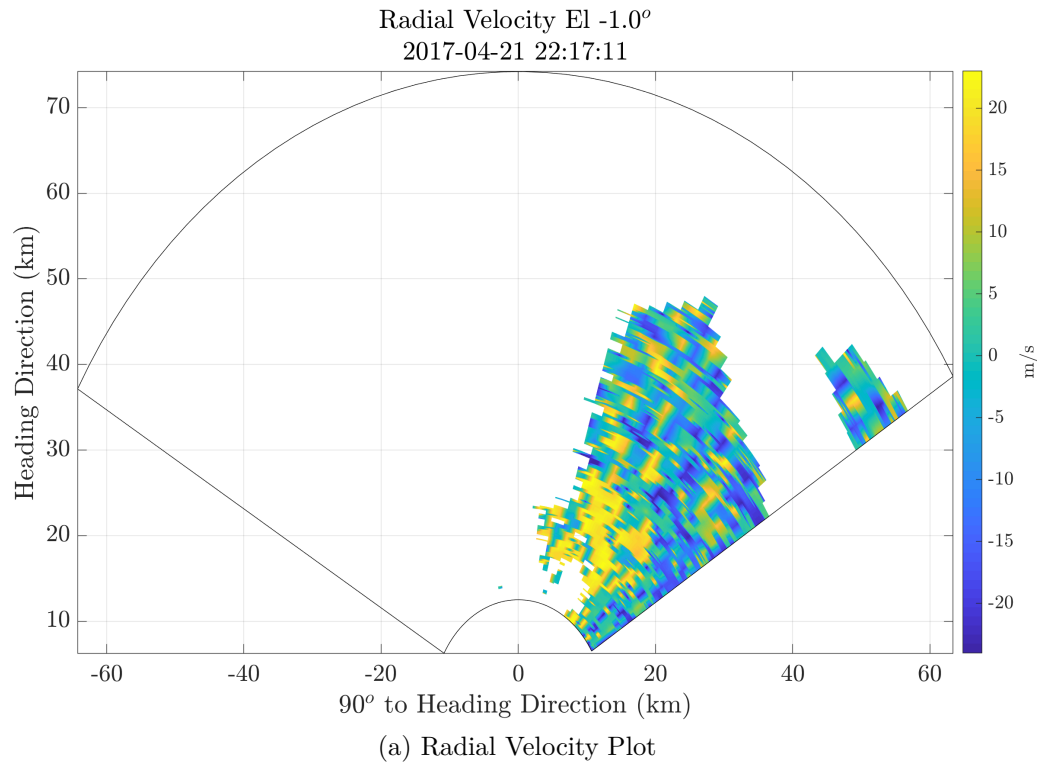

(b) Spectrum Width Plot

Figure 6.8: Airborne Case: Radial Velocity and Spectrum Width Plots

Algorithm 1 Velocity ambiguity resolution using two PRF's
___
 1: For each CPI estimate the Radial Velocity.
 2: Calculate one-time alias of Radial Velocity estimate in each case.
 3: Compare all the estimated Radial Velocities.
 4: The matching Radial Velocity value from the two CPI's is the newly estimated non-aliased Radial Velocity.
___

6.8a whereas the square root of the second spectral moment or Spectrum Width is shown in Figure 6.8b. As a result of quality control (QC) processing, there is a significant number of empty values in the display plot due to the lack of hydrometeor scatterers or any other targets in the field of view (of the radar). The returned signals from those range-azimuth bins (the ones without a target) have very low Signal to Noise Ratio (SNR). In addition, the lack of targets result in a uniform random distribution of (pulse to pulse) phase changes. The random phase changes then result in random Radial Velocity estimates and also results in higher values of Spectrum Width. Hence, if a range-azimuth cell met the condition of having low SNR and at the same time very high Spectrum Width value, the data at that particular range-azimuth cell was considered to not have met the data quality threshold. Such data points were removed from the final PPI plots.

There were two available Coherent Pulse Intervals (CPI's) during the campaign, with PRF's of 1000 Hz and 1500 Hz. Separately, the maximum unambiguous velocities were 7.99 m/s (for CPI with PRF 1500 Hz) and 11.99 m/s (for CPI with 1000 Hz) at the transmit frequency of 9.376 GHz. However, there are techniques to increase the maximum unambiguous velocity using multiple CPI's with different PRF's. One of the techniques as described in [98] was used to increase unambiguous velocity to 23.98 m/s. Such increase of maximum unambiguous velocity range is dependent on the ratio of PRFs. A discussion is presented in subsection 3.3.4 of Chapter 3. This current algorithm

of ambiguity resolution is presented in Algorithm 1. This algorithm results in unambiguous velocity estimates to be between -23.98 to +23.98 m/s. However, if the true velocity is outside this (new) unambiguous velocity extent, aliasing will still occur. As the figure shows, there appears to be a fair amount of velocity aliasing in the plot, since the values jump between +23.98, 0, and -23.98 m/s. Of course, a higher PRF can be used to increase the maximum unambiguous velocity but that will also decrease the maximum unambiguous range. Hence, a different set of staggered PRF's can be employed to achieve higher values of both maximum unambiguous range and maximum unambiguous velocity. The Spectrum Width was calculated using time domain pulse pair processing as explained in [3]. As aforementioned, low SNR causes higher and unreliable estimate of Spectrum Width. Therefore, any data that caused the Spectrum Width to exceed the value of 24 m/s or equal to 0 m/s was considered unreliable. Hence, those data points were removed from consideration in both of the moment plots in Figure 6.8 as well as Figure 6.7b.

6.2.1 Comparison with NEXRAD/KTLX (PPI Plots)

A basic comparison is performed between the data obtained and processed from PARADOX1 and a NEXRAD radar. KTLX radar at Oklahoma City, OK was chosen for the comparison because of its proximity to the weather event. The procedure for choosing NEXRAD radar is presented in Algorithm 2. Please note that the scan time and elevation angles between PARADOX1 and NEXRAD radars rarely match and a closest match is used for comparisons. The implicit assumption here is that the weather event is big enough and the beamwidth (of each radar) is wide enough so that a comparison can be made for the specific weather location. An additional assumption is that the weather event evolves

Algorithm 2 Algorithm to chose proper NEXRAD data for comparisons

1: Calculate the location (Latitude, Longitude, and Altitude) of the weather event.
2: Find the closest NEXRAD radar (among 159 NEXRAD radars).
3: Download the NEXRAD dataset with closest match in time (with PARADOX1 dataset).
4: Calculate the required elevation from NEXRAD's point of view and collect the data with closest match in elevation.

slowly enough that the time difference between the scans by PARADOX1 and NEXRAD doesn't have a significant impact on the measurements.

As in the case of PARADOX1, KTLX data also shows a significant number of empty values on the plot. The reason for that is the strict data quality procedures employed by NEXRAD processors. NEXRAD I/Q data is fed into algorithms that perform Interference Filtering, Ground Clutter Filtering, Spectral Noise Level Estimation and a series of other algorithms to censor imprecise range-azimuth-elevation cell data. Figure 6.9a shows the Reflectivity plot from KTLX with the field of view of PARADOX1 traced towards the bottom. Figures 6.9b, 6.10a, and 6.10b show the Reflectivity, Radial Velocity, and Spectrum Width plots respectively from KTLX with the similar field-of-view of PARADOX1.

There is a fair agreement between the Reflectivity plot of PARADOX1 and KTLX. As aforementioned, an accurate Reflectivity-to-Reflectivity (dBz to dBz) comparison cannot be performed because there is a slight difference between the beam coverage and the time of scan between the two radars. In addition, the frequency difference between PARADOX and NEXRAD causes backscatter (and forward scatter) amplitudes from hydrometeors to be different. Due to those reasons, the two weather events are not of the same size (in space). Additionally, there appears to be another smaller Reflectivity region around 30
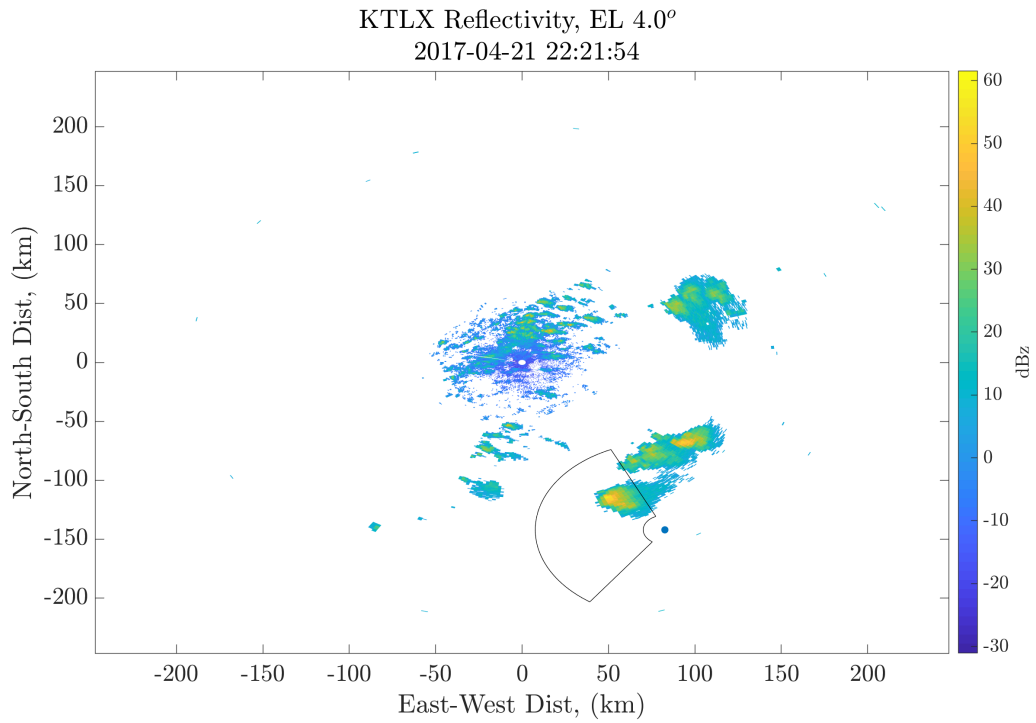
(a) PARADOX1 Field of View in KTLX PPI
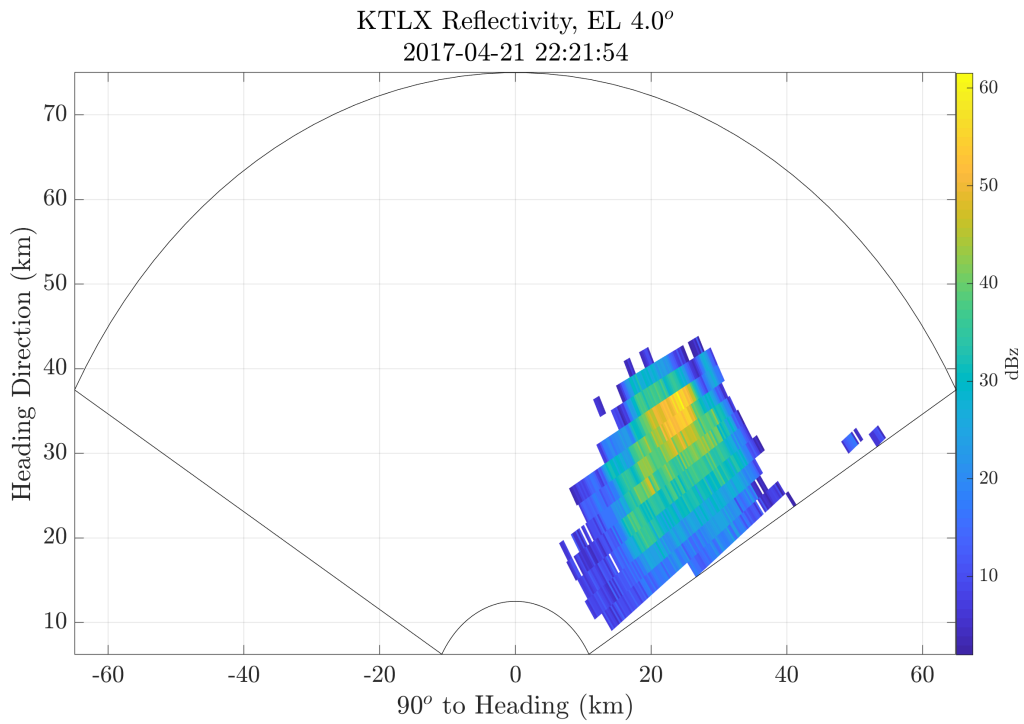
(b) KTLX Reflectivity Plot

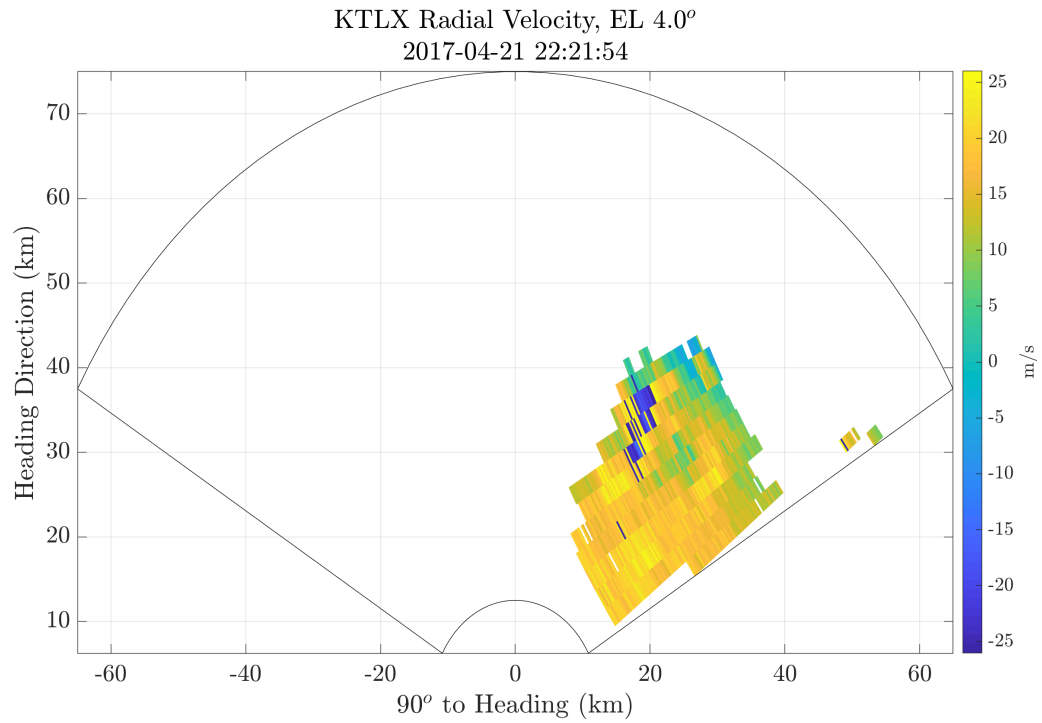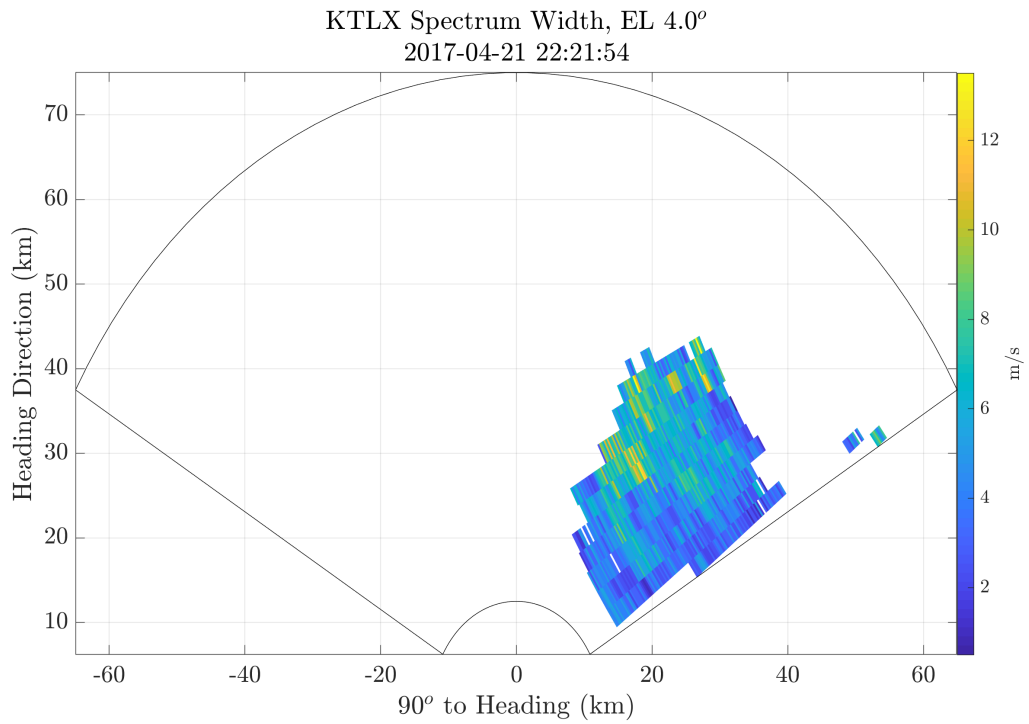Figure 6.9: Airborne Case: NEXRAD/KTLX Reflectivity PPI with same Field of View as PARADOX1

(a) KTLX Radial Velocity Plot

(b) KTLX Spectrum Width Plot

Figure 6.10: Airborne Case: NEXRAD/KTLX Radial Velocity and Spectrum Width PPI with same Field of View as PARADOX1

124

km heading and 50 km cross-heading direction in PARADOX1 PPI which is not so apparent in KTLX PPI.

The Radial Velocity between the two radars most likely will not match because of the different location of the radars. Nevertheless, few conjectures can still be derived. The Radial Velocity plot in KTLX seems to have more uniformity and fewer fluctuations between the positive and negative extremes, and zero. This uniformity can be attributed to the fact that the terminal velocity of rain drops (as they fall towards the earth's surface) is the most significant component on the Radial Velocity plot of KTLX radar. Since the PRF(s) of current NEXRAD is unknown (there are multiple scanning strategies of NEXRAD, and they are not specified in Level 2 data), excessive commenting on Radial Velocity is refrained. PARADOX1, on the other hand, measured from an airborne configuration. The motion compensation was applied so the aircraft's motion effect is largely removed. The velocity that appears in PARADOX1 Radial Velocity plot is the summation of the component of terminal velocity (of rain drops) and their radial motion (relative to radar due to wind). There is also a potential for an additional Doppler phase change due to aircraft motion that was not corrected by motion compensation algorithm. Therefore, it is impossible to definitively claim the validity (or lack thereof) of the Radial Velocity plot generated from PARADOX1.

In case of Spectrum Width, the case is similar to the Reflectivity plot. Since Spectrum Width measures the "spread" of velocity (or turbulence) in the scene, it is reasonable to assume that there will be a general agreement between KTLX data and PARADOX1 data. As it is evident, both radars have maximum Spectrum Width values around 12 m/s and a majority of values between 4 and 8 m/s. Spectrum Width values are highly dependent on the

returned Signal to Noise Ratio (SNR). A ground radar with higher transmit power is expected to have better SNR and therefore more accurate Spectrum Width estimation.

6.2.2 Comparison with NEXRAD/KTLX Constant Altitude PPI (CAPPI) Plots

As aforementioned, the airborne PARADOX1 was at about 10 km altitude and scanned at -1° elevation. Considering near zero scan elevation coupled with a wide beamwidth (around 7°), it is prudent to use Constant Altitude Plan Position Indicator (CAPPI) plots from ground radar for comparisons. In contrast to a more general Plan Position Indicator (PPI) plot, a CAPPI plot maintains a constant altitude throughout the plot. As NEXRAD radars (and by extension KTLX) have a 3D cone of coverage, a single altitude cut can be obtained by extracting proper data values from different elevation scans and filling out the remaining data points using interpolation algorithms. The method of obtaining CAPPI data is similar to Algorithm 2 except all the elevation data from step 3 is used (essentially, last step is skipped). The 3D coverage data can then be processed using Python ARM Radar Toolkit (Py-ART) library [109] to generate CAPPI of the three radar moments after which a comparison with the PARADOX1 plots can be made.

Figures 6.11a, 6.11b, 6.12a, and 6.12b show the "full" KTLX Reflectivity plot for the same scene (depicted in Figure 6.9a), the field of view of PARADOX1 for Reflectivity, Radial Velocity, and Spectrum Width, respectively. One of the first thing that is vivid in all of the the CAPPI plots is their smoothness which is caused by the interpolation of data. As opposed to both KTLX PPI and PARADOX1 PPI which have more fluctuating values, especially in
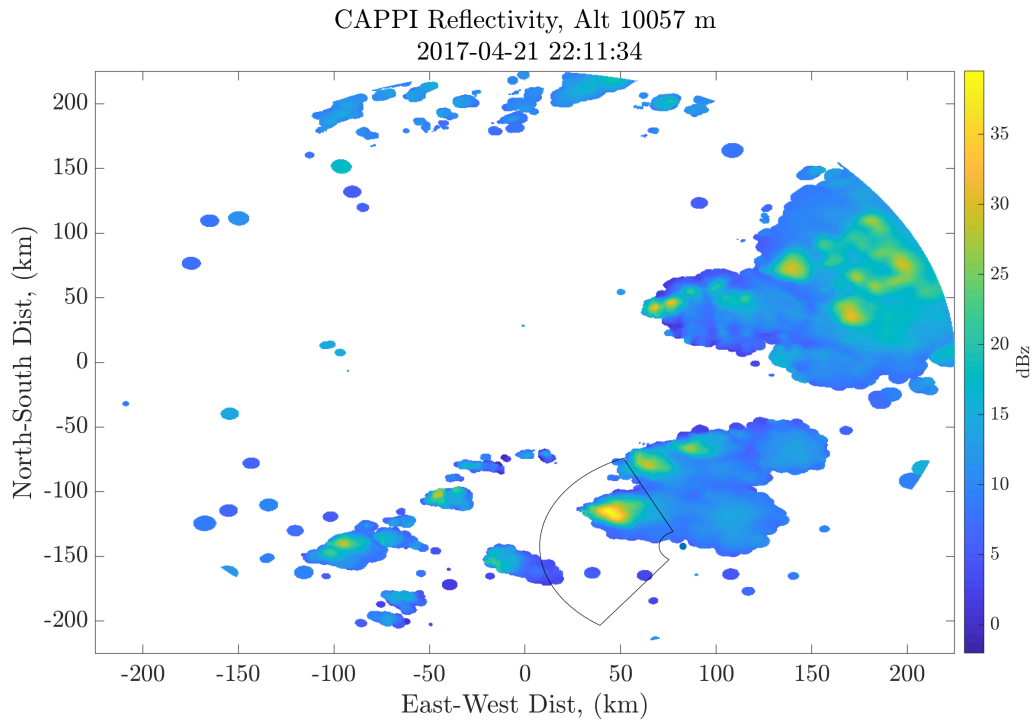
(a) PARADOX1 Field of View in KTLX PPI
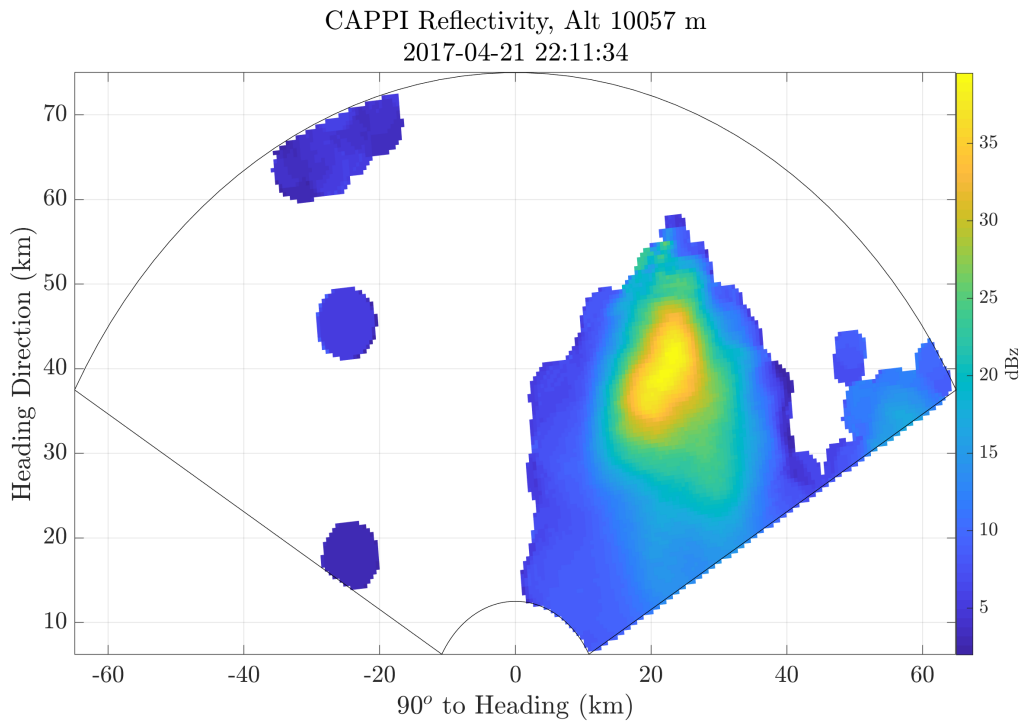
(b) KTLX Reflectivity Plot

Figure 6.11: Airborne Case: NEXRAD/KTLX Reflectivity CAPPI with same Field of View as PARADOX1

(a) KTLX Radial Velocity Plot

(b) KTLX Spectrum Width Plot

Figure 6.12: Airborne Case: NEXRAD/KTLX Radial Velocity and Spectrum Width CAPPI with same Field of View as PARADOX1

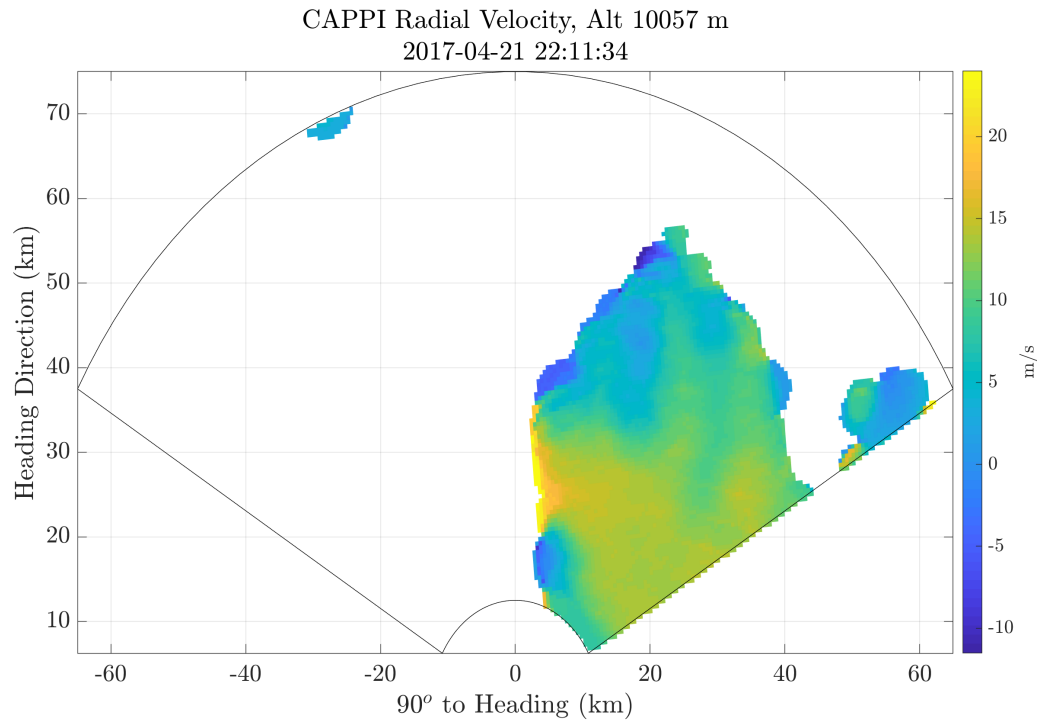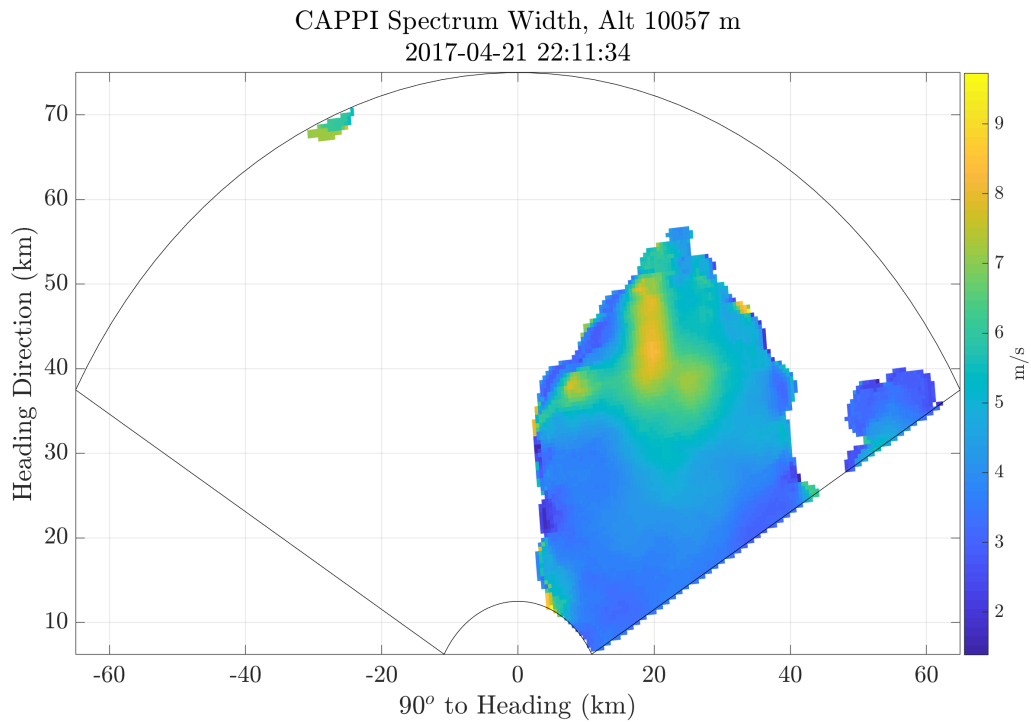Radial Velocity and Spectrum Width, there is a smoother transition from high values to low values in CAPPI plots. Another difference between CAPPI and PARADOX1 (and KTLX) PPI plots is the visibility of range-azimuth cells in the plots. In PARADOX1 and KTLX PPI plots, the shape and size of the range-azimuth cells are visible as individual "pixels". As the range increases, the range-azimuth cells become more oblate leading to a better differentiation of individual range-azimuth cells at a further range. The reason is that in contrast to range resolution which is constant, the spatial resolution in azimuth (and elevation) direction increases with increasing range. In case of CAPPI, the range-azimuth cells are uniform (and square in the current case but not always necessary).

Quantitatively, the CAPPI plots match better with PARADOX1 plots than the original PPI plots from KTLX. Comparing the Reflectivity plot in Figures 6.7b, 6.9b, and 6.11b, the CAPPI plot shows a bigger region of higher Reflectivity than KTLX PPI. PARADOX1 also has a bigger region of high return power. KTLX PPI doesn't show the weaker return from about 30 km in heading direction and 50 km cross-heading direction but both CAPPI plot and PARADOX1 PPI have those returns. The main reason for this distinction is the beam coverage; KTLX PPI beam coverage is slanted with 4° elevation and was chosen so that the data from the more prominent weather region (around 40 km heading and 20 km cross-heading) is captured. Choosing a single elevation KTLX PPI consequently leads to mismatched beam coverage (with PARADOX1) in other areas. CAPPI plot was included in the comparison precisely to alleviate this limitation.

The velocity plots, on the other hand, cannot be compared directly because of difference in aspect angle. In case of Spectrum Width, there is a small region

Figure 6.13: Ground Measurement Campaign 2016: Scan extent of PARADOX1 in Google Earth®

around 40 km heading and 20 km cross-heading, where the Spectrum Width value is high in CAPPI but not in KTLX PPI. The PARADOX1 PPI shows generally higher values in Spectrum Width.

6.3 PARADOX1: Ground Measurement Campaign of 2016

Similar to the airborne measurement campaign, PARADOX1 was also used in a ground-based configuration for a data collection campaign. The measurements were performed in fall of 2016 to observe general precipitations. The purpose of this particular ground test was to achieve more accurate comparison scenario with ground-based radars, in the shorter range. Similar to the previous case where airborne data from PARADOX1 is compared to the NEXRAD returns, this section examines the PARADOX1 data in the ground-based case and

Radar Parameter	Value
Radar Frequency	9.323 GHz
Waveform Type	Linear Frequency Modulated
Pulse width	$13.65\mu s$
Waveform Bandwidth	4.69 MHz
Pulse Repetition Frequency (PRF)	5000 Hz
Scan Elevation	3.4°
Scan Azimuth	-60° to +60° from Heading Direction
Radar Latitude and Longitude	35.24° N and 97.46° W
Radar Heading	161°

Table 6.2: PARADOX1 Parameters used in Ground Measurement Campaign of 2016

comparisons are made. In addition to comparing with NEXRAD, the data is also compared against another ground-based research radar, PX-1000. PX-1000 [107], [108] radar was briefly discussed in Section 6.1. During the measurements, PX-1000 was located about 10 meters south-west from the ground-based configuration of PARADOX1 radar. As done in the previous case, the return power, Radial Velocity and Spectrum Width results are compared and discussed. Figure 6.13 shows the scene of this ground-based measurement. Please note that the PARADOX1 radar was facing south-west and the -60° to +60° coverage is shown in red sector. The basic radar parameter configuration is listed in Table 6.2. In this measurement, the PARADOX1 data suffered from two beam blockages one at 0° (161° from true north, clockwise) caused by NOAA's National Weather Radar Testbed (NWRT) building which is also seen in PX-1000 scans. Another beam blockage for PARADOX1 radar was caused by the PX-1000 radar located at about 40° to the right (about 201° from true north, clockwise).

The signal processing algorithms applied in ground-based PARADOX1 raw I/Q data is similar to the airborne case. The differences are as follows,

1. There is no need for motion compensation as PARADOX1 is stationary.

2. Since the data was collected using a single PRF (5000 Hz), velocity ambiguity mitigation algorithms couldn't be applied. However, because of higher PRF, the maximum unambiguous velocity results to be 40.2 m/s which is well above the light rain maximum velocity. Therefore, there was no need for staggered PRF and subsequent velocity ambiguity correction.

For the moment computation algorithms, the noise floor was chosen at 20 dB. Radial Velocity and Spectrum Width were calculated using time domain autocorrelation method as described in [3]. Because of relatively short range, only range squared and radar constant calibration was used; range attenuation correction algorithm was not applied. The range-azimuth super-resolution enhancement processing was tested on this dataset, and the results were shown in Figures 6.4b, and 6.5a of Section 6.1. Since the range resolution of PARADOX1, in this case, was good (as a matter of fact, better than ground radar scans), range-resampling was applied to reduce the resolution for proper comparison with ground radar data.

Figures 6.14, 6.15a, and 6.15b show the plots of return power (before calibrating into dBz values), Radial Velocity and Spectrum Width respectively in this ground observation case. As in the case of the airborne campaign, there is a fair amount of empty values in all the three plots. As aforementioned, data with low SNR tend to produce high values of Spectrum Width; subsequently, the Quality Control Algorithm considered any range-azimuth cell that has Spectrum Width value higher than 13 m/s as unreliable and therefore removed those data from the display. In addition to the higher SNR values all around the PPI in further range, there appeared a more distinct weather event around
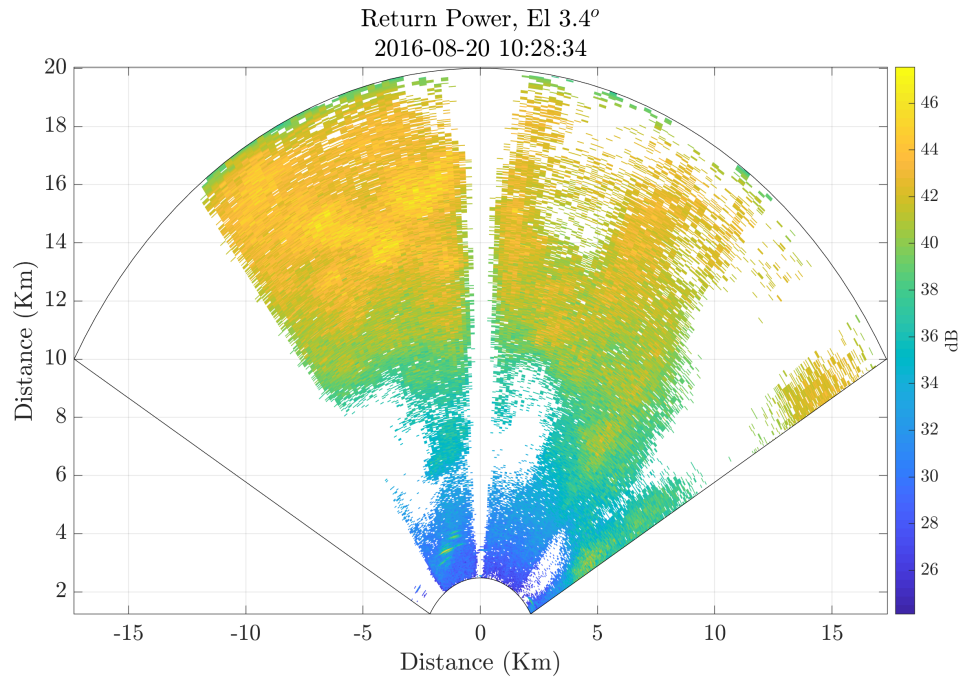
Figure 6.14: Ground Measurement: Uncalibrated but noise processed Return Power PPI

14 km heading and -5 km cross-heading direction. That location was chosen to calculate the required elevation angle from NEXRAD which was used to further examine the returns. The process of data retrieval from NEXRAD is equivalent to the airborne campaign case which was discussed in the previous section with the procedure presented in Algorithm 2.

Closer examination of the Radial Velocity plot shows a clear trend of negative velocity values towards the right side of plot transitioning to zero values towards the center of the plot and then to positive values in the left side of the plot. Therefore, this data indicates the rain was moving from West side towards East side while the radar was facing the South direction. Another explanation might be a presence of updraft and downdraft in the rain region. The Spectrum Width plot shows higher values around the edges of the weather event while showing lower values in the range-azimuth cells that
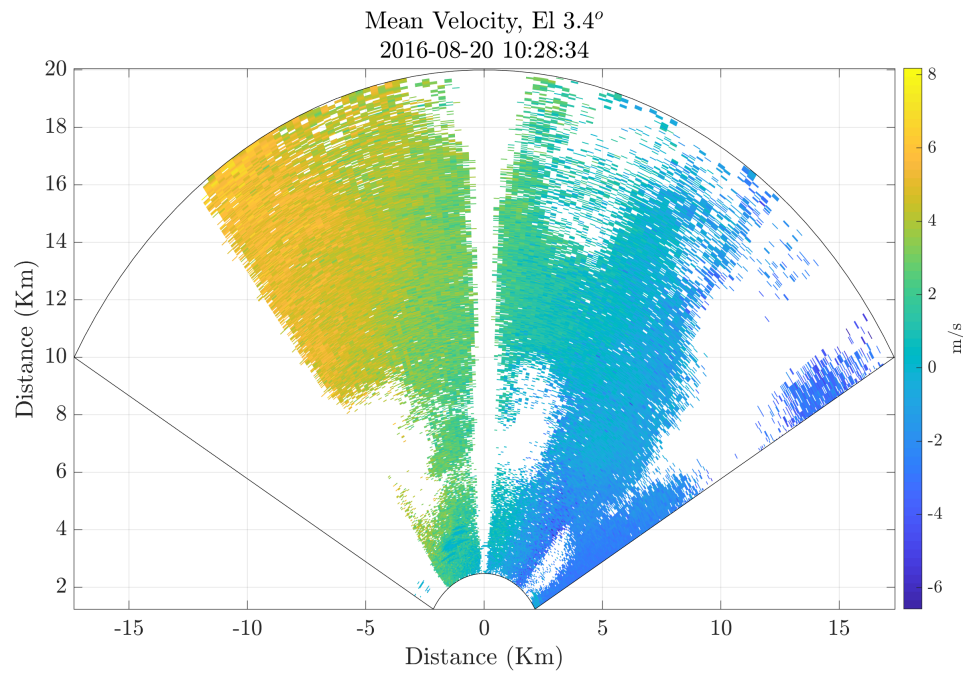
(a) Radial Velocity PPI
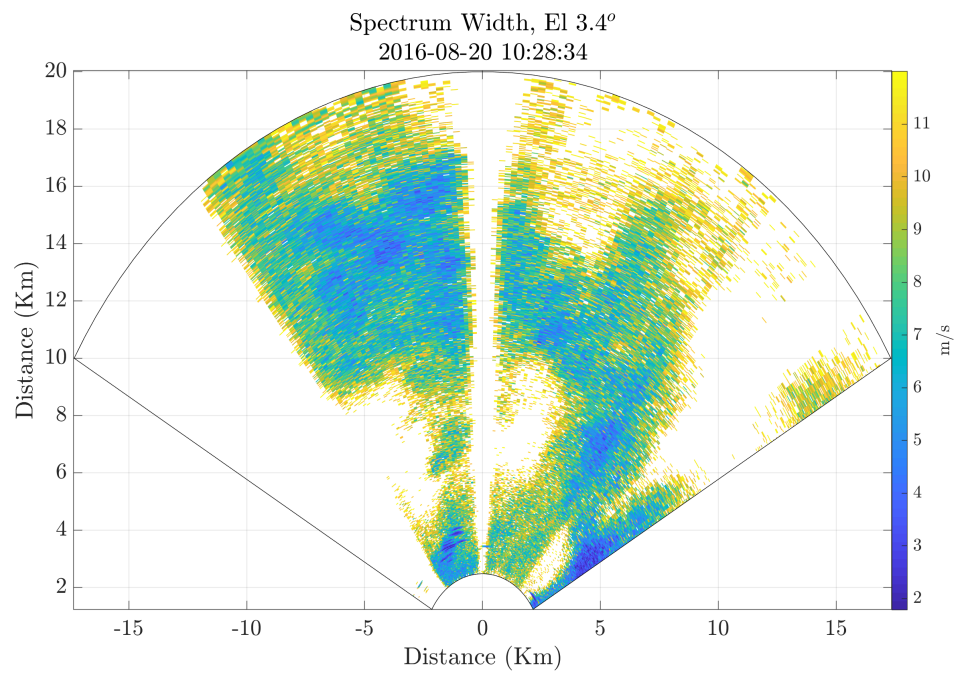
(b) Spectrum Width PPI

Figure 6.15: Ground Measurement: Radial Velocity and Spectrum Width Plots

134
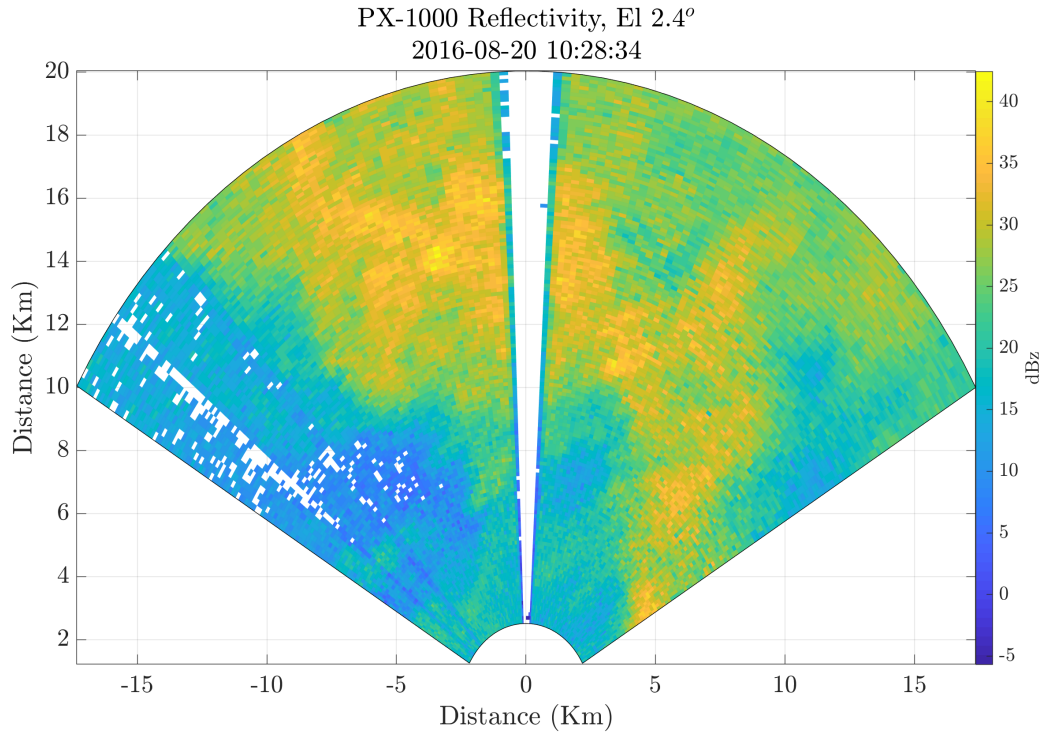
Figure 6.16: Ground Based Case: PX-1000 Reflectivity PPI

contain weather event. Again, Spectrum Width is highly dependent on the SNR, and a less severe weather event (like moderate rain) may not necessarily produce enough SNR for a proper calculation of Spectrum Width.

6.3.1 Comparison with PX-1000

In this ground measurement case, PX-1000 radar data was also used for comparisons. Figures 6.16, 6.17a, and 6.17b show the PPI plots for Reflectivity, Radial Velocity, and Spectrum Width, respectively (from PX-1000). In the data, there is a single beam blockage due to NOAA's National Weather Radar Testbed (NWRT) building. The general trend in Reflectivity matches quite well to the return power in PARADOX1 data. As in the PARADOX1 case, the velocity values transition from negative values in right side of the plot to
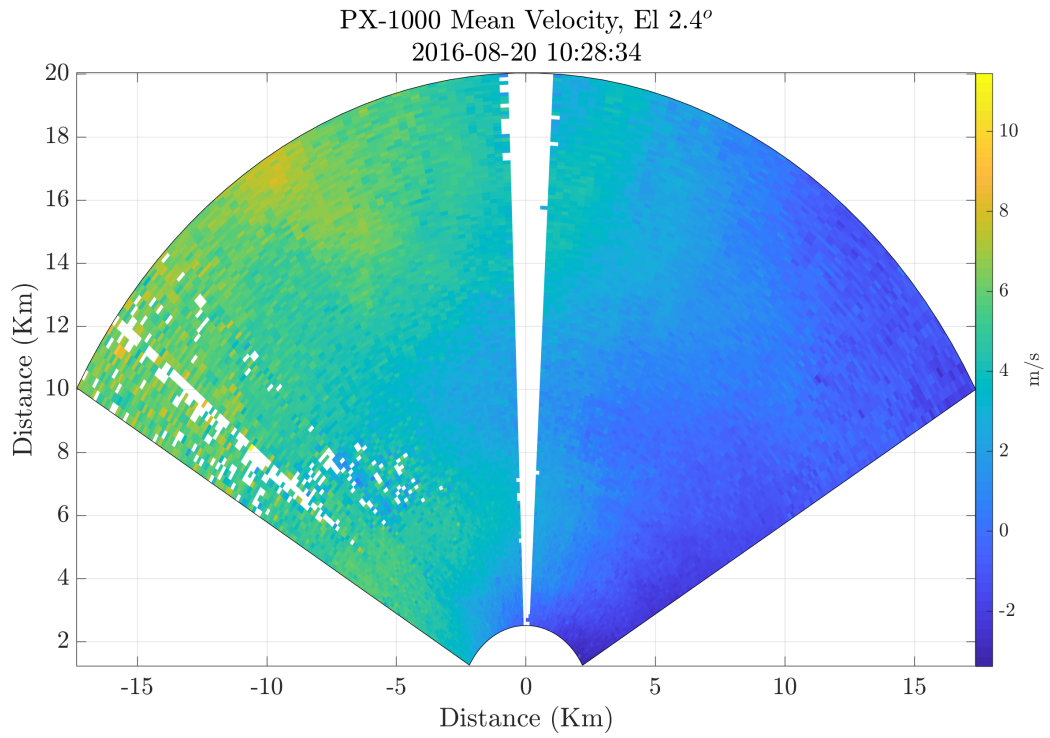
(a) PX-1000 Radial Velocity PPI
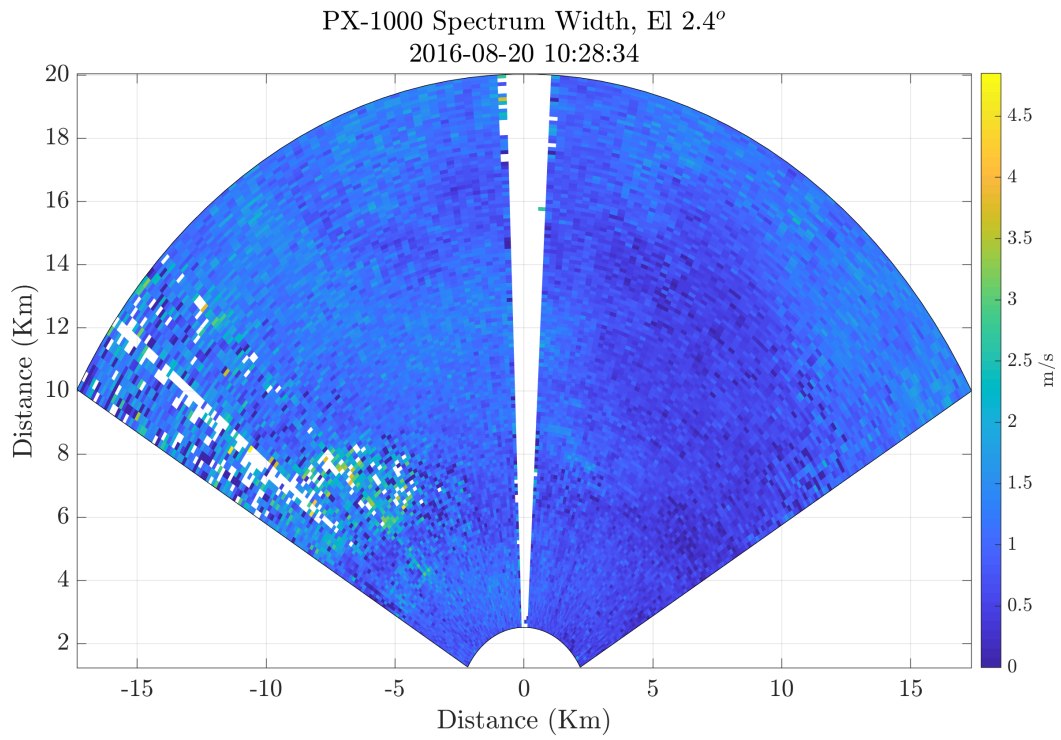
(b) PX-1000 Spectrum Width PPI

Figure 6.17: Ground Based Case: PX-1000 Radial Velocity and Spectrum Width PPI

zero values in the middle of the plot and finally to positive values in the left side of the plot. The above mentioned (in PARADOX1 case) theory seems to be complimented by PX-1000 velocity data as well. Although PARADOX1 and PX-1000 are close to each other, comparison of actual velocity values is refrained because of the difference in elevations of PARADOX1 and PX-1000 data. Rainwater is being moved due to the wind (with unknown speed and direction) as well as regions with updraft and downdraft (also unknown). Since PARADOX1 is scanning at higher elevation in this case, Radial Velocity estimation includes larger contribution from the terminal velocity as well as updraft/downdraft components (of true rain velocity). The Spectrum Width plot in PX-1000 case shows a lot of lower values, mostly less than 2 m/s. In PARADOX1 case, the area with higher power returns exhibits lower Spectrum Width values. Again, apart from the number-to-number comparison, the trend of Spectrum Width values match in both cases.

6.3.2   Comparison with NEXRAD/KTLX

Next, the results from NEXRAD radar (KTLX in Oklahoma City, OK) is examined and compared with PARADOX1 returns. Figure 6.18a shows the location of radar and the field of view of PARADOX1 in KTLX PPI plot. KTLX was about 25 km away from the PARADOX1 location in North-East direction. As aforementioned, the elevation of KTLX was chosen in such a way that the main beam illuminates the weather region in 14 km heading and -5 km cross-heading direction from PARADOX1 point of view. Figure 6.18b shows the Reflectivity from KTLX radar as a field of view from PARADOX1. The Reflectivity plot shows a good agreement with PARADOX1 radar, especially in the target area.
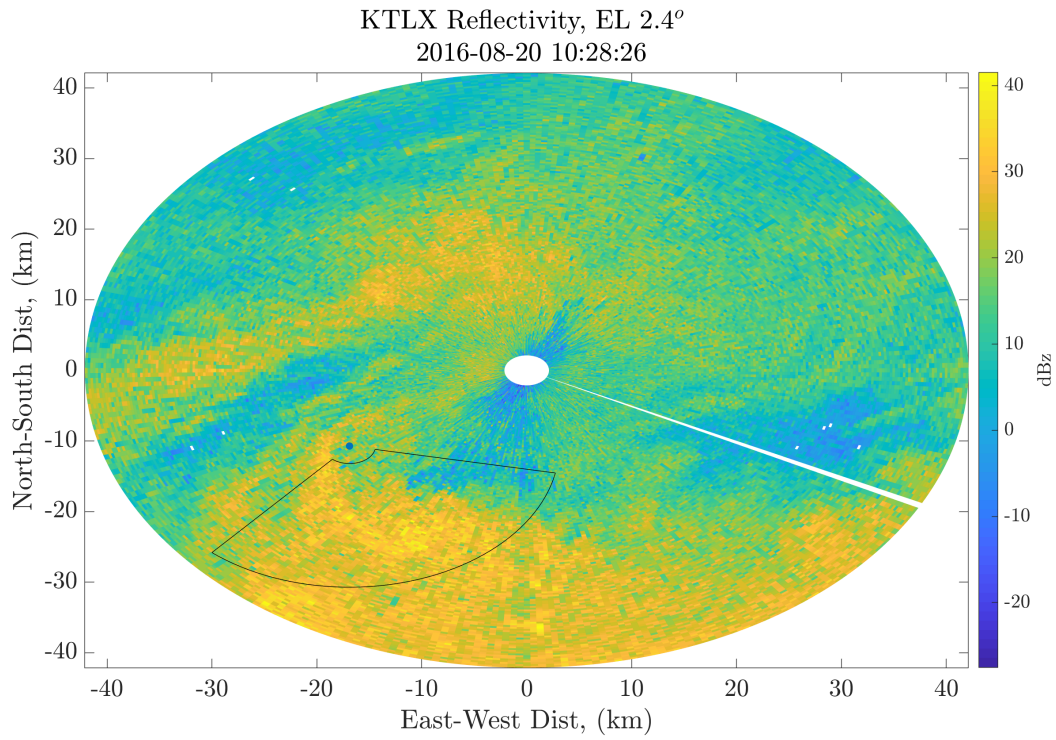
(a) PARADOX1 Field of View in KTLX PPI Ground Based Case

(b) KTLX Reflectivity PPI

Figure 6.18: Ground Based Case: KTLX Reflectivity PPI
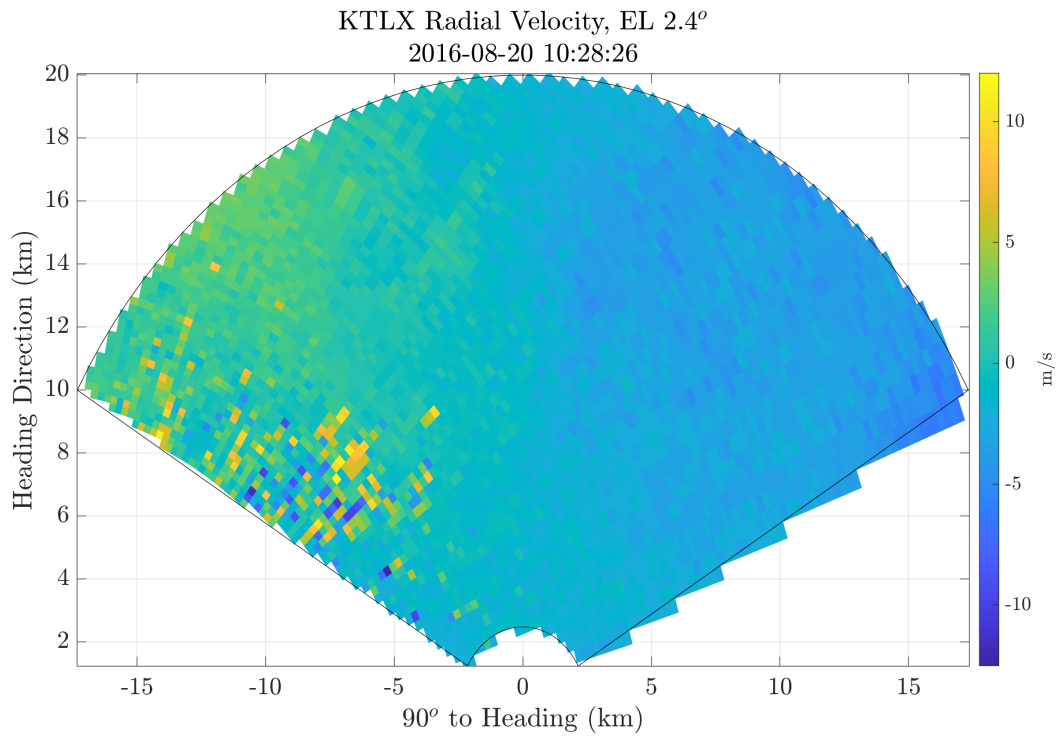
(a) PX-1000 Radial Velocity PPI
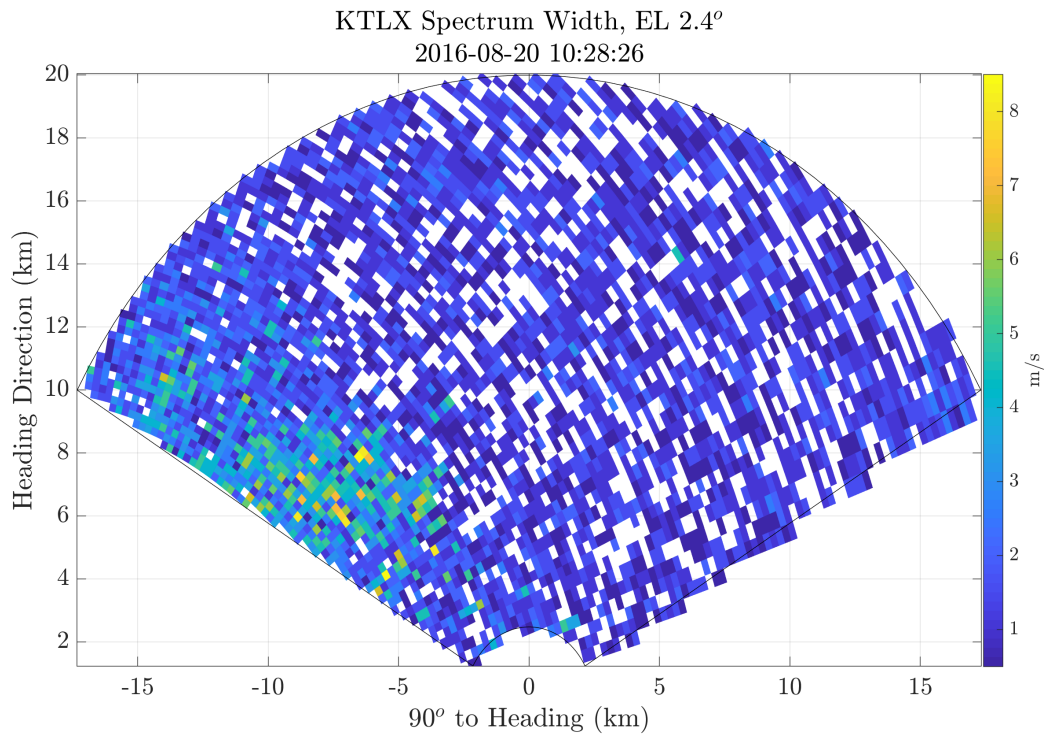
(b) PX-1000 Spectrum Width PPI

Figure 6.19: Ground Based Case: KTLX Radial Velocity and Spectrum Width PPI
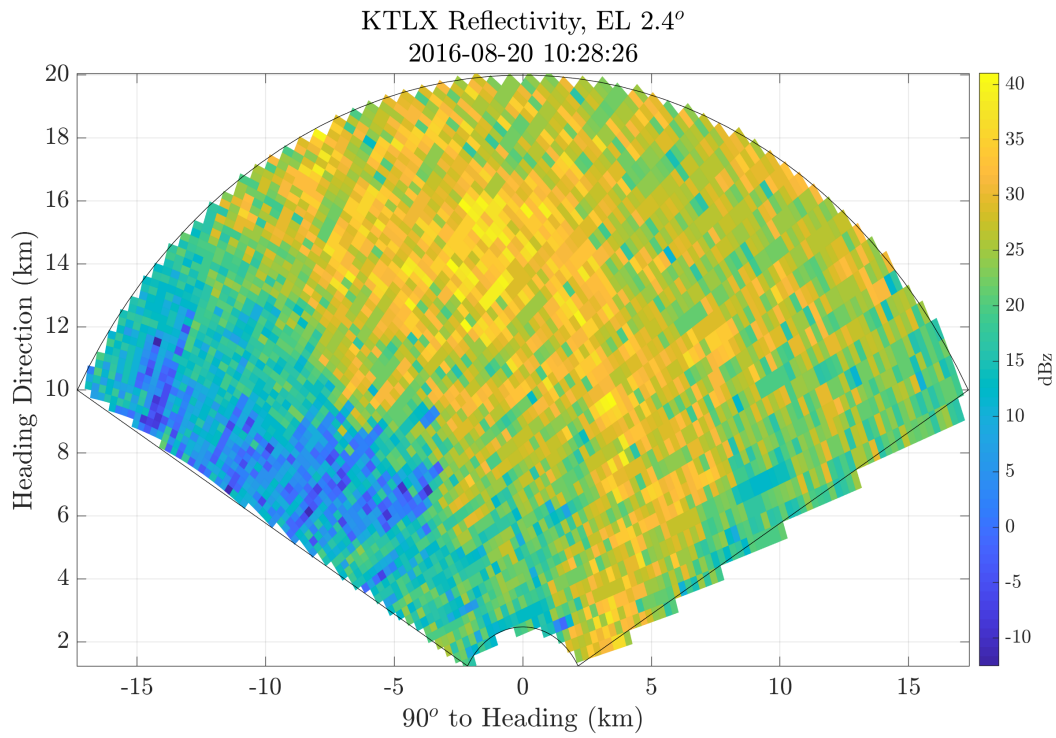
The Radial Velocity PPI is depicted in Figure 6.19a. As seen in the PPI, the trend of velocity is negative on the right side, zero in the center and positive values on the left side of the plot. This trend matches with the trend of PARADOX1 and is compatible with the theory of wind blowing rain from West to East direction. Again, actual velocity values are not compared due to the differences in aspect angle as well as elevation angles as the terminal velocity components might differ. Finally, the Spectrum Width plot shows a lot of empty values. It is public knowledge that NEXRAD has a stringent data quality control procedure after which some data are marked as unreliable. Speculating the exact procedure to get to the conclusion of missing data from the above Spectrum Width plot is refrained.

6.4   Summary and Conclusions

The weather surveillance functionality of the multi-mission airborne radar, PARADOX1, was evaluated in this Chapter. PARADOX1 radar was used in an airborne as well as a ground-based configuration to measure the data originating from various weather conditions. For the ground measurement, RMMSE algorithm was used for azimuthal super-resolution, and the results were compared with ground-based PX-1000 radar. In addition to that, the PPI scans of return power, Radial Velocity as well as Spectrum Width were generated and compared with those of PX-1000 as well as nearby NEXRAD (KTLX). The results show a good agreement between the PARADOX1 return power and Reflectivity from both PX-1000 and NEXRAD in the weather region. Since Radial Velocity is highly dependent on aspect angle, only the overall trend of velocity distribution was examined. The results, again, show agreement with both PX-1000 and NEXRAD. Spectrum Width, on the other hand, exhibited

higher values in case of PARADOX1 which is attributed to low SNR.

Additionally, weather data was measured in a flight campaign near Oklahoma City, OK, using PARADOX1. Similar to the ground-based test, PPIs for return power, noise-removed return power, Radial Velocity as well as Spectrum Width were generated. Those plots were compared against NEXRAD data from the same weather region. The weather is "looked down upon" from PARADOX1 while KTLX "looks up to" the weather. In addition, Constant Altitude PPI (CAPPI) plots were also generated from KTLX and the results were compared. The Reflectivity and return power plots bear resemblance with each other. Similar to the ground-based test, accurate comparison of velocity measurements couldn't be performed due to the difference in aspect angle. Also similar to the ground-based test scenario, Spectrum Width showed higher values which is, again, attributed to the SNR. In conclusion, PARADOX1's is verified to be a capable radar for weather moment measurements. Compared to ground-radars, it has better range resolution, but poorer azimuthal resolution, and lower SNR values.

Chapter 7

Summary and Conclusions

This study introduces a **P**olarimetric **A**irborne **Rad**ar **O**perating at **X**-band Version 1 (PARADOX1) as an airborne multi-mission radar. The radar hardware itself is developed in collaboration with Garmin International and its GSX-70 line of airborne radars. The necessity of an airborne multi-mission radar originates from the overlapping interests and goals of various scientific as well as commercial entities. There is an apparent need for airborne research quality data that is essential not only for weather and climate related studies but also for research related to earth's surface conditions like deforestation, ice sheet status, etc. Sense and Avoid (SAA) or sometimes referred to as Detect and Avoid (DAA) is another emerging field that is increasingly being recognized by various commercial and government agencies. Considering the practical needs of various communities, a proper study of a multi-mission airborne radar was necessary.

In contrast to proposing an entirely new hardware platform, this study focuses on development as well as implementation of various signal processing algorithms to achieve a multi-mission capability on a commercial airborne weather radar platform. This approach leads to more rapid implementations as testing, validating, and certifying a completely new hardware is often sluggish

and carries more risk of failure to achieve specified goals on time. Therefore, this study provides a blueprint for various signal processing algorithms that are of interest to realize a multi-mission airborne radar.

The characteristics of radar signals in terms of power and frequency content is examined in detail in Chapter 2. The chapter builds on fundamentals of radar signals not only for point targets but also for distributed targets. The effects of platform motion onto the spectrum of radar signals are derived and discussed. As signal processing is presented as a viable solution to achieve multi-mission capability, an algorithm suite is presented in Chapter 3. Data quality concerns, using both airborne and ground based configurations are discussed in Chapter 6.

In addition to the algorithm suite, a realistic simulation environment is also presented in Chapter 3. The simulation environment provides a method of generating data using a variety of combinations of radar parameter values and environment/target variables. This simulation environment has been a part of previous studies like [47]. In this study, the simulation environment is used to evaluate and validate super-resolution algorithms by generating returns when various transmit waveforms are used. The simulation also provided the data with desired noise level to study the algorithms' performance with regard to various SNR levels. The simulation environment was also used to generate a series of scans for a scenario containing two close-by airborne targets. The simulation was based on air-to-air scanning scenario and the radar parameters were similar to that of PARADOX1. Other environmental parameters like radar platform motion, target RCS fluctuations, false detections, etc. were also applied. This data was used to validate the SAA tracking functionality.

Weather measurement data from PARADOX1 is scrutinized to determine if

the data meets the research quality threshold. For that purpose, PARADOX1 was used in airborne as well as ground based configurations to measure weather data. The measured weather data was fed through various signal processing algorithms described in Chapter 3 and the results were compared against NEXRAD (KTLX at Oklahoma City, OK) radar data as well as data from a research radar named PX-1000 [107], [108]. The similarities as well as differences among the results from PARADOX1 and these well known scientific/research radars are discussed in Chapter 6. The results show that, indeed, PARADOX1 radar is able to measure research quality data and enhancements on the data can be made through various signal processing algorithms. One significant difference from those comparisons was in the result of Spectrum Width estimation. The major contributor for this difference is considered to be the Signal to Noise Ratio (SNR). Since PARADOX1 radar is a low C-SWaP radar, the SNR is always expected to be lower than the high powered ground based radars.

Another difference, although not always apparent, originates from the limited aperture size. PARADOX1 uses a 12 inch planar slotted waveguide array antenna in the airborne configuration while that of 18 inches is used in the ground based configurations. The resulting beamwidth is not nearly as fine as in case of the ground based radars like NEXRAD and PX-1000. However, a class of pulse compression algorithms called Adaptive Pulse Compression (APC) is discussed to mitigate the effect of lower aperture size. Reiterated Minimum Mean Square Error, RMMSE, algorithm [90] is used to enhance the resolution and the results are presented in Chapter 5 and Chapter 6.

In addition to RMMSE, two super-resolution algorithms in range-Doppler domain called Iterative Adaptive Approach (IAA) [56] and Matched Filter based Iterative Adaptive Approach (MF-IAA) [57] are presented in Chapter 4.

Both of these algorithms are non-parametric, iterative, weighted least square based spectral estimation algorithms. IAA operates on "raw" I/Q returns whereas MF-IAA operates on Matched Filter output to generate a resolution enhanced range-Doppler map using iterative methods. These algorithms are derived from a convolution based problem formulation. The algorithms were examined and evaluated using simulated as well as measured data. In the simulated data, a variety of transmit waveforms as well as SNR levels were chosen to analyze the performance of both IAA, and MF-IAA algorithms. The results show that resolution enhancement using IAA and MF-IAA is possible. Furthermore, PARADOX1 was used to measured ground based target (Water Tower) as well as airborne target (Piper Seneca Aircraft). IAA and MF-IAA algorithms were applied to the measured data and the results were compared against the results from the traditional Matched Filter data. The comparisons validated the simulation results. When IAA was compared against MF-IAA for the airborne target, IAA performed better than MF-IAA. Those results are presented in Chapter 4.

Sense and Avoid functionality is considered as a core capability of an airborne multi-mission radar. Tracking of airborne targets from SAA perspective is discussed using Kalman Filter and Joint Probabilistic Data Association in Chapter 2. As most of airborne targets can be considered friendly and not performing any evasive maneuvering, the motion model consisted of "nearly" constant acceleration model. The related theories, equations as well as appropriate derivations are presented in Chapter 2. Since coordinating flights of multiple close by targets was difficult, the aforementioned simulation environment was used to generate such data. The data was then used to validate the RMMSE super-resolution algorithm and then perform a two-target tracking.

Additionally, PARADOX1 was placed on a roof top and a real-time tracking was performed by coordinating a flight with University of Oklahoma, School of Aviation. This demonstrated the SAA tracking capability of PARADOX1 radar. The results show the error of deviation during tracking to be in an acceptable region. The discussions as well as the results are presented in Chapter 5.

In this study, PARADOX1 is presented as a low C-SWaP (Cost, Size, Weight, and Power) multi-mission airborne radar. The limitations of PARADOX1 radar are alleviated using both mature and novel signal processing algorithms and techniques. Range, azimuth, and Doppler super-resolution algorithms are developed and discussed that enhanced the capability of PARADOX1. A modular solution to multi-mission in an airborne platform is presented and validated. This study shows that using modular software based solution in an existing radar hardware can be a viable path to achieving multi-mission capability in an airborne platform.

Chapter 8

Future Work

While this study provides an initial framework for a multi-mission airborne radar, there are a lot of paths forward. As mentioned throughout this study, PARADOX1 is just the latest iteration of an ongoing study of multi-mission capable airborne radar. The future versions of PARADOX will most certainly have various hardware upgrades. For instance, the current generation consists of a vertically polarized antenna which can be upgraded to a dual polarization capable antenna in the future. Furthermore, as technology advances and the costs subside, the various components of the the radar systems can be upgraded to provide higher bandwidth and/or lower noise figure as well as other enhancements while still maintaining the low C-SWaP profile. Undoubtedly, these hardware upgrades will enhance the capability of future versions of PARADOX as a true airborne multi-mission radar.

On the signal processing side, which is the focus of this study, there are potential areas of advancement. There will always be need of higher resolution and while some of the resolution enhancement may be provided by improvement in hardware, there will still be an appetite for resolution enhancement through signal processing. Continued studies in Adaptive Pulse Compression and Super-Resolution will pave the way for sub-meter resolution which will introduce

more capabilities in the future. The aperture size limitation is one of the most apparent shortcomings of PARADOX1. While it is possible to include larger antenna, such actions deviate from the core principle of maintaining a low C-SWaP profile. Therefore, novel signal processing techniques can be studied and employed to achieve better resolution in angular domain. On the Doppler estimations, PARADOX1 is already capable of transmitting CPI's with multiple combinations of pulse length, PRF, waveform bandwidth, etc. Two staggered PRF's and the associated data was examined in this study, and in the future, more of such staggered PRF's can be employed and the results examined. The Spectrum Width estimation in this study did not obtain high quality due to low SNR. More studies on proper estimation can be done to achieve similar results as the ground based radars. Potential sources of error during Spectrum Width estimations are studied previously [110], [111]. These studies can be extended to provide more accurate Spectrum Width in cases with lower overall SNR.

This study validated SAA tracking with a single airborne target while PARADOX1 was at the ground. Although costly, a multi-target air-to-air SAA tracking test can be performed not only to validate current algorithm but also to discover any potential limitations in the actual operational environments. The target motion models can be upgraded to include Interactive Multiple Model (IMM) [112], [113] which can aid in proper state estimation even for maneuvering targets. Similarly, Joint Probabilistic Data Association algorithm can be improved using, for example [114] for more efficient data association.

References

[1] S. S. Swords, *Technical history of the beginnings of radar*. IET, 1985.

[2] M. Richards, *Fundamentals of Radar Signal Processing*. 2005.

[3] R. J. Doviak *et al.*, *Doppler radar and weather observations*. Courier Corporation, 1993.

[4] D. Atlas, Ed., *Radar in Meteorology: Battan Memorial and 40th Anniversary Radar Meteorology Conference*, American Meteorological Society, 1990, ISBN: 978-1-935704-15-7.

[5] R. J. Serafin and J. W. Wilson, "Operational weather radar in the united states: Progress and opportunity", *Bulletin of the American Meteorological Society*, vol. 81, no. 3, pp. 501–518, Mar. 2000, ISSN: 0003-0007, 1520-0477. DOI: `10.1175/1520-0477(2000)081<0501:OWRITU>2.3.CO;2`.

[6] T. D. Crum and R. L. Alberty, "The wsr-88d and the wsr-88d operational support facility", *Bulletin of the American Meteorological Society*, vol. 74, no. 9, pp. 1669–1688, 1993.

[7] T. D. Crum, R. L. Alberty, and D. W. Burgess, "Recording, archiving, and using WSR-88d data", *American Meteorological Society*, vol. 74, no. 4, pp. 645–654, 1993.

[8] T. D. Crum, R. E. Saffle, and J. W. Wilson, "An update on the NEXRAD program and future WSR-88d support to operations", *Weather and Forecasting*, vol. 13, no. 2, pp. 253–262, Jun. 1998, ISSN: 0882-8156, 1520-0434. DOI: `10.1175/1520-0434(1998)013<0253:AUOTNP>2.0.CO;2`. [Online]. Available: `http://journals.ametsoc.org/doi/abs/10.1175/1520-0434%281998%29013%3C0253%3AAUOTNP%3E2.0.CO%3B2` (visited on 11/09/2018).

[9]   NOAA National Weather Service (NWS) Radar Operations Center.
       (1991). NOAA Next Generation Radar (NEXRAD) Level 2 Base Data.
       NOAA National Centers for Environmental Information, [Online]. Avail-
       able: `https://www.ncdc.noaa.gov/nexradinv/chooseday.jsp?id=`
       `ktlx` (visited on 05/28/2017).

[10]   *MMR - Multi-Mission Radar | SRC, Inc.* [Online]. Available: `https:`
       `//www.srcinc.com/what-we-do/radar-and-sensors/mmr.html`
       (visited on 08/26/2018).

[11]   *Highly Adaptable Multi-Mission Radar (HAMMR)*, en-us. [Online]. Avail-
       able: `https://www.northropgrumman.com/Capabilities/hammr/`
       `Pages/default.aspx` (visited on 08/26/2018).

[12]   *Israel Aerospace Industries Ltd. - Groups Elta Number Products ELM-
       2084 Systems Ground.* [Online]. Available: `http://www.iai.co.il/`
       `2013/34481-41832-en/Groups_ELTA_EltaNumber_Products-ELM.`
       `aspx` (visited on 08/26/2018).

[13]   M. Weber, J. Cho, J. Flavin, J. Herd, and M. Vai, "MULTI-FUNCTION
       PHASED ARRAY RADAR FOR u.s. CIVIL-SECTOR SURVEIL-
       LANCE NEEDS", p. 11,

[14]   J. Evans and D. Turnbull, "Development of an automated windshear
       detection system using doppler weather radar", *Proceedings of the IEEE*,
       vol. 77, no. 11, pp. 1661–1673, Nov. 1989, ISSN: 0018-9219. DOI: `10.`
       `1109/5.47729`.

[15]   J. W. Taylor and G. Brunins, "Design of a new airport surveillance
       radar (ASR-9)", *Proceedings of the IEEE*, vol. 73, no. 2, pp. 284–289,
       Feb. 1985, ISSN: 0018-9219. DOI: `10.1109/PROC.1985.13139`.

[16]   D. E. Forsyth, "National weather radar testbed:" Defense Techni-
       cal Information Center, Fort Belvoir, VA, Sep. 30, 2003. DOI: `10.`
       `21236/ADA630030`. [Online]. Available: `http://www.dtic.mil/docs/`
       `citations/ADA630030` (visited on 10/23/2018).

[17]   M. Yeary, G. Crain, A. Zahrai, R. Kelley, J. Meier, Y. Zhang, I. Ivic,
       C. Curtis, R. Palmer, T. Yu, and R. Doviak, "An update on the multi-
       channel phased array weather radar at the national weather radar
       testbed", in *2011 IEEE RadarCon (RADAR)*, May 2011, pp. 971–973.
       DOI: `10.1109/RADAR.2011.5960680`.

[18]   S. M. Torres, R. Adams, C. D. Curtis, E. Forren, D. E. Forsyth, I. R. Ivić, D. Priegnitz, J. Thompson, and D. A. Warde, "Adaptive-weather-surveillance and multifunction capabilities of the national weather radar testbed phased array radar", *Proceedings of the IEEE*, vol. 104, no. 3, pp. 660–672, Mar. 2016, ISSN: 0018-9219. DOI: 10.1109/JPROC.2015.2484288.

[19]   M. E. Weber, J. Y. N. Cho, J. S. Herd, J. M. Flavin, W. E. Benner, and G. S. Torok, "The next-generation multimission u.s. surveillance radar network", *Bulletin of the American Meteorological Society*, vol. 88, no. 11, pp. 1739–1752, Nov. 2007, ISSN: 0003-0007, 1520-0477. DOI: 10.1175/BAMS-88-11-1739.

[20]   J. Herd, D. Carlson, S. Duffy, M. Weber, G. Brigham, M. Rachlin, D. Cursio, C. Liss, and C. Weigand, "Multifunction phased array radar (MPAR) for aircraft and weather surveillance", in *2010 IEEE Radar Conference*, May 2010, pp. 945–948. DOI: 10.1109/RADAR.2010.5494483.

[21]   J. Herd, S. Duffy, D. Carlson, M. Weber, G. Brigham, C. Weigand, and D. Cursio, "Low cost multifunction phased array radar concept", in *2010 IEEE International Symposium on Phased Array Systems and Technology*, Oct. 2010, pp. 457–460. DOI: 10.1109/ARRAY.2010.5613327.

[22]   G. Zhang, S. Karimkashi, L. Lei, R. Kelley, J. Meier, R. Palmer, C. Futon, R. J. Doviak, A. Zahrai, D. S. Zrnic, *et al.*, "A cylindrical polarimetric phased array radar concept—a path to multi-mission capability", in *Phased Array Systems & Technology, 2013 IEEE International Symposium on*, IEEE, 2013, pp. 481–484.

[23]   S. Karimkashi, G. Zhang, R. Kelley, J. Meier, R. Palmer, A. Zahrai, R. J. Doviak, and D. S. Zrnic, "Cylindrical polarimetric phased array radar demonstrator: Design and analysis of a frequency scanning antenna array", in *2013 IEEE International Symposium on Phased Array Systems and Technology*, Oct. 2013, pp. 477–480. DOI: 10.1109/ARRAY.2013.6731874.

[24]   S. Karimkashi and G. Zhang, "Optimizing radiation patterns of a cylindrical polarimetric phased-array radar for multimissions", *IEEE Transactions on Geoscience and Remote Sensing*, vol. 53, no. 5, pp. 2810–2818, May 2015, ISSN: 0196-2892. DOI: 10.1109/TGRS.2014.2365362.

[25] Y. Pan, Y. Zhang, and S. Karimkashi, "Broadband low-cost reflectarray for multi-mission radar applications", in *2012 IEEE Radar Conference*, May 2012, pp. 0613–0617. DOI: 10.1109/RADAR.2012.6212213.

[26] C. Fulton, G. Zhang, W. Bocangel, L. Lei, R. Kelley, and M. McCord, "Cylindrical polarimetric phased array radar: A multi-function demonstrator and its calibration", in *2013 IEEE International Conference on Microwaves, Communications, Antennas and Electronic Systems (COMCAS 2013)*, Oct. 2013, pp. 1–5. DOI: 10.1109/COMCAS.2013.6685315.

[27] S. Perera, Y. Zhang, D. Zrnic, R. Doviak, S. Perera, Y. Zhang, D. Zrnic, and R. Doviak, "Electromagnetic simulation and alignment of dual-polarized array antennas in multi-mission phased array radars", *Aerospace*, vol. 4, no. 1, p. 7, Feb. 10, 2017. DOI: 10.3390/aerospace4010007.

[28] J. CAI, Y. R. Zhang, and F. Kong, "Acceleration of advanced radar processing chain and adaptive pulse compression using GPGPU", Society for Modeling and Simulation International (SCS), 2016, ISBN: 978-1-5108-2318-1. DOI: 10.22360/SpringSim.2016.HPC.008.

[29] J. CAI, "Advanced aviation weather radar data processing and real time implementations", PhD thesis, The University of Oklahoma, Norman, OK, 2017.

[30] J. Cai and Y. R. Zhang, "General purpose graphic processing unit implementation of adaptive pulse compression algorithms", *Journal of Applied Remote Sensing*, vol. 11, no. 3, p. 035 009, Aug. 2017, ISSN: 1931-3195, 1931-3195. DOI: 10.1117/1.JRS.11.035009.

[31] P. H. Hildebrand, W.-C. Lee, C. A. Walther, C. Frush, M. Randall, E. Loew, R. Neitzel, R. Parsons, J. Testud, F. Baudin, and A. LeCornec, "The ELDORA/ASTRAIA airborne doppler weather radar: High-resolution observations from TOGA COARE", *Bulletin of the American Meteorological Society*, vol. 77, no. 2, pp. 213–232, Feb. 1996, ISSN: 0003-0007, 1520-0477. DOI: 10.1175/1520-0477(1996)077<0213:TEADWR>2.0.CO;2.

[32] P. H. Hildebrand, C. A. Walther, C. L. Frush, J. Testud, and F. Baudin, "The ELDORA/ASTRAIA airborne doppler weather radar: Goals, design, and first field tests", *Proceedings of the IEEE*, vol. 82, no. 12, pp. 1873–1890, Dec. 1994, ISSN: 0018-9219. DOI: 10.1109/5.338076.

[33] S. L. Durden, E. Im, F. Li, W. Ricketts, A. Tanner, and W. Wilson, "ARMAR: An airborne rain-mapping radar", *Journal of Atmospheric and Oceanic Technology*, vol. 11, no. 3, pp. 727–737, 1994. DOI: `10.1175/1520-0426(1994)011<0727:AAARMR>2.0.CO;2`.

[34] F. Li, S. L. Durden, E. Im, A. Tanner, W. Ricketts, W. Wilson, R. Meneghini, T. Iguchi, and K. Nakamura, "Airborne rain mapping radar and preliminary observations during TOGA/COARE", in *Proceedings of IGARSS '93 - IEEE International Geoscience and Remote Sensing Symposium*, Aug. 1993, 832–834 vol.2. DOI: `10.1109/IGARSS.1993.322208`.

[35] R. J. Keeler and R. E. Passarelli, "Signal processing for atmospheric radars", in *Radar in Meteorology*, D. Atlas, Ed., Boston, MA: American Meteorological Society, 1990, pp. 199–229, ISBN: 978-1-935704-15-7. DOI: `10.1007/978-1-935704-15-7_21`.

[36] R. M. Wakimoto, W.-C. Lee, H. B. Bluestein, C.-H. Liu, and P. H. Hildebrand, "ELDORA observations during VORTEX 95", *Bulletin of the American Meteorological Society*, vol. 77, no. 7, pp. 1465–1481, Jul. 1996, ISSN: 0003-0007, 1520-0477. DOI: `10.1175/1520-0477(1996)077<1465:EODV>2.0.CO;2`.

[37] S. L. Durden, Z. S. Haddad, and T. P. Bui, "Correction of doppler radar data for aircraft motion using surface measurements and recursive least squares estimation", *Journal of Atmospheric and Oceanic Technology*, vol. 16, no. 12, pp. 2026–2029, Dec. 1999, ISSN: 0739-0572, 1520-0426. DOI: `10.1175/1520-0426(1999)016<2026:CODRDF>2.0.CO;2`.

[38] W.-C. Lee, P. Dodge, F. D. Marks, and P. H. Hildebrand, "Mapping of airborne doppler radar data", *Journal of Atmospheric and Oceanic Technology*, vol. 11, no. 2, pp. 572–578, 1994. DOI: `10.1175/1520-0426(1994)011<0572:MOADRD>2.0.CO;2`.

[39] K. R. Chan, J. Dean-Day, S. W. Bowen, and T. P. Bui, "Turbulence measurements by the DC-8 meteorological measurement system", *Geophysical Research Letters*, vol. 25, no. 9, pp. 1355–1358, May 1, 1998, ISSN: 00948276. DOI: `10.1029/97GL03590`. [Online]. Available: `http://doi.wiley.com/10.1029/97GL03590` (visited on 10/28/2018).

[40] V. N. Bringi and V Chandrasekar, "POLARIMETRIC DOPPLER WEATHER RADAR: Principles and applications", p. 664,

[41] G. Zhang, *Weather radar polarimetry*. Boca Raton: Taylor & Francis, 2016, ISBN: 978-1-4398-6958-1.

[42] M. J. Kochenderfer and J. P. Chryssanthacopoulos, "Robust airborne collision avoidance through dynamic programming", p. 118, Jan. 2011.

[43] B. C. Karhoff, J. I. Limb, S. W. Oravsky, and A. D. Shephard, "Eyes in the domestic sky: An assessment of sense and avoid technology for the army's "warrior" unmanned aerial vehicle", in *2006 IEEE Systems and Information Engineering Design Symposium*, Apr. 2006, pp. 36–42. DOI: 10.1109/SIEDS.2006.278710.

[44] UAS Task Force, "Unmanned aircract system airspace integration plan, version 2.0, march 2011", Mar. 1, 2011. [Online]. Available: https://www.hsdl.org/?abstract&did= (visited on 10/23/2018).

[45] J Everaerts, "THE USE OF UNMANNED AERIAL VEHICLES (UAVS) FOR REMOTE SENSING AND MAPPING", p. 6, 2008.

[46] D. A. Haessig, R. T. Ogan, and M. Olive, ""sense and avoid" - what's required for aircraft safety?", in *SoutheastCon 2016*, Mar. 2016, pp. 1–8. DOI: 10.1109/SECON.2016.7506724.

[47] R. Nepal, Z. Yan (Rockee), and J. Cai, "Micro-doppler radar signature identification within wind turbine clutter based on short-CPI airborne radar observations", *IET Radar, Sonar & Navigation*, vol. 9, no. 9, pp. 1268–1275, Dec. 1, 2015, ISSN: 1751-8784, 1751-8792. DOI: 10.1049/iet-rsn.2015.0111.

[48] E. Ackerman. (Nov. 8, 2016). Metamaterial radar is exactly what delivery drones need, IEEE Spectrum: Technology, Engineering, and Science News.

[49] J. P. John, J. Kirchgessner, R. Ma, D. Morgan, I. To, and V. P. Trivedi, "Si-based technologies for mmWave automotive radar", in *2016 IEEE Compound Semiconductor Integrated Circuit Symposium (CSICS)*, Oct. 2016, pp. 1–4. DOI: 10.1109/CSICS.2016.7751064.

[50] G. Fasano, D. Accado, A. Moccia, and D. Moroney, "Sense and avoid for unmanned aircraft systems", *IEEE Aerospace and Electronic Systems Magazine*, vol. 31, no. 11, pp. 82–110, Nov. 2016, ISSN: 0885-8985. DOI: 10.1109/MAES.2016.160116.

[51] RTCA Subcommittee 228, "Minimum operational performance standards (MOPS) for air-to-air radar for detect and avoid systems", Washington DC, USA, Aug. 2016.

[52] ASTM F2411-07, *Standard specification for design and performance of an airborne sense and avoid system*, West Conshohocken, PA, 2007.

[53] *Due regard radar (developmental)*, General Atomics Aeronautical Systems Inc. [Online]. Available: `http://www.ga-asi.com/due-regard-radar-developmental` (visited on 08/22/2018).

[54] D. Accardo, G. Fasano, L. Forlenza, A. Moccia, and A. Rispoli, "Flight test of a radar-based tracking system for UAS sense and avoid", *IEEE Transactions on Aerospace and Electronic Systems*, vol. 49, no. 2, pp. 1139–1160, Apr. 2013, ISSN: 0018-9251. DOI: `10.1109/TAES.2013.6494404`.

[55] Y. Zhang, Z. Li, B. Cheong, J. Cai, R Nepal, H. Suarez, W. Blake, J. Andrews, and T. Yong, "Optimized radar signal processing for a low-cost, solid-state airborne radar", in *36th Conference on Radar Meteorology*, 2013, pp. 16–20.

[56] Z. Li, R. Nepal, Y. Zhang, and W. Blake, "Efficient pulse compression for lpi waveforms based on a nonparametric iterative adaptive approach", in *Radar Sensor Technology XIX; and Active and Passive Signatures VI*, International Society for Optics and Photonics, vol. 9461, 2015, p. 94610X.

[57] R. Nepal, Y. R. Zhang, Z. Li, and W. Blake, "Matched filter based iterative adaptive approach", in *SPIE Defense+ Security*, International Society for Optics and Photonics, 2016, pp. 982 912–982 912.

[58] R. Nepal, Y. Zhang, and W. Blake, "Sense and avoid airborne radar implementations on a low-cost weather radar platform", *Aerospace*, vol. 4, no. 1, p. 11, Mar. 1, 2017, ISSN: 2226-4310. DOI: `10.3390/aerospace4010011`.

[59] R. Nepal, Y. R. Zhang, G. Zhang, A. Ryzhkov, and W. Blake, "Data quality analysis and enhancement of an airborne weather radar for scientific and multi-mission operations", in *Radar Sensor Technology XXII*, International Society for Optics and Photonics, vol. 10633, 2018, p. 1 063 308.

[60] M. I. Skolnik, *Introduction to Radar Systems*. McGraw-Hill, 2001.

[61] Z. LI, "Applications of gaussian mixture model to weather observations", PhD thesis, The University of Oklahoma, Norman, OK, 2011.

[62] R. E. Kalman, "A new approach to linear filtering and prediction problems", *Journal of basic Engineering*, vol. 82, no. 1, pp. 35–45, 1960.

[63] T. Fortmann, Y. Bar-Shalom, and M. Scheffe, "Sonar tracking of multiple targets using joint probabilistic data association", *IEEE Journal of Oceanic Engineering*, vol. 8, no. 3, pp. 173–184, Jul. 1983, ISSN: 0364-9059. DOI: 10.1109/JOE.1983.1145560.

[64] Y. Bar-Shalom, T. E. Fortmann, and P. G. Cable, *Tracking and data association*, 1990.

[65] Y. Bar-Shalom, X Rong Li, and T. Kirubarajan, *Estimation with applications to tracking navigation*, 1st ed. 2001.

[66] H. W. Sorenson, *Kalman filtering: theory and application*. IEEE, 1985.

[67] P. Del Moral, "Nonlinear filtering using random particles", *Theory of Probability & Its Applications*, vol. 40, no. 4, pp. 690–701, 1996.

[68] J. Carpenter, P. Clifford, and P. Fearnhead, "Improved particle filter for nonlinear problems", *IEE Proceedings-Radar, Sonar and Navigation*, vol. 146, no. 1, pp. 2–7, 1999.

[69] S. S. Blackman, "Multiple-target tracking with radar applications", *Dedham, MA, Artech House, Inc., 1986, 463 p.*, 1986.

[70] S. Blackman and R. Popoli, "Design and analysis of modern tracking systems (artech house radar library)", *Artech house*, 1999.

[71] D. Reid, "An algorithm for tracking multiple targets", *IEEE Transactions on Automatic Control*, vol. 24, no. 6, pp. 843–854, Dec. 1979, ISSN: 0018-9286. DOI: 10.1109/TAC.1979.1102177.

[72] N. Wiener, "With engineering applications", p. 170,

[73] Y. Bar-Shalom and X.-R. Li, *Multitarget-multisensor tracking Principles and techniques*. 1995.

[74] P. S. Maybeck, *Stochastic models, estimation and control*, ser. Mathematics in science and engineering v. 141. New York: Academic Press, 1979, 3 pp., ISBN: 978-0-12-480701-3.

[75] L. Ljung, *System Identification Theory for the User*, 2nd ed. Upper Saddle River, N.J: Prentice Hall, 1999, ISBN: 0-13-656695-2.

[76] N. Levanon and E. Mozeson, *Radar Signals*. Hoboken, NJ, USA: John Wiley & Sons, Inc., 2004, 427 pp., ISBN: 0-471-47378-2.

[77] F. E. Nathanson, P. J. O'Reilly, and M. N. Cohen, *Radar design principles: signal processing and the environment*. Raleigh, NC: Scitech Publ., 1969, OCLC: 315625111, ISBN: 978-1-891121-09-8 978-1-891121-50-0.

[78] S. D. Blunt and K. Gerlach, "Adaptive pulse compression", in *Proceedings of the 2004 IEEE Radar Conference (IEEE Cat. No.04CH37509)*, Apr. 2004, pp. 271–276. DOI: `10.1109/NRC.2004.1316434`.

[79] B. Zrnic, A. Zejak, A. Petrovic, and I. Simic, "Range sidelobe suppression for pulse compression radars utilizing modified RLS algorithm", in *1988 IEEE 5th International Symposium on Spread Spectrum Techniques and Applications - Proceedings. Spread Technology to Africa (Cat. No.98TH8333)*, vol. 3, Sep. 1998, 1008–1011 vol.3. DOI: `10.1109/ISSSTA.1998.722532`.

[80] M. A. Richards, W. A. Holm, and J. A. Scheer, *Principles of Modern Radar: Basic Principles*. 2009, ISBN: 978-1-891121-52-4.

[81] T. Collins and P. Atkins, "Nonlinear frequency modulation chirps for active sonar", *Sonar and Navigation IEE Proceedings - Radar*, vol. 146, no. 6, pp. 312–316, Dec. 1999, ISSN: 1350-2395. DOI: `10.1049/ip-rsn:19990754`.

[82] J. A. Johnston and A. C. Fairhead, "Waveform design and doppler sensitivity analysis for nonlinear fm chirp pulses", *IEE Proceedings F - Communications, Radar and Signal Processing*, vol. 133, no. 2, pp. 163–175, 1986, ISSN: 0143-7070. DOI: `10.1049/ip-f-1.1986.0027`.

[83] P. Yichun, P. Shirui, Y. Kefeng, and D. Wenfeng, "Optimization design of NLFM signal and its pulse compression simulation", in *IEEE International Radar Conference, 2005.*, May 2005, pp. 383–386. DOI: `10.1109/RADAR.2005.1435855`.

[84]   R. McAulay and J. Johnson, "Optimal mismatched filter design for radar ranging, detection, and resolution", *IEEE Transactions on Information Theory*, vol. 17, no. 6, pp. 696–701, 1971, ISSN: 0018-9448. DOI: `10.1109/TIT.1971.1054722`.

[85]   N. Levanon, "Cross-correlation of long binary signals with longer mismatched filters", *Sonar and Navigation IEE Proceedings - Radar*, vol. 152, no. 6, pp. 377–382, Dec. 2005, ISSN: 1350-2395. DOI: `10.1049/ip-rsn:20050024`.

[86]   M. H. Ackroyd and F. Ghani, "Optimum mismatched filters for sidelobe suppression", *IEEE Transactions on Aerospace and Electronic Systems*, vol. AES-9, no. 2, pp. 214–218, Mar. 1973, ISSN: 0018-9251. DOI: `10.1109/TAES.1973.309769`.

[87]   S. D. Blunt, K. Gerlach, and T. Higgins, "Aspects of radar range super-resolution", in *2007 IEEE Radar Conference*, Apr. 2007, pp. 683–687. DOI: `10.1109/RADAR.2007.374301`.

[88]   S. Blunt and K. Gerlach, "Adaptive pulse compression via MMSE estimation", *IEEE Transactions on Aerospace and Electronic Systems*, vol. 42, no. 2, pp. 572–584, Apr. 2006, ISSN: 0018-9251. DOI: `10.1109/TAES.2006.1642573`.

[89]   Z. Li, Y. Zhang, S. Wang, L. Li, and M. Mclinden, "Fast adaptive pulse compression based on matched filter outputs", *IEEE Transactions on Aerospace and Electronic Systems*, vol. 51, no. 1, pp. 548–564, Jan. 2015, ISSN: 0018-9251. DOI: `10.1109/TAES.2014.130544`. [Online]. Available: `http://ieeexplore.ieee.org/document/7073512/` (visited on 06/17/2018).

[90]   Shang Wang, Zhengzheng Li, and Yan Zhang, "Application of optimized filters to two-dimensional sidelobe mitigation in meteorological radar sensing", *IEEE Geoscience and Remote Sensing Letters*, vol. 9, no. 4, pp. 778–782, Jul. 2012, ISSN: 1545-598X, 1558-0571. DOI: `10.1109/LGRS.2011.2181484`.

[91]   L. P. Goetz and J. D. Albright, "Airborne pulse-doppler radar", *IRE Transactions on Military Electronics*, vol. MIL-5, no. 2, pp. 116–126, Apr. 1961, ISSN: 0096-2511. DOI: `10.1109/IRET-MIL.1961.5008329`.

[92] D. P. Jorgensen, P. H. Hildebrand, and C. L. Frush, "Feasibility test of an airborne pulse-doppler meteorological radar", *Journal of Climate and Applied Meteorology*, vol. 22, no. 5, pp. 744–757, 1983. DOI: `10.1175/1520-0450(1983)022<0744:FTOAAP>2.0.CO;2`.

[93] R. M. Lhermitte, "Probing of atmospheric motion by airbrone pulse-doppler radar techniques", *Journal of Applied Meteorology*, vol. 10, no. 2, pp. 234–246, 1971. DOI: `10.1175/1520-0450(1971)010<0234:POAMBA>2.0.CO;2`.

[94] J. Testud, P. H. Hildebrand, and W.-C. Lee, "A procedure to correct airborne doppler radar data for navigation errors using the echo returned from the earth's surface", *Journal of Atmospheric and Oceanic Technology*, vol. 12, no. 4, pp. 800–820, 1995.

[95] W. D. Pan, P. R. Harasti, M. Frost, Q. Zhao, J. Cook, T. Maese, and L. J. Wagner, "Lossless differential compression of weather radar data in universal format using motion estimation and compensation", presented at the 26th Conference on Interactive Information and Processing Systems (IIPS) for Meteorology, Oceanography, and Hydrology, 2010, p. 6.

[96] Y. Zhang and S. Wang, "Remote relative wind velocity estimation using airborne doppler radar and spectrum analysis", *IEEE Transactions on Aerospace and Electronic Systems*, vol. 47, no. 3, pp. 1648–1667, ISSN: 0018-9251. DOI: `10.1109/TAES.2011.5937256`.

[97] G. V. Morris and L. Harkness, "Airborne pulsed doppler radar (artech house radar library)", *Artech House, November*, 1996.

[98] M SACHIDANANDA and D. S. ZRNIC, "An Improved Clutter Filtering and Spectral Moment Estimation Algorithm for Staggered PRT Sequences", en, *JOURNAL OF ATMOSPHERIC AND OCEANIC TECHNOLOGY*, vol. 19, p. 11, 2002.

[99] *Phased array system toolbox*. [Online]. Available: `https://www.mathworks.com/products/phased-array.html` (visited on 09/29/2018).

[100] Z. Li, Y. Zhang, S. Wang, and J. Cai, "Super-resolution processing for multi-functional lpi waveforms", in *Radar Sensor Technology XVIII*, International Society for Optics and Photonics, vol. 9077, 2014, p. 90770M.

[101] Xing Tan, W. Roberts, Jian Li, and P. Stoica, "Range-doppler imaging via a train of probing pulses", *IEEE Transactions on Signal Processing*, vol. 57, no. 3, pp. 1084–1097, Mar. 2009, ISSN: 1053-587X, 1941-0476. DOI: `10.1109/TSP.2008.2010010`.

[102] T. Yardibi, J. Li, P. Stoica, M. Xue, and A. B. Baggeroer, "Source localization and sensing: A nonparametric iterative adaptive approach based on weighted least squares", *IEEE Transactions on Aerospace and Electronic Systems*, vol. 46, no. 1, pp. 425–443, Jan. 2010, ISSN: 0018-9251. DOI: `10.1109/TAES.2010.5417172`.

[103] W. Roberts, P. Stoica, J. Li, T. Yardibi, and F. A. Sadjadi, "Iterative adaptive approaches to MIMO radar imaging", *IEEE Journal of Selected Topics in Signal Processing*, vol. 4, no. 1, pp. 5–20, Feb. 2010, ISSN: 1932-4553. DOI: `10.1109/JSTSP.2009.2038964`.

[104] S. Wang, Z. Li, Y. Zhang, B. Cheong, and L. Li, "Implementation of Adaptive Pulse Compression in Solid-State Radars: Practical Considerations", *IEEE Geoscience and Remote Sensing Letters*, vol. 12, no. 10, pp. 2170–2174, 2015, ISSN: 1545598X. DOI: `10.1109/LGRS.2015.2454481`.

[105] R. M. Haralick and L. G. Shapiro, *Computer and robot vision*. Addison-wesley, 1992.

[106] Shang Wang, Zhengzheng Li, Yan Zhang, Boonleng Cheong, and Lihua Li, "Implementation of adaptive pulse compression in solid-state radars: Practical considerations", *IEEE Geoscience and Remote Sensing Letters*, vol. 12, no. 10, pp. 2170–2174, Oct. 2015, ISSN: 1545-598X, 1558-0571. DOI: `10.1109/LGRS.2015.2454481`.

[107] B. L. Cheong, R. Kelley, R. D. Palmer, Y. Zhang, M. Yeary, and T. Yu, "Px-1000: A solid-state polarimetric x-band weather radar and time–frequency multiplexed waveform for blind range mitigation", *IEEE Transactions on Instrumentation and Measurement*, vol. 62, no. 11, pp. 3064–3072, 2013, ISSN: 0018-9456. DOI: `10.1109/TIM.2013.2270046`.

[108] *PX-1000, Advanced Radar Research Center*. [Online]. Available: `https://arrc.ou.edu/radar_px1000.html` (visited on 09/02/2018).

[109] J. Helmus and S. Collis, "The python ARM radar toolkit (py-ART), a library for working with weather radar data in the python programming

language", *Journal of Open Research Software*, vol. 4, no. 1, Jul. 18, 2016, ISSN: 2049-9647. DOI: `10.5334/jors.119`. [Online]. Available: `http://openresearchsoftware.metajnl.com/articles/10.5334/jors.119/` (visited on 09/02/2018).

[110] M. Fang, R. J. Doviak, and V. Melnikov, "Spectrum width measured by WSR-88d: Error sources and statistics of various weather phenomena", *Journal of Atmospheric and Oceanic Technology*, vol. 21, no. 6, pp. 888–904, Jun. 2004, ISSN: 0739-0572, 1520-0426. DOI: `10.1175/1520-0426(2004)021<0888:SWMBWE>2.0.CO;2`.

[111] L. B. Cornman, S. Gerding, G. Meymaris, and J. Williams, "Evaluation of an airborne radar turbulence detection algorithm", in *Proceedings of the 9th Conference on Aviation, Range, and Aerospace Meteorology*, 2000, p. 4.

[112] H. A. P. Blom and Y. Bar-Shalom, "The interacting multiple model algorithm for systems with markovian switching coefficients", *IEEE Transactions on Automatic Control*, vol. 33, no. 8, pp. 780–783, Aug. 1988, ISSN: 0018-9286. DOI: `10.1109/9.1299`.

[113] Y. Bar-Shalom, K. C. Chang, and H. A. P. Blom, "Tracking a maneuvering target using input estimation versus the interacting multiple model algorithm", *IEEE Transactions on Aerospace and Electronic Systems*, vol. 25, no. 2, pp. 296–300, Mar. 1989, ISSN: 0018-9251. DOI: `10.1109/7.18693`.

[114] D. Sengupta and R. A. Iltis, "Neural solution to the multitarget tracking data association problem", *IEEE Transactions on Aerospace and Electronic Systems*, vol. 25, no. 1, pp. 96–108, Jan. 1989, ISSN: 0018-9251. DOI: `10.1109/7.18666`.